Université de Lille

L2EP Laboratoire d'électrotechnique et d'électronique de puissance de Lille

Conception d'ondes mécaniques localisées contrôlées : application à l'haptique

Thèse de doctorat de l'Université de Lille
préparée à IRCICA

École doctorale n°632 Sciences de l'Ingénierie et des Systèmes (ENGSYS)
Spécialité de doctorat: Génie Electrique (GE)

Thèse présentée et soutenue à Villeneuve d'Ascq, le 13/10/2025, par

Mondher OUARI

Composition du Jury :

Dejan Vasic Professeur, CY Cergy Paris Université	Président
Valerie Budinger Professeure, ISAE-Supaero	Rapporteur
François Pigache Professeur, INPT-ENSEEIHT	Rapporteur
Charles Croënne Chargé de recherche, CRNS IEMN Lille	Examinateur
Frédéric Giraud Professeur, Université de Lille	Directeur de thèse
Christophe Giraud-Audine Professeur, Arts et Métiers Paritech	Co-directeur de thèse
Charles Hudin Ingénieur de recherche, CEA-LIST	Invité

Thèse de doctorat

Université de Lille

Laboratoire d'électrotechnique et d'électronique de puissance de Lille

Design of controlled localized mechanical waves: application to haptics

Doctoral Thesis of the University of Lille
prepared at IRCICA

Doctoral School No. 632 — Engineering and Systems Sciences (ENGSYS)
PhD Specialty: Electrical Engineering (EE)

Thesis presented and defended at Villeneuve d'Ascq on 13/10/2025 by

Mondher OUARI

Jury Members:

Dejan Vasic Professor, CY Cergy Paris UniversitY	President
Valerie Budinger Professor, ISAE-Supaero	Reviewer
François Pigache Professor, INPT-ENSEEIHT	Reviewer
Charles Croënne Researcher, CNRS IEMN Lille	Examiner
Frédéric Giraud Professor, University of Lille	Thesis Supervisor
Christophe Giraud-Audine Professor, Arts et Métiers ParisTech	Co-Supervisor
Charles Hudin Research Engineer, CEA-LIST	Guest

Doctoral Thesis

Acknowledgments

This dissertation is the outcome of sustained work carried out within L2EP and the HASAMé project—an experience that has been deeply enriching both professionally and personally. Its completion owes much to the support and contributions of many people, to whom I extend my sincere gratitude.

I am grateful to the jury members. I especially thank Prof. Dejan Vasic for agreeing to chair the jury. My thanks also go to Prof. Valeri Budinger and Prof. François Pigache for their meticulous reading and careful review of the manuscript. I am indebted to Dr. Charle Croënne for evaluating this work and for his insightful comments during the defense, which significantly strengthened the manuscript. I also thank Dr. Charles Hudin for attending the defense and for his constructive suggestions.

I am deeply thankful to my mentors for their guidance throughout these three years. To Anis Kaci: your steady encouragement and thoughtful discussions profoundly shaped my work and growth; your technical and personal support was a constant source of motivation. To Frederic Griaud and Christophe Giraud-Audine: thank you for your unwavering involvement and for the critical yet constructive feedback that consistently pushed me to refine my approach. I am also sincerely grateful to Prof. Betty Semail for her guidance and constructive criticism.

My thanks extend to my colleagues, Detjon and Angelica ,for their daily support, stimulating discussions, and generous sharing of ideas and time.

My deepest appreciation goes to my family. To my father, Ahmed, whose guidance and encouragement have shaped the person I am; . To my mother, Rabiaa, for her unconditional support. A special thanks to my aunt Dalila for her unfailing help. To my brothers, Kimou, Zinou, and Moatez, for always believing in me and standing by my side. I am also grateful to all family members and friends who supported me along this journey.

Finally, my profound thanks go to my wife, Rayenne. Your patience and quiet strength carried me through countless drafts and deadlines. Thank you for accepting the long hours, celebrating the small wins, and reminding me of what truly matters. This achievement is as much yours as it is mine.

Abstract

Conducted within the framework of the multidisciplinary HASAMé project, the work aims to overcome the limitations of current surface haptic technologies, particularly regarding scalability, energy efficiency, and the spatial precision of tactile effects. The central objective is to generate localized ultrasonic friction, allowing users to perceive tactile feedback such as textures, buttons, or directional cues directly on touch interfaces. To achieve this, both passive and active confinement approaches are investigated. Passive confinement leverages the geometric and material properties of periodic structures—such as mechanical pillars—to create localized vibrational zones through wave attenuation and mode conversion. These structures are designed and analyzed using analytical modeling based on beam and plate theories, as well as finite element simulations, with experimental prototypes validating their effectiveness. On the other hand, active confinement is realized through networks of piezoelectric actuators and sensors integrated into the surface. Control strategies are developed using modal superposition and implemented in a rotating reference frame, enabling real-time shaping of the vibration field. This approach allows not only confinement but also the generation of traveling waves, which are crucial for inducing directional shear forces perceived by the user's fingertip. A significant contribution of this thesis is the introduction of an electrical-analogy-based modeling framework using Mason's equivalent circuit, which treats each section of the vibrating surface as a three-port electrical cell. The methodology provides a flexible tool for analyzing and designing complex haptic systems with distributed control. Experimental results obtained with custom-designed electronic boards and laser vibrometry confirm the theoretical predictions, showing precise confinement of vibration and efficient control of tactile responses. Overall, this work provides a comprehensive framework—spanning modeling, control, experimental implementation, and human-centered evaluation—for the development of next-generation haptic interfaces. It opens the

way for intelligent, responsive surfaces applicable to automotive controls, medical devices, and interactive consumer electronics.

Contents

List of Figures

List of Abbreviations and Symbols

Abbreviations

HCI	Human-Computer Interaction
HASAMé	Haptic SurfAces enhanced by Métamaterials
USF	Ultrasonic Shear Forces
FEM	Finite Element Method
ABH	Acoustic Black Hole
PI	Proportional-Integral (controller)
VR	Virtual Reality
OLED	Organic Light Emitting Diode
DSP	Digital Signal Processor
L2EP	Laboratoire d'Électrotechnique et d'Électronique de Puissance
IEMN	Institut d'Électronique, de Microélectronique et de Nanotechnologie
LGF	Laboratoire Georges Friedel
LAMIH	Laboratoire d'Automatique, de Mécanique et d'Informatique Industrielles et Humaines
Hap2U	Industrial partner specializing in ultrasonic haptics
ADC	Analog to Digital Converter
PWM	Pulse Width Modulation
DC	Direct Current
AC	Alternative Current
CAD	Computer-Aided Design

List of Symbols

$u(x,t)$	Displacement field at position x and time t
$\phi_n(x)$	Mode shape function for the n-th vibration mode
$\eta_n(t)$	Modal coordinate (amplitude) of the n-th mode
ω	Angular frequency (rad/s)
ω_0	Resonance (natural) frequency
$\delta\omega$	Frequency detuning between excitation and resonance
f	Frequency (Hz)
k	Wave number (rad/m)
λ	Wavelength of the traveling wave
T	Transformation matrix in Mason's model
A	Cross-sectional area or amplitude
ρ	Density of the material
C_{31}	Elastic stiffness or dynamic modulus
Γ	Propagation constant
Z_0	Characteristic mechanical impedance
Z_t	Transfer impedance (Mason model)
Z_s	Series impedance (Mason model)
V_1, V_2	Equivalent electrical voltages at the cell boundaries
I_1, I_2	Equivalent electrical currents at the cell boundaries
V_s	Intermediate voltage in the circuit
I_a, I_b	Intermediate current variables
E_0	Source term representing piezoelectric force
M	Mass
K	stiffness
D	Damping coefficient
F_a	Actuator force
x_a	Position of actuator a
x_c	Position of sensor c
n_a	Number of actuators
n_c	Number of sensors
U_d, U_q	Control voltages in rotating frame (direct/quadrature)
SWR	Standing Wave Ratio
TWR	Traveling Wave Ratio
K_p	Proportional gain of PI controller
K_i	Integral gain of PI controller
s	Laplace variable
$H(s)$	Transfer function
ξ	Spatial coordinate

General Introduction

Haptics, derived from the Greek word haptikos, refers to the science of touch and tactile feedback, where users can physically interact with virtual or real environments through the sensation of touch. It plays a critical role in human-computer interaction (HCI) by simulating different touch-based experiences, allowing users to feel textures, resistance, pressure, and sometimes even motion. This field has evolved significantly, with modern haptic technologies integrated into various devices such as smartphones, virtual reality (VR) systems, robotics, medical devices, gaming consoles, and the automotive industry. The goal of haptics is to create more immersive, intuitive, and effective ways for users to interact with digital systems.

In virtual reality, for instance, haptic devices such as gloves, suits, or controllers enable users to experience the sensation of touching or manipulating virtual objects, enhancing the experience's realism. This touch feedback can be in the form of vibrations, forces, or even temperature changes. Such integration is especially critical in applications like training simulations for pilots [1], surgeons [2], or military personnel [3] where haptic feedback adds a layer of realism that helps improve training outcomes.

In the medical field, haptics are revolutionizing surgical training and medicine. Surgeons can use haptic-enabled robotic systems to perform complex surgeries remotely with precision and feedback as if they were physically present [4]. Medical students can practice procedures using haptic simulators that allow them to feel the resistance and texture of tissues or organs, improving their learning experience [5].

Advances in haptics are also benefiting gaming and entertainment. Haptic vests or controllers allow players to feel impacts, vibrations, and even environmental effects like wind or rain, deepening their immersion in virtual worlds [6, 7]. Meanwhile, haptic feedback is used in robotics to enable more precise control over robotic arms, allowing operators to perform delicate tasks such as assembling fine components or handling fragile objects . [8, 9]

Beyond these applications, haptics is increasingly used in social interactions, especially remote ones. Haptic technology is adding a new dimension to remote interactions [10]. Devices like haptic gloves or bracelets allow users to simulate physical touch, such as a handshake, hug, or pat on the back, enhancing emotional connection even when participants are kilometers apart. This technology is gaining attention in virtual meetings [11], and long-distance relationships[12], offering a more tangible way to express affection, empathy, or support.

In the automotive industry [13] , haptic technology is becoming a key innovation for enhancing driver experience, safety, and control. Modern vehicles now incorporate haptic feedback into steering wheels, pedals, and touchscreens to provide real-time information to the driver. For example, steering wheels equipped with haptics can vibrate to alert drivers when they drift out of a lane, helping to prevent accidents. Similarly, haptic feedback in pedals can signal hazardous road conditions, like ice or sudden stops ahead. Touchscreen interfaces in cars also integrate haptic feedback, allowing drivers to feel subtle vibrations when interacting with navigation systems, media controls, or climate settings. This reduces the need to avoid the road and enhances overall user safety [14].

While haptic technology offers immense potential across various industries, its integration presents several challenges that limit its widespread adoption. One of the primary issues is the complexity and cost of designing precise, responsive haptic systems that can accurately simulate real-world sensations. Creating realistic tactile feedback requires advanced hardware, such as actuators and sensors, which can be expensive to develop, manufacture, and maintain. Additionally, haptic systems often require significant computational power to process and deliver real-time feedback, which can be difficult to achieve without introducing delays or inaccuracies, particularly in high-demand applications like virtual reality or medical simulations. Another significant challenge is ensuring the consistency and reliability of haptic feedback across different devices and environments. Factors such as variations in user sensitivity, device limitations, or environmental conditions can affect the perception of touch, making it difficult to standardize experiences across platforms. For example, the same haptic feedback that feels natural in a gaming controller may not be effective or comfortable in a steering wheel or medical instrument. Moreover, designing haptics for automotive interfaces or virtual environments often requires complex calibration to ensure that the feedback is intuitive, safe, and doesn't cause distraction or discomfort. The lack of industry-wide standards for haptic technology also creates difficulties in seamless integration, as developers face challenges when trying to ensure compatibility across different hardware and software ecosystems. This fragmentation can slow the development of haptic applications and limit interoperability between devices. Addressing these integration problems will require advancements in haptic technology, standardization efforts, and more cost-effective production methods to fully unlock its potential across industries.

In summary, haptic technology holds immense promise across diverse sectors, offering the potential to revolutionize how humans interact with machines and digital environments. However, realizing this promise requires overcoming significant engineering, perceptual, and integration challenges. The research presented in this thesis aims to contribute to this goal by exploring novel strategies for vibration control and confinement as a foundational step toward achieving robust, scalable, and versatile haptic systems.

Hasamé Project

This Work is situated within the framework of the HAsame project, a multidisplicary project funded by The ANR french agency under agreement ANR-21-CE33-0020.

The HASAMé project (Haptic SurfAces enhanced by Métamaterials) is an ambitious multidisciplinary initiative focused on transforming human-computer interaction through advanced haptic technologies. At its core, the project develops smart surfaces capable of delivering realistic and programmable tactile sensations—such as button clicks and texture feedback—via a novel stimulation technique called Ultrasonic Shear Forces (USF). These surfaces are designed to address critical limitations of current touchscreen technology, particularly the over reliance on visual input, which affects accessibility and safety, notably in automotive settings. By embedding display, touch sensing, and haptic feedback into a unified surface, HASAMé envisions more inclusive, intuitive, and safer user interfaces.

A key innovation in HASAMé is the use of engineered metamaterials placed beneath the interactive surface. These metamaterials are designed to manipulate vibration propagation and confinement, enabling precise control over where and how tactile feedback is felt. Both passive and active variants are explored: passive structures confine vibration through geometry and material design, while active ones use embedded piezoelectric components for tunable and programmable feedback. Combined with distributed actuation and sensing capabilities, these layers transform static surfaces into responsive, interactive mediums suited for complex geometries like OLED displays or 3D automotive dashboards.

Crucially, the project integrates psychophysical testing to validate and optimize the haptic sensations from the user's perspective. Through rigorous sensory evaluation protocols, human participants assess the realism, clarity, and usability of the simulated tactile feedback. These tests help define perceptual thresholds and establish a "tactile language"—a set of standardized descriptors and parameters—that guide the development of haptic effects. Additionally, multimodal evaluations involving visual and auditory cues are conducted to understand the broader user experience and ensure that the HASAMé devices meet real-world demands in terms of comfort, effectiveness, and satisfaction. This human-centered approach ensures that technological advancements translate into genuinely useful and perceptually convincing user experiences.

Thuis project is composed of 3 Major work projects :

WP1 – Human-Computer Interaction (HCI)

Composed of : LGF laboratory and LAMIH, this work package focuses on evaluating how users perceive and interact with the tactile surfaces developed in the project. It involves conducting psychophysical studies to determine stimulation thresholds and user preferences for various haptic effects such as button clicks and textures. WP1 also defines a consistent tactile language and tests the user experience across different scenarios (e.g., transportation, healthcare, public interfaces), ensuring that HASAMé devices are intuitive, effective, and enjoyable to use.

WP2 – Structures (Metamaterials Design)

Composed of : Hap2u , IEMN , and L2EP, WP2 is dedicated to designing the physical metamaterial layers that enable controlled haptic feedback. It begins with passive configurations that localize vibrations, then progresses to tunable, active metamaterials incorporating piezoelectric components. These structures allow precise modulation and superimposition of vibration modes necessary for Ultrasonic Shear Forces (USF)-based stimulation. WP2 also demonstrates the adaptability of these back layers by applying them to OLED displays and complex 3D smart surfaces.

WP3 – Control (Mechatronic Integration)

Composed of L2EP, this work package develops the electronics and software systems required to drive the tactile feedback mechanisms. It ensures stable and precise stimulation through closed-loop control, supports distributed actuation to manage multiple actuators simultaneously, and introduces self-sensing capabilities to detect user interactions without the need for additional sensors. WP3 provides the technical foundation for real-time, programmable, and robust haptic responses, fully integrated with the structures from WP2 and validated through user studies in WP1.

The primary objective of this PhD thesis is to contribute to the advancement of haptic interfaces through the integration and control of ultrasonic stimulation within smart surfaces, with a particular emphasis on the development of localized ultrasonic friction (USF). Achieving this goal requires both theoretical and experimental progress to address the specific challenges associated with localized haptic rendering.

To this end, the work presented in this thesis builds upon the outcomes of experimental investigations and system developments carried out throughout the project. These results have played a critical role in identifying and refining the specifications necessary for the design of next-generation haptic interfaces. As a result, new prototypes have been conceived and developed to meet these revised requirements, enabling more effective and precise control of ultrasonic vibration patterns for enhanced haptic perception

Thesis structure

This manuscript is organized as follows :

Chapter 1 introduces the field of haptic technologies, with a focus on surface haptics and ultrasonic-based tactile feedback. It presents the motivations for developing localized haptic effects and highlights the current challenges in scalability, energy efficiency, and vibration control. A detailed review of existing methods is provided, including both passive and active techniques for vibration control, as well as their limitations in real-world applications. Moreover, a vibration confinement methodology based on mechanical-electrical analogy is presented.

Chapter2 presents a method for passively confining vibrations by using periodic structures composed of resonant mechanical elements (pillars) integrated into the haptic surface. It introduces the theoretical foundation based on mode conversion and wave attenuation and outlines the design and simulation of a prototype using finite element methods (FEM). The influence of key parameters—such as pillar geometry, placement, and periodicity—on the confinement performance is studied. Experimental validation confirms the effectiveness of this method in isolating vibration to localized regions on the surface.

Chapter 3 explores an active approach to vibration confinement by leveraging actuator/sensor networks to dynamically shape vibrational patterns. It begins with a simulation framework based on modal superposition and beam theory to demonstrate the concept of active confinement. Different control strategies are tested to localize energy around actuators. An experimental setup with piezoelectric actuators and laser vibrometry is used to validate the simulation. Results demonstrate successful confinement and the system's capacity to shape vibration fields, including generating traveling waves.

General Conclusion provides conclusion and prospective of this work

1 Introduction

1.1 Haptic and Haptics

1.1.1 Definition of haptic and haptic technology

In scientific discussions surrounding haptic technologies, the terms "haptics" and "haptic" are often used interchangeably, yet they hold distinct meanings and applications, both tied to the sense of touch.

The term "haptic" as a noun pertains to the human perceptual system, encompassing both tactile (cutaneous) responses and kinesthetic perceptions (sensations from muscles and joints). As an adjective, "haptic" describes anything related to or involving the sense of touch. In technological contexts, it refers to devices or features that provide tactile feedback, enabling users to interact with virtual objects as if they were physically present.

Conversely, "haptics" refers to the broader field of study and application of touch-based technology. This multidisciplinary domain integrates knowledge from psychology, neuroscience, robotics, and computer science to design systems that simulate tactile experiences. Haptics aims to replicate the sense of touch within digital interfaces, facilitating new forms of human-computer interaction. The scope of haptics extends across various industries, from virtual reality and medical simulation to remote collaboration, where it plays a pivotal role in enhancing user engagement and realism in digital environments.

A clear distinction between "haptic" and "haptics" is essential for understanding the full potential of touch technology. While "haptic" emphasizes the sensory aspects of touch in devices, "haptics" encompasses the scientific and technological advancements necessary to reproduce these sensations. Together, they represent a critical frontier in technological development, fostering more immersive, interactive, and human-centered digital experiences.

The incorporation of haptic feedback into devices significantly enriches user

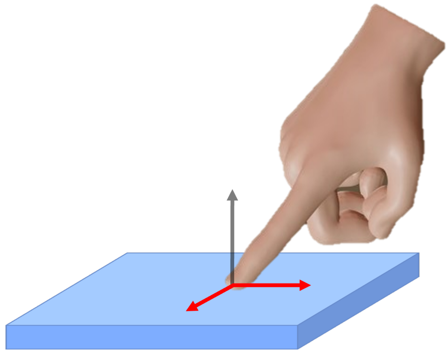

Figure 1.1: Schematic of the direction of force: normal (in black) and tangential (in red).

interactions by creating a more immersive and tangible experience. Simultaneously, ongoing advancements in the field of haptics continue to expand the possibilities for integrating digital and physical realities, enabling more sophisticated and engaging virtual environments.

In recent years, haptics has witnessed significant advancements aimed at developing innovative feedback mechanisms for devices or introducing haptic feedback in devices that currently lack it. Haptic feedback devices engage both human perceptual systems: the touch system (tactile feedback) and the kinesthetic system (feedback related to movement and force). This thesis falls within the domain of tactile haptic devices, focusing specifically on surface haptics. Surface haptics is a rapidly growing field of research that aims to create tactile sensations on physical interfaces, such as the touchscreens commonly found in mobile phones, tablets, and other interactive devices.

1.2 Surface Haptics Technologies

Surface haptics encompasses a wide array of devices and technologies, with numerous efforts made to classify these systems. For instance, [15] proposed a classification scheme for haptic devices in virtual reality based on interaction methods or paradigms. According to this classification, haptic devices are divided into three main categories: 'desktop haptics' (force feedback for virtual tools), 'surface haptics' (direct interaction with touchscreens), and 'wearable haptics' (force feedback through wearable devices like gloves, helmets, and shoes).

To enhance the taxonomy of surface haptics, [16] conducted a comprehensive review of haptic surfaces that generate tactile effects on touch interfaces. In their study, the authors categorized devices based on the direction of the

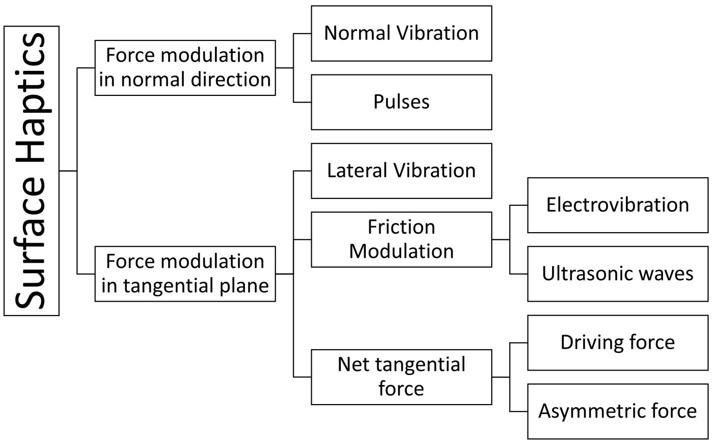

Figure 1.2: Classification of the current technologies for surface haptics displays based on the stimulation direction and method.

force they provide—either normal (perpendicular) or tangential (parallel) to the surface (see Figure 1.1). Their analysis resulted in the classification illustrated in Figure 1.2, which serves as a foundation for the discussion and further development presented in the following section of this thesis.

1.2.1 Haptic surfaces modulating a force in normal direction

Some devices are capable of directly indenting the fingertip by generating forces in the normal direction. These forces can be produced by leveraging two main principles: vibrations or pulses.

1.2.1.1 Normal Vibration

When a surface is actuated by a basic vibration motor, such as those commonly integrated into mobile devices, a vibration wave propagates through the entire structure. This wave reaches the user's finger or hand in contact with the device. Such an approach is often sufficient for delivering simple vibrotactile feedback, like confirming a button press or signaling an incoming call. However, these vibrations typically spread uniformly across the entire surface, limiting spatial precision and the ability to create localized tactile effects.

To produce more complex and discernible sensations, variations in vibration transients, frequencies, and intensities can be employed [17]. These tactile signals can be generated by various types of actuators, including electromagnetic devices such as linear resonant actuators (LRA), voice coil motors, and eccentric rotating mass (ERM) motors, as well as piezoelectric actuators [18].

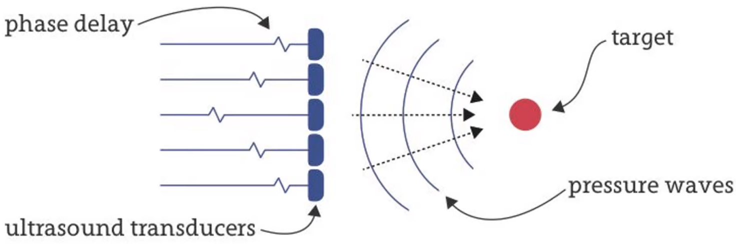

Figure 1.3: Phased array principle [23]

Each actuator type offers distinct characteristics in terms of frequency range, amplitude, response time, and energy efficiency, enabling a broad spectrum of tactile feedback applications.

1.2.1.2 pulses

In the context of this thesis, pulses refer to short, transient deformations that occur on the finger pulp. Various methods can be employed to generate these pulses on a rigid plate. In this section, we present three such methods.

Phase array acoustic pulses Acoustic waves can propagate through various media, including solids, liquids, and gases. In the context of haptic feedback devices, acoustic wave focalization has been explored in air for virtual reality applications and on solid surfaces for touchscreen devices.

In 1995, [19] demonstrated that a nonlinear ultrasonic wave phenomenon known as "radiation pressure" could generate enough force to create a tactile sensation. Later, in 2006, [20] successfully focused acoustic waves on a water surface using an array of piezoelectric transducers. By precisely calculating the actuation delay for each transducer, the waves were made to converge at a single focal point simultaneously, as illustrated in Figure 1.3. However, the ultrasonic waves produced by this method can pose risks to the auditory system due to sound pressure levels that exceed recommended safety limits [21].

In 2015, [22] extended this principle to a solid, transparent surface actuated by electromagnetic actuators positioned along its edges. By employing wave propagation theory and considering the structure's eigenmodes, the authors calculated the precise contribution of each actuator required to generate localized vibrations at one of the plate's four corners. This approach showed promising results in accurately reproducing reference tactile fields, offering a new avenue for creating localized haptic feedback.

In elastic media, like glass plates , waves produced by phased array will

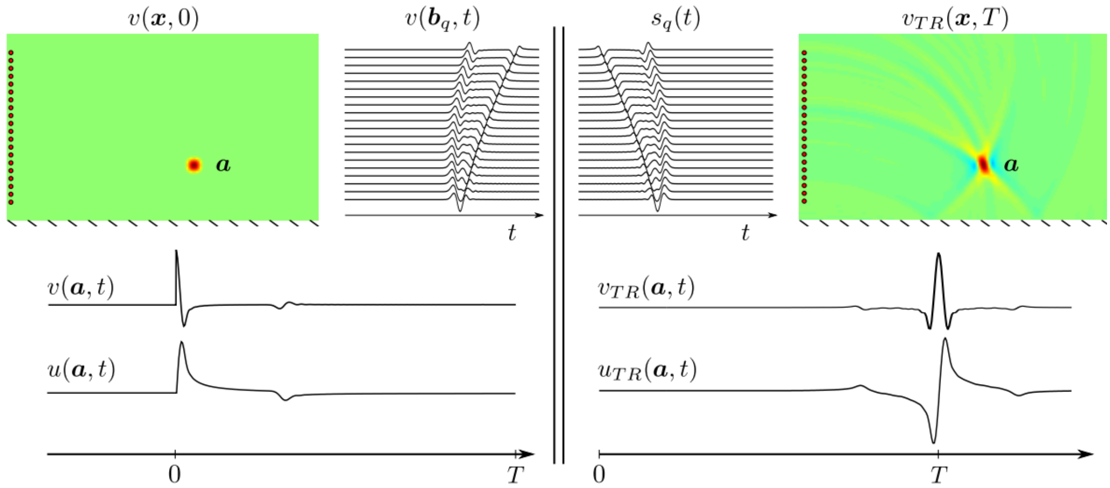

Figure 1.4: The learning phases of the time-reversal method for an initial deformation at point [26], with $u(a, t)$ representing the displacement field at point a, $v(a, t)$ as its derivative, and $s_q(t)$ as the signal emitted by transducer q during the time-reversal phase. The initial velocity field $v(x, 0)$ is reproduced via time-reversal as $v_{TR}(x, t)$.

be reflected at the plate's edges, hence creating unwanted reflection which can interfere with the desired outcome.

time reversal In order to improve wave focusing on a plate, time reversal methods [24, 25] can be used in order to improve the resolution compared to phased array.

With this method , each actuator have a different contribution to generate wave focalization. To determine the contribution of each actuator, the authors employ a learning phase, during which initial deformations are induced at various locations on the surface via external excitation. The acoustic wave propagates and is reflected by the boundaries. By taking advantage of piezoelectric transducer [24] or magnetic coils [25], which can work as actuators or sensors ,the propagating signature on each actuator is measured as an electrical signal . By time-reversing these electrical signals, the initial deformation can be reproduced at the respective locations. The stages of the learning process are shown in Figure 1.4.

Multimodal superimposition In his thesis, [27] proposed an analytical approach to achieve reference deformation in structures. Their approach is based on multimodal decomposition theory, enabling the desired structural deformation to be reconstructed through the superposition of the structure's eigenmodes. Analogous to a Fourier series decomposition, they project the desired

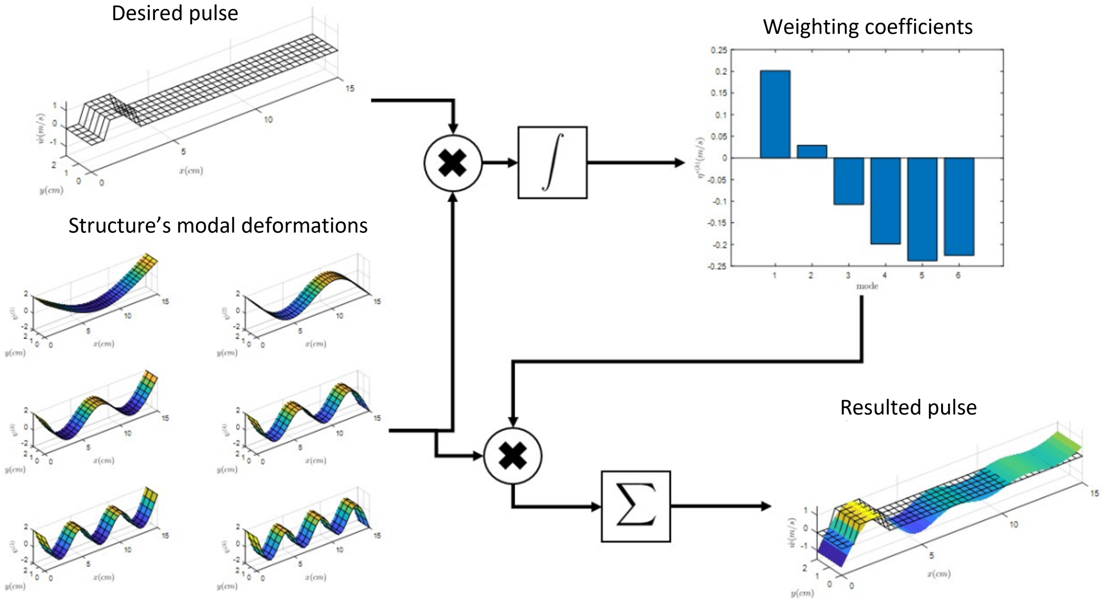

Figure 1.5: Multimodal superposition principle [29].

deformation velocity onto the structure's orthogonal basis to derive the mode's weighting coefficients needed to approximate the initial shape through recomposition. Control voltages are precomputed offline, and the structure is managed in an open-loop system. The authors selected a transient regime to maximize kinetic energy precisely at the focalization point in time and space, as illustrated in Figure 1.5. [28] improved the performance and robustness of this method by employing spatio-frequency filters, enabling independent control of each vibration mode within a control loop.

1.2.2 Force modulation in tangential plane

1.2.2.1 lateral vibration

Similar to force modulation in the normal direction, lateral vibrations of a surface can also create tactile stimulation on the fingertip. For instance, [30] demonstrated that the skin displacement caused by lateral vibrations can simulate tangential force modulation when interacting with rough surfaces, even when the surface itself remains flat and smooth. This lateral force can be used to create the sensation of roughness on a virtual surface.

One significant advantage of lateral vibrations is that the actuators can be placed at the edges of the touch surface, facilitating better integration of haptics into consumer products. Additionally, lateral forces allow direct interaction with the finger, enhancing tactile feedback. Some devices, based on friction modulation, utilize the user's finger movements to generate force, further improving technological integration. These devices will be discussed in the following section.

1.2.2.2 Friction modulation

An alternative approach to generating lateral force modulation—without relying on direct mechanical actuators—involves the technique known as friction modulation. This method modulates the friction between a moving fingertip and a touch surface to create tactile sensations, enabling the perception of various textures and interactive effects. Unlike conventional mechanical actuation, friction modulation produces lateral forces indirectly, through controlled variations in surface friction.

The resulting frictional force experienced by the user depends on several factors, including the fingertip's position on the surface, the normal force applied by the user, and the finger's exploration speed. By manipulating these interactions, it becomes possible to simulate a wide range of tactile experiences.

Two primary techniques are commonly employed to achieve this friction modulation: electrostatic actuation, also known as electro-vibration, and ultrasonic vibration.

Electrovibration The authors in [31] discovered that dragging a dry finger over a conductive surface, powered by alternating current and covered with a thin insulating layer, as shown in figure 1.6, produced a distinct sensation compared to when the surface was not powered. This phenomenon is explained by the formation of a capacitive effect between the finger and the powered surface,generating an attractive force, increasing the friction.

Exploiting this results, [33] developed an electrotactile display composed of an array of electrodes insulated with a thin dielectric layer. By utilizing friction induced by electrostatic attraction forces, they were able to generate texture sensations on the touch surface. The phenomenon was named as *"electrovibration"* i.e electrically induced vibration. Moreover, [34] showed that electrovibration can be delivered through a commercial capacitive touch screen, which demonstrates the viability of this technology on large surfaces. They also showed that varying the frequency and amplitude of an electrovibrating signal can evoke different sensations properties such as stickiness, smoothness or pleasantness

The electrification principle has result in various commercial such , Tanvas^{TM} [35] and a 3D texture rendering device developed by Disney [36]. . However

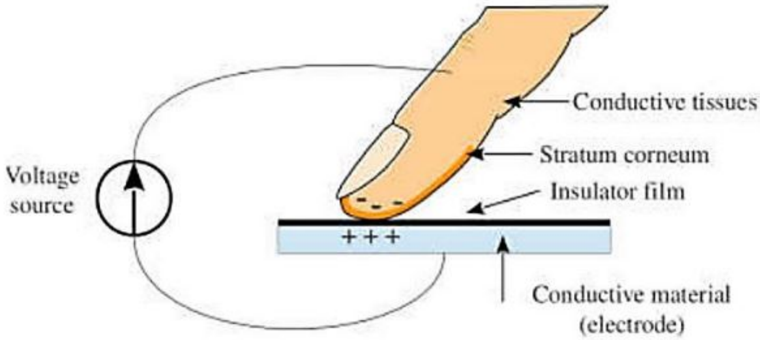

Figure 1.6: Working principle of Electro-adhesion [32]

[37] reported that the surface roughness and the finger's skin humidity affected the perception of the haptic effect

Ultrasonic Vibration Another way to achieve friction modulation is to use ultrasonic vibration. Ultrasonic vibrations are mechanical waves that have a frequency surpassing the human perception threshold (superior to 20 kHz). These waves have the capacity to propagate across diverse solid materials , such as aluminum and glass. When a finger slides on a rigid surface that is vibrating at ultrasonic frequency, a reduction of the friction occurs.

Achieving ultrasonic vibration on a touch surface typically requires attaching piezoelectric actuators to the surface and driving them with sinusoidal voltage. To efficiently produce these vibrations, a stationary bending mode is energized, where the system resonates at its natural frequency to optimize the power use. A specific design process is then required to optimize material selection, geometry, and excitation frequency.

The first use of this phenomena in haptic application was by [38]. The Authors obtained a vibration amplitude of up 2 µm, and they reported that friction reduction increased with the vibration amplitude. This effect was referred to as *active lubrication* or *ultrasonic lubrication* to illustrate its ability to reduce friction through ultrasonic vibrations.

Since then, significant research on ultrasonic surface haptic stimulators has been conducted at the L2EP laboratory. This work began with [39], where the first ultrasonic vibration-based device was developed. Building on this foundation, a tactile stimulator called Stimtac was created. Stimtac consisted of a copper surface equipped with multiple piezoelectric actuators and force sensors. the force sensors are used to measure the finger position on the device [40]. Over the years, the Stimtac prototype was refined with more sensi-

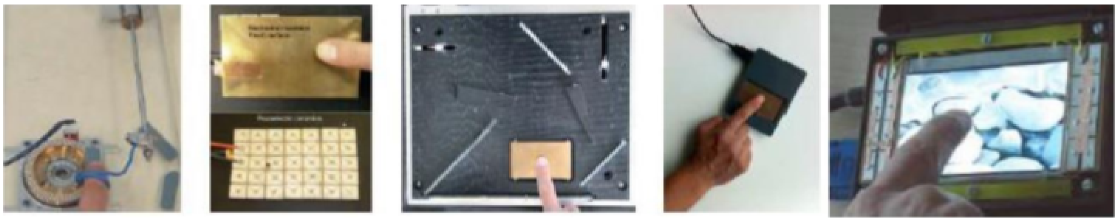

Figure 1.7: Evolution of the StimTac prototype: 1D configuration, 2D feedback, 2D input and feedback (2008), compact US prototype (2010) and transparent prototype (2012)

tive sensors, improved hardware robustness, and more energy-efficient control mechanisms.

In 2012, a transparent tactile stimulator was developed [41], leading to the creation of E-Vita, a tactile feedback tablet that incorporated both haptic and visual feedback [42]. The combination of a transparent surface with visual-tactile stimulation eventually resulted in the commercial product XploreTouch, developed by Hap2U. The progression of ultrasonic lubrication devices is illustrated in Figure 1.7.

The complex mechanisms behind ultrasonic lubrication are not yet fully understood. However, two prominent theories have been proposed in the literature to explain these phenomena: the intermittent contact theory and the squeeze-film effect.

The squeeze-film effect is based on the formation of a thin air layer that undergoes cyclic compression and decompression between the fingertip and the oscillating surface at high speeds. This theory suggests that the air film created by ultrasonic vibrations reduces the contact area between the fingertip and the surface, leading to a decrease in frictional forces during sliding. [43, 44] investigated this phenomenon and observed distinct frictional behaviors between vibrating and non-vibrating surfaces. However, a more detailed study by [45] indicates that the observed friction reduction cannot be fully explained by the squeeze-film effect alone, as it does not completely predict friction behavior.

To address this, [45] proposed the intermittent contact theory, which suggests that the interaction between the finger and the vibrating surface is not continuous. According to this theory, at certain vibration amplitudes, the finger periodically loses contact with the oscillating surface, reducing the lateral forces exerted during sliding. This intermittent contact leads to the observed friction reduction between the fingertip and the surface.

Although the intermittent contact theory has gained partial support within the scientific community, recent studies have revealed a more complex interaction between both the squeeze-film effect and intermittent contact, suggesting that they jointly contribute to active lubrication [46]. [47] proposed that partial squeeze-film levitation modulates the perceived friction on the fingertip. However, the exact role each mechanism plays in active lubrication remains unknown, awaiting further exploration and deeper clarification.

The aforementioned devices and technologies all explored transversal ultrasonic vibrations i.e out-of-plane vibrations. [48] developed an in-plane vibration based ultrasonic haptic device. It showed better energetic performance specially at high ultrasonic frequencies for similar perceptions and better robustness to finger interactions.

1.2.2.3 Net tangential force

The previously discussed prototypes based on friction reduction require a moving finger (active finger) to induce haptic feedback. Net tangential force is a solution to generate haptic feedback on a passive finger, because they are shear forces created on the finger independently of its moving speed or direction. According to [16] two methods or type of shear forces exists : asymmetric friction force and a driving force.

Asymmetric friction force In [49], the authors used electromagnetic actuators to generate a sawtooth displacement at 5 Hz on a plate. Since friction depends on the relative velocity between the finger and the plate, the sawtooth motion creates a strong asymmetry in friction: the relative speed is higher when the plate's velocity is high. As a result, a net lateral force is produced. However, this method requires large-amplitude, low-frequency movements, which limits its practicality for certain applications.

To overcome this limitation, [50] developed a device composed of two actuators. The first is a piezoelectric actuator responsible for producing active lubrication through ultrasonic actuation. The second is an electromagnetic actuator that generates 100 Hz oscillations in the tangential direction. By synchronizing the friction reduction with the oscillations, a shear force is applied to the user's finger, producing a tactile sensation. Using a similar method, [51] replaced ultrasonic lubrication with electrovibration to increase friction during a specific phase of the oscillation.

For actively generating lateral forces, [52] developed a device that simultaneously modulates friction using electrostatic actuation and generates in-plane ultrasonic oscillations at 30 kHz. The direction and magnitude of the active lateral forces depend on the phase relationship between the in-plane oscillation and electrovibration.

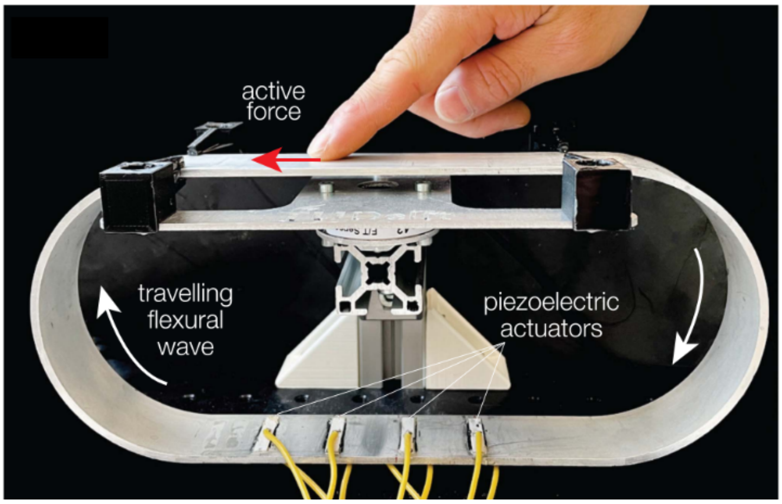

Figure 1.8: ring-type structure to generate travelling wave [54]

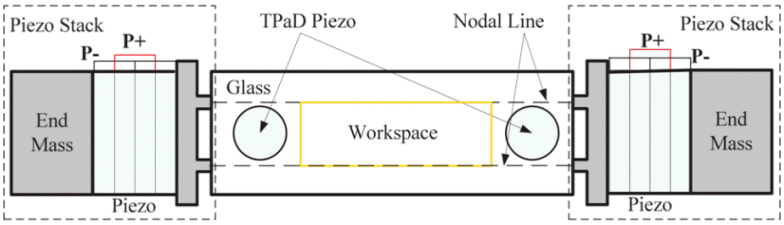

Figure 1.9: Top view of the LateralpaD structure [55]

driving force It is possible to generate shear forces by using two different vibration modes on the touch surface. These two modes must be excited simultaneously at an intermediate frequency between their respective resonance frequencies. This excitation allows for the creation of elliptical particle motion, which produces a driving force. For this purpose, [53] excites two out-of-plane vibration modes in a finite beam, at an intermediate frequency and with a phase shift. This results in a traveling wave that generates elliptical motion. To achieve a better traveling wave ratio, [54] excites two traveling modes on a ring-type structure as depicted in figure 1.8, which provides an infinite vibration surface, leading to an improved traveling wave ratio. .

Rather than using two identical vibration modes, [55] employs an out-of-plane mode, generated by piezoelectric actuators placed on the surface, and an in-plane vibration mode, created using two stacks of piezoelectric actuators on each side of the surface, as shown in Figure 1.9 .

To improve the integrability of this technique, which is based on modal superimposition, the L2EP laboratory developed a device in which the actuators are positioned exclusively on the surface [56], as illustrated in Figure 1.10. The

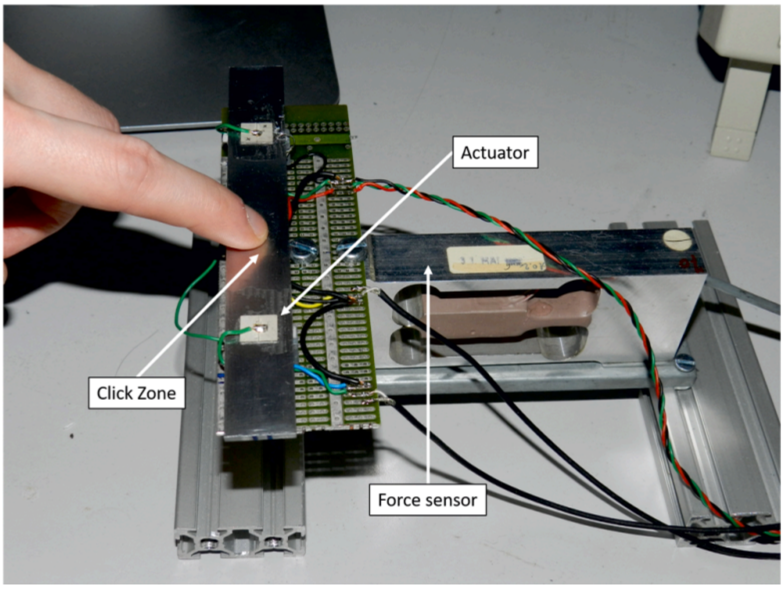

Figure 1.10: The device used to generate two different vibration modes simultaneously [56]

prototype was designed to support the coexistence of two ultrasonic vibration modes at the same frequency: the first mode corresponds to an out-of-plane vibration, while the second mode induces an in-plane vibration.

By simultaneously actuating both vibration modes with a controlled phase shift of $\pi/2$, an elliptical motion is generated at the surface. This elliptical movement enables the modulation of lateral forces, which can be perceived by the user's fingertip as tactile feedback.

Since the device is intended for direct interaction with the user's fingers, a closed-loop control system was implemented to ensure the maintenance of the desired phase shift between the two vibration modes. This feedback loop guarantees the stability and effectiveness of the generated tactile sensations, regardless of external disturbances or variations in operational conditions.

1.2.3 Surface haptic challenges

Despite the advancement in different haptic technologies, at the except of the basic normal vibration, none of the methods have made it past the prototype stage due to several problems.

Although the classic normal vibrations methods is enough for the confirmation of control actions, many applications require more than haptics for the confirmation of actions such as searching and finding the control elements. The

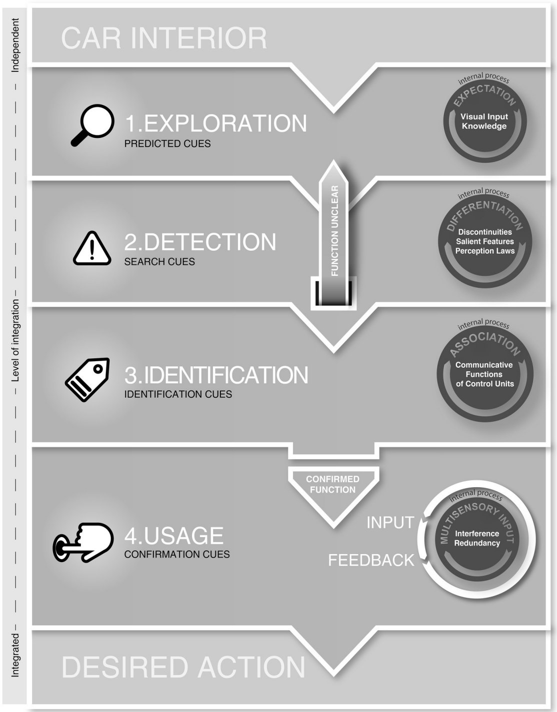

Figure 1.11: Theoretical framework of haptic processing in automotive user interfaces [57]

latter is taking an important place in haptic interaction in automotive applications. [57] defines a theoretical framework for haptic interaction in automotive interfaces. it consists in a model-based description of the haptic processing in the case of controlling a car's function, which describes four discrete phases (steps) that are crucial in the process. As illustrated in Figure 1.11, haptic interaction begins with an exploration phase initiated by the user's intention. This is followed by the detection phase, during which the user distinguishes interactive surfaces from purely decorative elements. Next is the identification phase, where the user selects the intended control element. Finally, the interaction culminates in the usage phase, during which the user manipulates the control element and receives confirmation via haptic feedback. More details about the framework and its guidelines can be found in the paper. Such complex haptic interaction cannot be achieved solely on surfaces haptics based on normal vibration methods. Friction control and net tangential forces represent an answer to the complex interaction described in the framework, but their integration still faces challenges.

The scope of this thesis is surface haptics based on mechanical vibrations specifically ultrasonic vibrations. We are going to present some of the challenges that integration of haptics based on mechanical haptic faces challenges.

While ultrasonic vibration is effective on small-scale interfaces, scaling this technology to larger areas—aligned with the framework guidelines—introduces several significant challenges:

- **Uniformity of Vibration**: Achieving consistent ultrasonic vibration across a large and complex (non-planar) surface is difficult. Inconsistent vibration amplitudes or frequencies can cause uneven friction modulation, where some areas perform optimally, while others experience diminished or even excessive friction.

- **Complexity of System Design**: Expanding ultrasonic vibration systems to larger surfaces increases design complexity. Factors such as transducer placement, control algorithms, and mechanical integration become more demanding, particularly on irregular or curved surfaces.

- **High Energy Consumption**: Operating ultrasonic actuators over extensive areas requires substantial energy, making it less suitable for energy-constrained or mobile applications.

- **Increased Vibration Mode Density**: Larger surfaces naturally exhibit a higher density of vibration modes. This complicates the task of selecting and controlling specific modes for generating targeted effects.

- **Difficulty in Mode Selection for Ultra-Shear Forces**: In applications requiring the superposition of two vibration modes to generate ultra-shear forces, the increased mode density makes precise mode selection and control far more challenging.

Each of these challenges needs to be addressed to successfully implement ultrasonic friction modulation on larger, more complex surfaces. Moreover, the integration this haptics based on mechanical vibrations into practical applications faces significant challenges related to boundary conditions, which affect the propagation and performance of ultrasonic waves.

Several potential solutions can be identified to address the challenges associated with vibration-based mechanical systems. These approaches aim to enhance performance, improve efficiency, and ensure adaptability in diverse applications. One such approach involves segmented vibration systems, which divide the surface into smaller, independently controlled regions. This segmentation allows for improved uniformity of vibrations and reduces energy consumption by targeting only the active areas that require modulation, while maintaining the boundary conditions respected. Another promising strategy is developing surfaces with optimized acoustic properties, to enhance wave propagation and minimize energy losses, thereby increasing the overall efficiency of the system. Together, these solutions offer a comprehensive framework for addressing current challenges and advancing the field of vibration-based technologies.

In this thesis, we aim to address the challenges of vibrations confinement and boundary conditions by focusing on the first approach: dividing a large surface into smaller, independently controlled segments.

The next section provides a brief overview of vibration confinement techniques, highlighting key methods and strategies used to control and localize vibrations within specific regions.

1.3 Overview of vibration confinement techniques

Vibration confinement is not just a goal for haptic applications; it is also a key challenge in various fields, particularly in vibration damping for structures. Solutions in this domain aim to limit the spread of vibrations or confine them to specific areas of a vibrating surface. Vibration localization techniques can be broadly classified into two categories: passive and active.

Passive localization relies on structural geometry to prevent vibration from propagating. These methods are typically less adaptable and cannot be adjusted once the structure is built. For example, the frequency range of attenuation is fixed and cannot be changed post-construction.

In contrast, active localization uses sensors and actuators to actively control vibrations. This approach offers greater flexibility, as it can be fine-tuned and reprogrammed after construction, allowing for adjustment of the vibration system.

in this section, a small overview of both type of methods, that can be related to surface haptics, is detailed.

1.3.1 passive methods

As previously mentioned, passive vibration localization techniques rely on geometry. For this purpose, [58] developed a specific geometry using narrow plates with a cutoff frequency below which bending waves become non radiate and do not propagate but remain confined around the actuator. This frequency corresponds to the resonance frequency of the first vibration mode. Figure 1.12 show the numerical simulation that was conducted on a narrow plate to analyze its behavior in the frequency domain. The results present the amplitude response at two distinct locations: the excitation point, denoted as

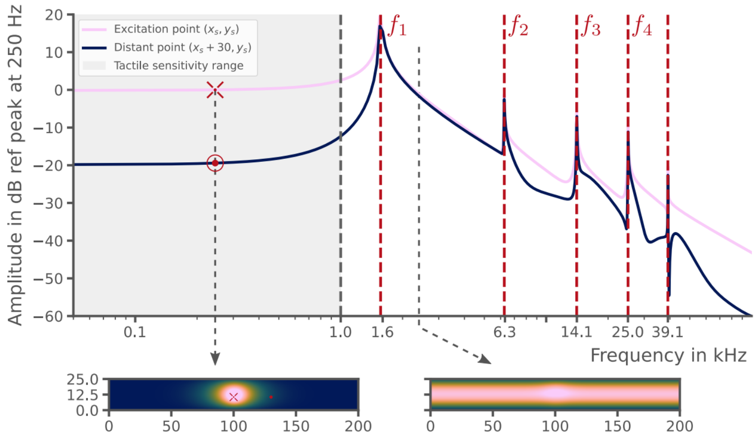

Figure 1.12: Numerical solution the narrow plate in the frequency domain [59]

(x_s, y_s), represented by the light pink curve, and a second point located 30 mm away along the x-axis, indicated by the dark blue curve. The simulation results demonstrate that, within the frequency range of 0 to 1.6 kHz, the plate exhibits non-propagative behavior. Beyond the first cut-off frequency, denoted as f_1, the plate transition into a propagative regime.

By arranging multiple narrow plates in a periodic pattern, a larger haptic surface can be created with localized vibrations [60].

Another approach to vibration confinement involves using structures known as "acoustic black holes" (ABH). Named after celestial black holes, which absorb all light waves, acoustic black holes are designed to dampen mechanical vibrations (see Figure 1.13b). The design of ABHs draws inspiration from gradient index (GRIN) lenses, originally proposed by Maxwell. GRIN lenses offer several benefits, including modified refractive properties, reduced aberrations, and easy integration [61, 62]. Based on these optical lenses, research has applied similar principles to elastic waves [63, 64]. An acoustic black hole acts as a mechanical vibration lens by gradually tapering the thickness of a thin plate while adding a damping layer, as shown in Figure 1.13a [65].

Another explored method is based on metamaterials, specifically periodic, locally resonant structures. Inspired by optical applications [66], [67] developed a structure with periodically placed pillars arranged to generate a waveguide. The periodic lattice structure creates a frequency band gap where the transmission coefficient of the vibration is nearly zero, preventing vibration propagation outside the waveguide, as shown in Figure 1.14.based on this idea, [68] developed a waveguide for ultrasonic vibrations to achieve localized haptics that confine vibration at a frequency of 60 kHz.

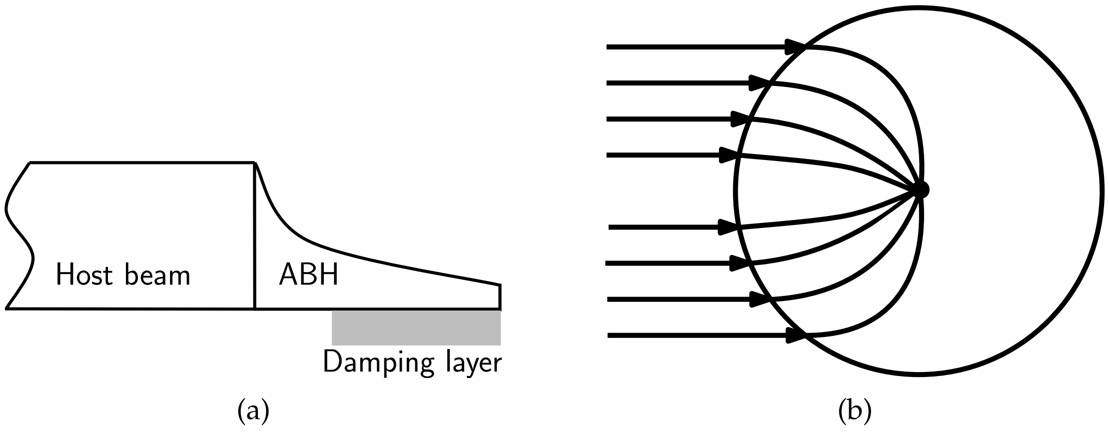

Figure 1.13: Acoustic black hole principle. a)ABH schematics .b) Vibration damping in ABH

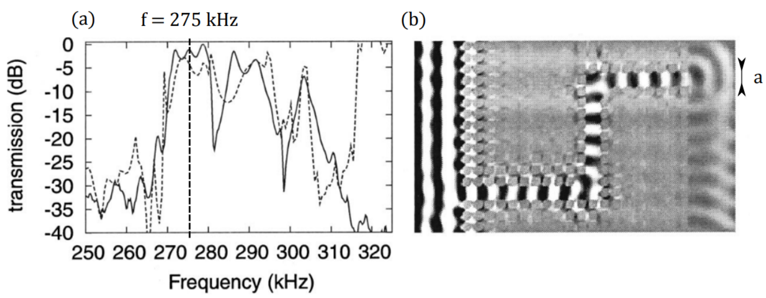

Figure 1.14: Acoustic waveguiding by a phononic crystal composed of cylindrical steel inclusions in water, as presented in [67]. (a) Experimental (solid line) and numerical (dotted line) transmission of the waveguide. (b) Numerically calculated displacements at frequency f=275 khz

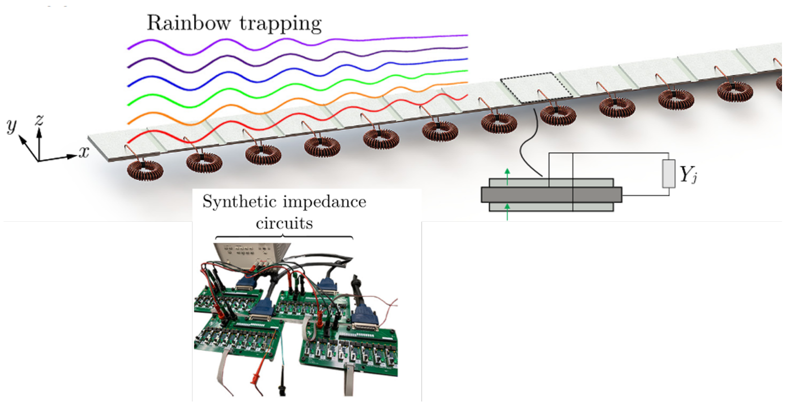

Figure 1.15: The frequency trapping device with it's synthetic impedance circuit [71]

1.3.2 Active methods

As previously discussed, active methods utilize actuators to actively control, limit, or confine the propagation of vibrations across a surface. In this context, [69] proposed a system in which multiple actuators were affixed to a vibrating surface. The vibration response at specific points on the surface was measured using a laser Doppler vibrometer. These measurements were performed for each actuator individually to characterize the system's dynamic behavior.

Based on the collected data, a transfer function matrix was established, representing the relationship between the input signals applied to the actuators and the resulting vibration amplitudes at the observation points. By inverting this transfer function matrix, it becomes possible to synthesize input signals for the actuators such that the vibration is concentrated at a specific point while being minimized elsewhere on the surface. This strategy is commonly referred to as the *inverse filter* technique.

Another approach to achieve vibration confinement is through the use of an active absorber, as demonstrated by [70]. This absorber consists of a piezoelectric transducer connected to a synthetic shunt resonant circuit, enabling vibration damping at a tunable frequency. Similarly, [71] applied this principle to a beam with multiple piezoelectric actuators affixed to it. By using synthetic impedance circuits, they tuned the shunt circuit of each actuator to a different frequency, allowing for the limitation of vibration propagation based on frequency, as illustrated in Figure 1.15. In addressing the complex problem of vibration confinement,the aforementioned solutions are tailored to specific application domains, limiting their broader applicability. This thesis aims to bridge that gap by developing a methodology that transcends domain-specific constraints, leveraging the versatility of electrical analogies as a unifying framework. In the next section, the proposed methodology is developed.

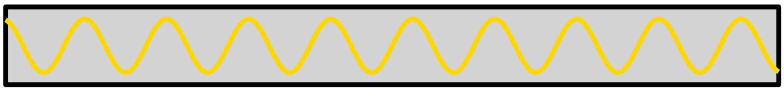

(a)

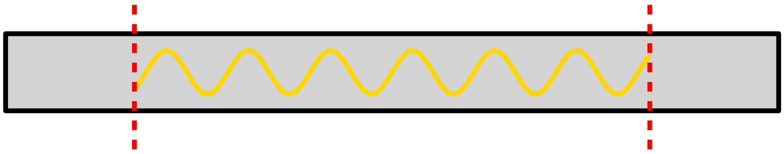

(b)

Figure 1.16: Vibration propagation in a beam. a) Normal vibration propagation. b) confined vibration propagation (dashed lines represent the emulated boundary conditions)

1.4 The Electrical Analogy based vibration confinement concept

Our aim in this thesis is to limit vibration propagation on a surface. To simplify the concept, in this part, we are going to introduce the general idea behind vibration confinement. When a beam is excited by an actuator (piezoelectric actuator for example), the vibration will be through all the surface. To be able to confine vibration in a part of the beam, we intent to emulate fixed boundary conditions on the surface to limit the vibrations at the desired frequency, as depicted on 1.16b. The emulated boundary conditions are presented with dashed lines. It means, at a specific frequency, we would have a small beam with fixed-fixed boundary conditions inside a larger beam with free-free boundary conditions. If the excited within the small boundary conditions , the vibration would not propagate beyond the emulated clamped-clamped boundary-conditions.

To emulate the boundary conditions, our concept in based on an electrical analogy of mechanical vibration propagation. The analogy was developed to overcome the complex calculation to find the wave equations in piezoelectric materials.In [72], the authors by uses the analogy from electrical network theory and presents an equivalent circuit that can be used for one dimensional analysis. The electrical analogues since then has been widely used to analyses and investigate vibrations behavior. This method is particularly useful in case of piezoelectric transducer since they have both mechanical and electrical properties. The technique was named after its author : *Mason's equivalent circuit*.

The aim of this analogy is to facilitate and illustrate the concept on which the vibration confinement can be based on.

Table 1.1: Analogy between mecahnical and electrical physical elements

Mechanical	**Electrical**
Force	Voltage
Velocity	Current

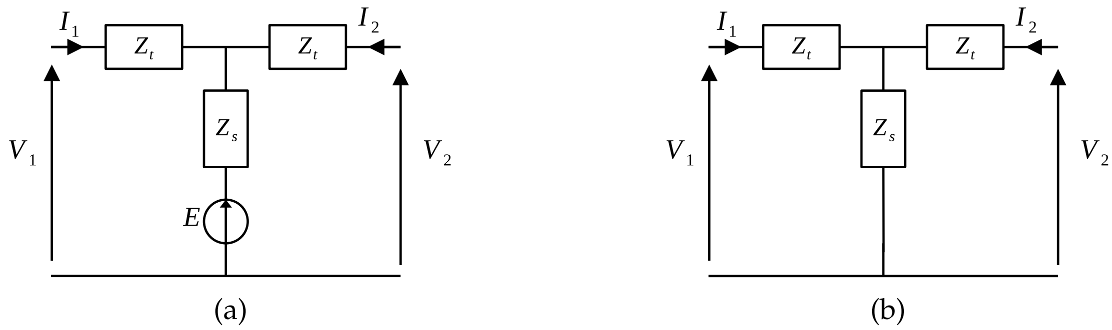

Figure 1.17: Mason's equivalent circuit. a) with piezoelectric force .b) without piezoelectric force

1.4.1 Mason's equivalent circuit

In this analogy, the mechanical forces or constraints are represented by voltages and the vibration amplitude is represented by the current intensities 1.1.

The mason's equivalent circuit is built upon this analogy, where a part or section of surface is modeled as a three port electrical circuit. This part or section is called "Cell". One port represents the electromechanical conversion using piezoelectric transducer, while the other two ports represents the boundary conditions on each side of the section as depicted in figure1.17a.

The electromechanical conversion is modeled as a voltage source, which corresponds to the force generated when a voltage is applied to a piezoelectric transducer. If no piezoelectric transducer is placed on the section, or if the actuator is not powered, the voltage source can be removed from the equivalent circuit, as shown in Figure 1.17b.

The electrical impedances Z_t,Z_s are in function of the geometry and mechanical properties of the cell as follows :

$$Z_T = iZ_0 tan(\frac{\Gamma l}{2}) \tag{1.1}$$

$$Z_s = iZ_0(\frac{1}{sin(\Gamma l)}) \tag{1.2}$$

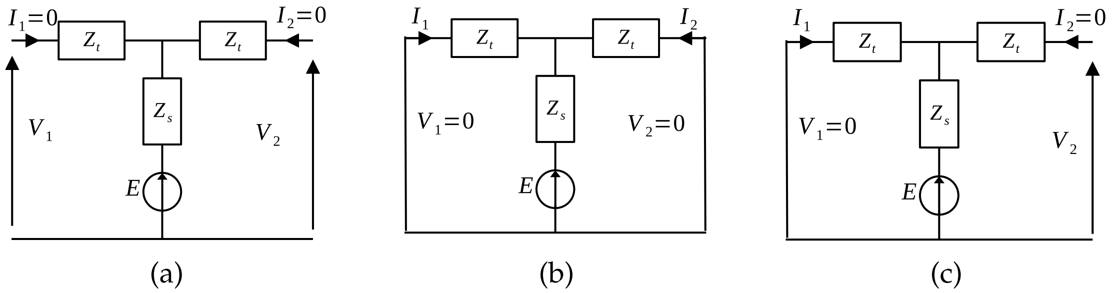

Figure 1.18: Mason's equivalent circuit boundary conditions : a) clamped-clamped. b) free-free. c) free-clamped.

where :

$$Zs_0 = A\sqrt{\rho C_{31}^D} \qquad \Gamma = \omega\sqrt{\frac{\rho}{C_{31}^D}}$$

The different parameters are in function of the considered material and cell such as :

- A The surface of the cell
- l The thickness of the cell
- ρ the density of the material
- C_{31}^D the rigidity of the material.

The electrical parameters V_1, I_1, V_2, and I_2 depend on the boundary conditions of the system. When the boundary conditions are free, it implies that there are no constraints, the force is null, which translate to to a short circuit in the Mason's model. Conversely, when the boundary conditions are clamped, there are no vibrations, and the current intensity becomes null, resulting in an open circuit. The various configurations of these boundary conditions are illustrated in Figure 1.18.

Moving forward, for the sake of simplifying the representation of our concept, a simplified representation of the cell is used. The representation encapsulate the different components of the equivalent circuit under a block representation.

This cell representation allows per example to easily represent a beam consisting of multiple sections,each one is represented by a cell as depicted figure 1.20a. In this example the beam presented in 1.16 can be divided into 5 cells.

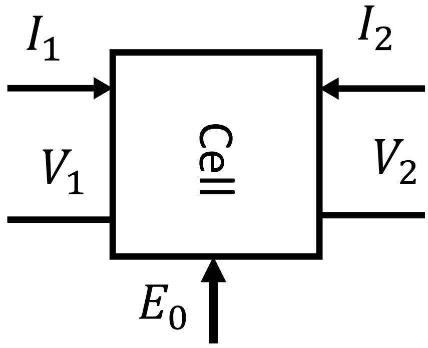

Figure 1.19: Cell representation

The boundary conditions are free-free which is represented by the short circuit at each end of the equivalent representation. Only the middle cell has a transducer attached to it and thus only this beam has the below input E_0. The equivalent circuit looks like a representation of transmission line in electrical network. We can use this representation to study the vibration behavior in the beam i.e find the vibration modes.

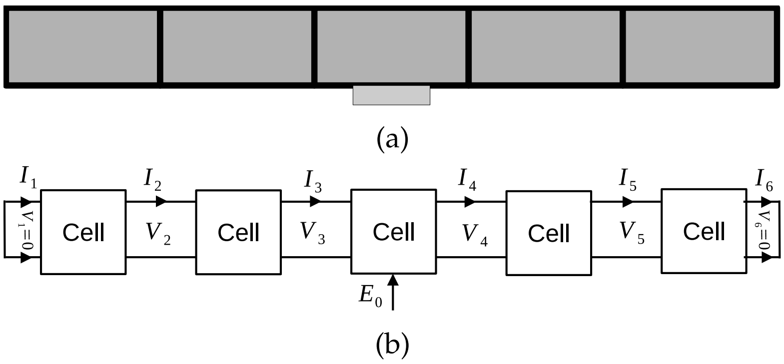

Figure 1.20: Beam representation using mason's equivalent circuit. a) A beam divided into 5 cells. b) the equivalent circuit of the beam

1.4.1.1 Mathematical model of a cell

The mathematical model of a cell is a general representation that does not account for specific boundary conditions, i.e., the model assumes that both voltages and currents are nonzero. It is formulated as a matrix-based system that defines the relationship between current and voltage at key points, specifically (V_1 , I_1),(V_2 , I_2) , and the piezoelectric force term E_0 if taken into account.

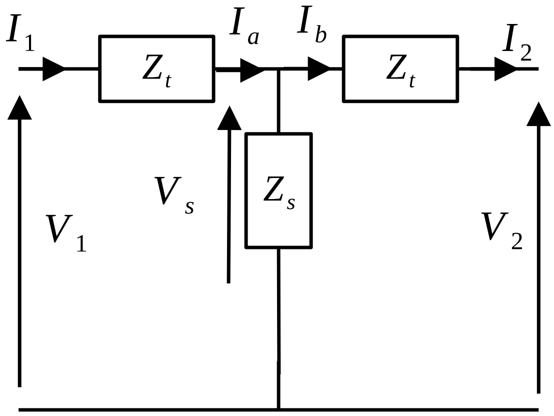

Figure 1.21: Mason'equivalent circuit with intermediary variables

To construct this model, we use the cell represented in Figure 1.21. The circuit includes intermediary current and voltage variables that help determine the desired model. Following this approach, we can establish the relationship between (V_1 , I_1) and (V_s , I_a) :

$$Vs = V_1 - Z_t I_a \tag{1.3}$$
$$I_a = Is \tag{1.4}$$

This system equations can be written on matrix form as follows :

$$\begin{bmatrix} V_1 \\ I_1 \end{bmatrix} = \begin{bmatrix} 1 & -Z_T \\ 0 & 1 \end{bmatrix} \begin{bmatrix} V_2 \\ I_a \end{bmatrix} = T_1 \begin{bmatrix} V_2 \\ I_a \end{bmatrix} \tag{1.5}$$

Then following the same method of work we establish the following relations:

$$\begin{bmatrix} V_s \\ I_b \end{bmatrix} = \begin{bmatrix} 1 & 0 \\ -\dfrac{1}{Z_s} & 1 \end{bmatrix} \begin{bmatrix} V_s \\ I_a \end{bmatrix} = T_2 \begin{bmatrix} V_s \\ I_a \end{bmatrix} \tag{1.6}$$

$$\begin{bmatrix} V_2 \\ I_2 \end{bmatrix} = T_1 \begin{bmatrix} V_s \\ I_b \end{bmatrix} \tag{1.7}$$

Based on (1.5),(1.6),(1.7) can be written as :

$$\begin{bmatrix} V_2 \\ I_2 \end{bmatrix} = T \begin{bmatrix} V_1 \\ I_1 \end{bmatrix} \tag{1.8}$$

where : $T = T_1 T_2 T_1$

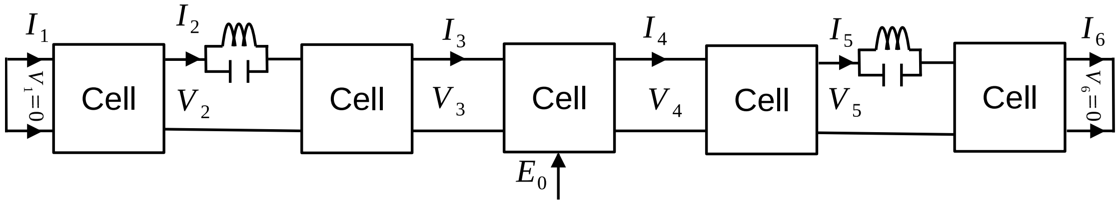

Figure 1.22: The beam equivalent circuit with added filters

The previous model is based on the fact that there is no piezoelectric force. In case of piezoelectric force the model becomes as follows :

$$\begin{bmatrix} V_2 \\ I_2 \end{bmatrix} = T \begin{bmatrix} V_1 \\ I_1 \end{bmatrix} + KE_0 \tag{1.9}$$

where $K = T_1 T_2 B$ with $B = \begin{bmatrix} 0 & \frac{1}{Z_s} \end{bmatrix}^T$

This cell model will allow for the calculation of vibration behavior of a beam represented by multiple cells.

1.4.2 The vibration confinement concept

As illustrated in Figure 1.20a, the analogy of a beam can be modeled as an electrical transmission line consisting of multiple impedances. At a given frequency, when a piezoelectric force is applied, the presence of current in certain sections of the transmission line corresponds to vibrations occurring in the equivalent regions of the beam, represented as discrete cells.

To achieve vibration confinement inside a specific regions of the beam, the current should be nonzero in designated branches while remaining null in others. However, due to the natural propagation of vibrations through the structure, the current—and consequently, the vibration—will generally not be null at any frequency unless specific modifications are introduced.

In electrical engineering, specialized components known as filters are designed to control the flow of current in circuits. In particular , band rejection filter show a large impedance ($Z = \infty$) at a specific resonance frequency. Inserting such filter in between two cells of a beam (figure 1.22) will cancel the vibration in the branch, hence confining the vibration in the selected cells.

In the next section, we illustrate this concept and we described the required to design the confinement.

In order to confine vibration mode in a part of a beam based on electrical analogy we are using the following three steps.

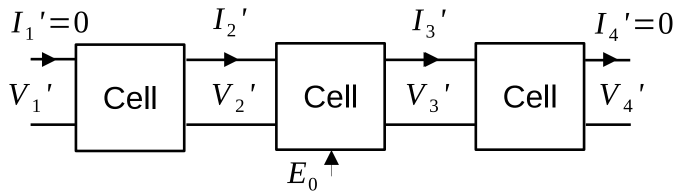

Figure 1.23: The three cells circuit with clamped-clamped boundary conditions

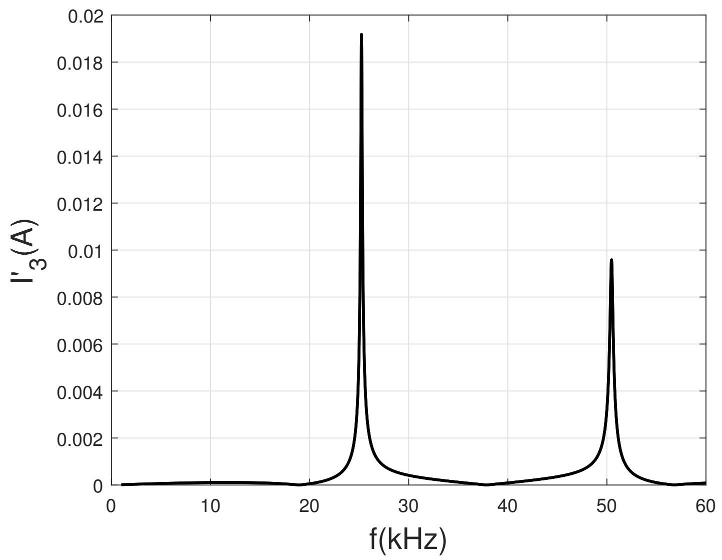

Figure 1.24: Frequency response of the current I_3' of the clamped-clamped 3 cells beam

1.4.3 Selecting the vibration mode to be confined

In a first step, we simulate the beam mode of the 3 selected cells, where the vibration confinement should occur, in this simulation, we isolate the selected cells, imposing clamped-clamped boundary conditions as depicted in figure 1.23.

Using the matrix representation and taking into account the boundary conditions, we simulate a frequency sweep from 10 Hz to 20 kHz. The currents analogous to the vibrations are calculated when a force is applied with E_0 =1 V. We analyze I_2' ($I_2' = I_3'$ due to symmetry conditions). The current presents several curve peaks in the frequency domain which are the resonance frequencies of the vibration modes. To be efficient, the vibrations should occur at the resonance frequency. We select an operating frequency at 25 kHz, corresponding to the first vibration mode.

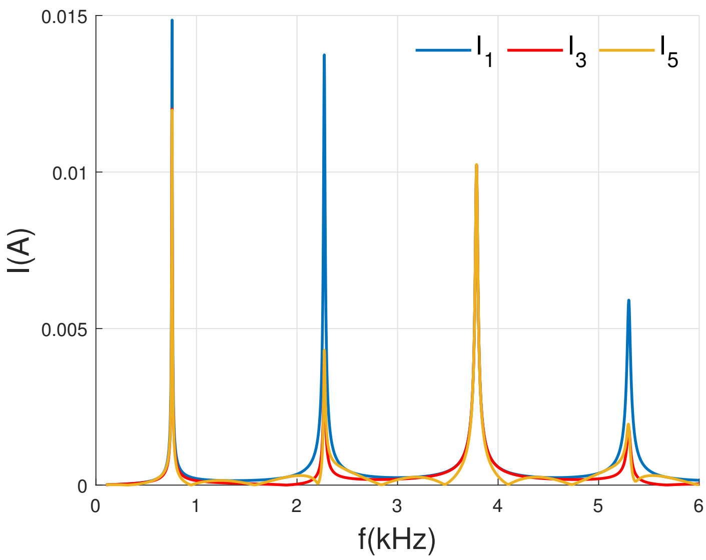

Figure 1.25: Frequency response of the current of the 5 cell beam in free-free conditions

Since we aim to generate the desired mode in 5-cell beam, we first examine the vibration modes of this beam under the same excitation applied at the center of the beam, but with free-free boundary conditions. Using the same procedure, we calculate the frequency response of the currents. Figure 1.25 illustrates the three currents I_3 ,I_3 and I_5. The currents exhibit identical peaks, corresponding to vibration modes at different frequencies. This observation confirms that vibrations propagate through all the cells of the beam. However, none of these modes match the target vibration mode that we aim to confine. This outcome is expected, as vibration modes are inherently dependent on the beam's length and boundary conditions.

1.4.4 The band-reject filter Design

The band-reject filter is specifically designed so that the resonance frequency of the mode we aim to confine falls within its rejection bandwidth. This ensures that vibration at the selected frequency is attenuated, allowing for the confinement of the desired mode. The filter consists of an inductance L and a capacitance C connected in parallel. Based on this configuration, the filter impedance can be described as:

$$Z_c = \frac{jL\omega}{1-\omega^2 LC} = j\frac{jG\omega}{1-\left(\frac{\omega}{\omega_0}\right)^2} \tag{1.10}$$

The values of L and C are not definitive, they are chosen accordingly to have a desired resonance frequency and gain.

The frequency response of the filter are shown in 1.26. the impedance of the filter presents a peak at that same frequency as the desired mode 25 kHz. Since the impedance at the resonance frequency is high , the current is interrupted at the filter.

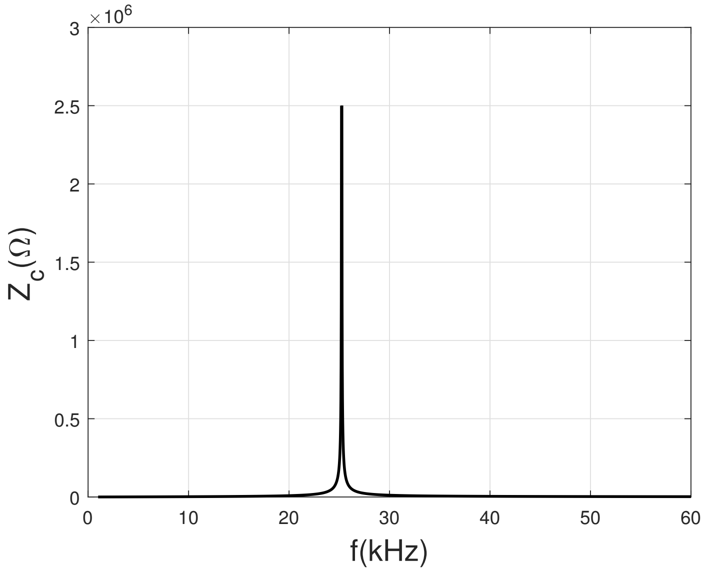

Figure 1.26: Impedance of the band-rejection filter with a resonance frequency of 25 kHz. a Resistor R =100 MΩ has been introduced to allow the calculation of Z_c

1.4.5 Simulation of the beam with filter included

After selecting the desired mode and designing the filter accordingly, we calculate the frequency response of the beam with the filter included, using the same excitation applied at the middle of the beam. The currents, both before and after the filter, are computed and presented in Figure 1.27. The frequency response of the currents reveals several peaks, so several vibration modes. Upon closer examination, the currents I_1 and I_2 exhibit similar vibration modes to those previously calculated in the beam without the filter. In addition to these modes, the current I_4 displays an additional vibration mode that corresponds to the selected vibration mode we aimed to confine. This result shows that the filter, within its rejection bandwidth, successfully emulates and enforces clamped boundary conditions, effectively confining the desired vibration mode.

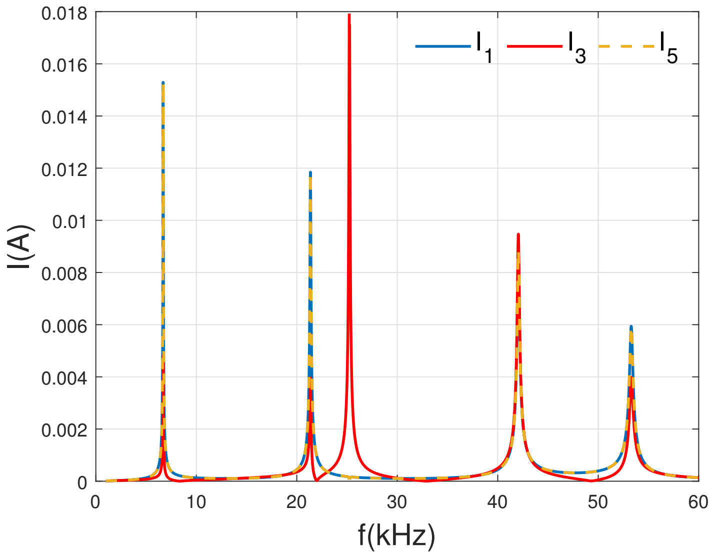

Figure 1.27: Frequency response of the current of the 5 cell beam in free-free conditions with the filter

The calculations based on Mason's equivalent circuit form the foundation of our theoretical framework for developing vibration confinement techniques. These calculations demonstrate how the designed filter can emulate and enforce boundary conditions on specific regions of the system, enabling targeted control of vibrations. In the following sections, we will showcase how this theoretical concept was used to develop both passive and active prototypes for vibration confinement, highlighting their design and practical implementation.

1.4.6 Implementation of the concept

Starting from the electrical analogy concept for vibration confinement , two prototype for vibration confinement were developed, this thesis. The first one is based on geometry while the other is based on active strategy .

Passive vibration confinement To develop passive vibration confinement, a geometry equivalent to a resonant filter with a selective bandwidth can be utilized. The selected geometry is a square pillar, which can be integrated into the vibrating surface to function as a resonant filter. Its application to a beam is illustrated in Figure 1.28, demonstrating how the concept can be implemented in a simplified structure. Furthermore, this thesis explores the extension of this approach to larger surfaces, such as plates, to evaluate its effectiveness in more complex scenarios. The design and implementation of the prototype will be detailed in Chapter 2.

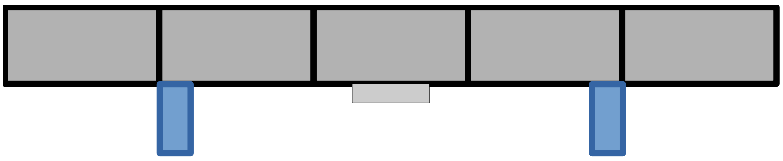

Figure 1.28: Example of passive vibration confinement on a beam using pillars.

active vibration confinement To achieve active vibration confinement, a control system is employed to dynamically manage vibrations within the desired regions. As explained before, instead of relying on geometry, active methods use sensors and actuators to monitor and modify the vibration response in real time. For this purpose, piezoelectric actuators and sensors can be placed on the vibrating surface to apply targeted forces that counteract or shape the vibrations.The force references are calculated by a control law as it's shown in Figure 1.29, demonstrating how active control can be used to confine vibrations to specific areas in a beam. In this thesis, we develop a an active method that can be used and implemented on a beam . The design and functionality of the active vibration confinement prototype will be presented in Chapter 3.

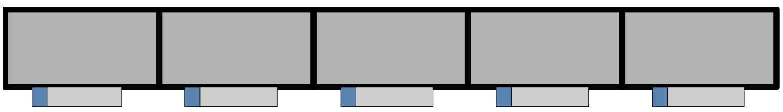

Figure 1.29: Example of active vibration confinement on a beam using sensors (in blue) and actuators(in light grey).

1.5 conclusion

This chapter began by examining various haptic technologies, with a particular focus on those based on mechanical vibrations. It highlighted the key challenges these technologies faces, which hinder their widespread adoption and integration. Vibration confinement emerged as a potential solution to address some of these challenges. To explore this further, we investigated several approaches to vibration confinement, applicable not only to haptic applications but also to broader contexts.

We then introduced a theoretical framework for vibration confinement, rooted in electrical analogies. By leveraging specially designed filters capable of imposing specific boundary conditions, we demonstrated an effective strategy for confining vibrations to desired regions. Toward the end of the chapter, we presented a passive vibration confinement method, which serves as a practical application of this concept. The design and implementation of this method will be detailed further in the next chapter.

2 Design of passively confined vibrations

2.1 Introduction

In this chapter, we focus on the practical implementation of the passive vibration confinement method introduced in the previous chapter. Building on the theoretical framework, we outline the design and development of a passive prototype that employs geometries equivalent to resonant filters with selective bandwidths.

The chapter begins with a discussion of the design methodology, detailing the chosen structure of the prototype and the step-by-step process used to create it. Following this, we evaluate the performance of the passive vibration confinement method by presenting results obtained through both experimental testing and numerical simulations. These results demonstrate the effectiveness of the design in confining vibrations.

2.2 Prototype Design and Vibration Confinement Strategy

As illustrated in Figure 2.1.a, the prototype developed in this study is designed to generate localized vibrations within a defined region of the plate, referred to as the active zone (outlined in blue), in order to provide targeted haptic feedback. To suppress vibrations outside this region—particularly on areas where no lubrication or tactile stimulation is desired—pillars are strategically positioned on the opposite side of the passive surfaces (outlined in green).

As discussed in the previous chapter, these pillars function as resonant mechanical filters. Under appropriate design conditions, they are capable of attenuating the propagation of vibration modes. The primary aim is to ensure

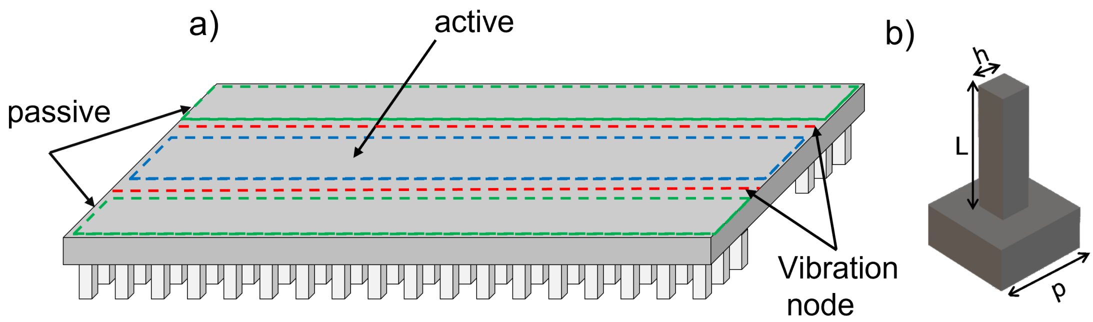

Figure 2.1: (a) Schematic of the studied prototype. The active vibration zone is outlined in blue. (b) Representation of the pillar and the periodic unit cell.

that, within the operating frequency band used for friction modulation, vibrations are effectively confined to the active zone, thereby minimizing unwanted vibrations in the passive areas.

The objective is to use the pillars to replicate a clamped boundary condition at the interface between the active and passive zones. If the added pillars exhibit a bending vibration mode at the same frequency as the targeted confined mode within the active zone, an energy transfer occurs between these two modes, a phenomenon known as mode conversion. This energy exchange restricts vibration propagation beyond the designated region. By carefully selecting the geometric parameters of the pillars, it is possible to optimize this effect, effectively confining vibrations within the active zone for the selected mode [73].

The design of this system is complex and does not have simple straightforward analytical solutions. Therefore, a design method where the dimensions of the active zone and the pillars are considered separately . This method consists of three key steps:

- **Defining the active zone**: The first step involves isolating the active zone from the passive areas. In this step , the two boundary interfaces between these regions are treated as clamped. The haptic application requires some constraints such as : the vibration mode with a frequency higher than 25 kHz so that it can be ultrasonic with a half-half-wavelength smaller than the width of a finger estimated at 20 mm [74].

- **Determining the pillar dimensions**: For effective energy transfer, one of the pillar's bending mode resonance frequencies (considered in isolation) must coincide with the selected mode frequency of the active zone. To maximize this transfer while minimizing the pillar size, we focus on the first bending mode.

To facilitate the manufacturing process, the pillars in this study are designed with a square prismatic shape, resulting in two identical modal deformations along each symmetry axis.

Beyond geometric considerations, the pillar is modeled with clamped-free boundary conditions, assuming that displacements are imposed at the interface between the pillar and the surface. Additionally, studies on the coupling of beam resonators to a surface have shown that the resonance frequencies of the connected beam closely approximate those of a clamped-free beam, though they consistently appear slightly lower .

- **Establishing the placement of the pillars**: the performance and effectiveness of vibration confinement depend on the periodic arrangement of the pillars—specifically, the distance between adjacent pillars, referred to as the periodicity. This periodicity is characterized by two distinct parameters corresponding to the spacing along the x-axis and y-axis of the plane.

  To simplify the design process and reduce the number of influencing variables, a symmetric periodic cell is chosen. In this configuration, the spacing between pillars is identical in both directions (p in figure 2.1), ensuring uniform periodicity across the structure.

  In addition to the periodicity, another critical parameter that significantly influences vibration confinement is the number of pillar rows surrounding the active zone. If too few rows are implemented, the attenuation of propagating vibrations may be insufficient, allowing energy to leak into the passive areas. Conversely, increasing the number of rows improves the attenuation of propagating vibration modes by reinforcing the periodic structure and creating a more effective barrier especially at the desired frequency.

Once the prototype is fully defined, piezoelectric ceramics are strategically positioned at the antinodes of the selected vibration mode. Ideally, each ceramic element spans a subdomain bounded by nodal lines to ensure maximum coupling with the targeted mode while minimizing energy transfer to adjacent, undesired modes [75]. To further enhance electromechanical efficiency, the polarization direction of each ceramic is aligned with the local strain field.

However, practical constraints arise from the geometry and standard dimensions of commercially available ceramics, which may prevent precise spatial alignment with the modal antinodes. Moreover, due to the proximity of neighboring modes with similar spatial profiles, spatial selectivity alone is insufficient to ensure mode isolation. To address this, the excitation frequency is carefully tuned to match the resonance frequency of the targeted mode. This frequency-based selectivity enhances energy transfer into the desired mode and suppresses the activation of competing modes. Prior to conducting numerical simulations, we begin with analytical calculations based on Euler-Bernoulli beam theory. This method offers an initial design that can be verified and refined later through finite element numerical simulations.

2.3 Preliminary Analytic Design

Analytical pre-design constitutes an essential preliminary step prior to finite element simulations. It provides order-of magnitude estimations and explicit relationships between geometric parameters, material properties, and system performance, relying on simplified yet insightful assumptions. These analytical models not only guide the initial dimensioning process but also enhance physical understanding of the problem and offer a benchmark for identifying potential numerical inaccuracies. Once the analytical framework is established, finite element analysis (FEA) can be employed to refine the design by relaxing initial assumptions, incorporating complex boundary conditions, and enabling performance optimization.

The designs of the pillar and the active zone are based on complementary physics-based analytical models aimed at isolating and controlling their respective vibrational behaviors. The pillar geometry is determined using Euler-Bernoulli beam theory to ensure that the first bending mode resonates at the desired target frequency. In contrast, the active zone is modeled using Kirchhoff-Love plate theory. A kinematically admissible displacement field is assumed in the form of a separable function $F(x, y) = f(x).g(y)$, where $f(x)$ enforces pinned boundary conditions at the interface. Substituting this ansatz into the governing plate equations enables the identification and confinement of specific vibration modes. Together, these analytical models provide a structured pre-design framework that guides the subsequent finite element method (FEM) simulations used for refinement and validation.

2.3.1 Euler-Bernoulli Beam Theory

The Euler-Bernoulli beam theory, also known as the classical beam theory or engineer's beam theory [76], is a fundamental theory used to describe the behavior of beams under bending loads. Bending refers to the deformation of a structural element (e.g., a beam or plate) under transverse loads, causing curvature along its length.

The theory simplifies the analysis of beam deflections, stresses, and strains by making several assumptions about the beam's geometry, material properties, and loading conditions. The key assumptions of this theory are [77] :

1. **Plane Sections Remain Plane**: Cross-sections of the beam remain flat and perpendicular to the neutral axis after deformation.

2. **Small Deflections**: The deflections of the beam under loading are small compared to the beam's length, allowing linear approximations for deformation.

3. **Elastic Material**: The material of the beam is assumed to follow Hooke's Law, meaning the material behaves elastically, and stress is proportional to strain.

4. **No Shear Deformation**: The beam deforms only through bending, neglecting shear deformation.

5. **Constant Young's Modulus and moment of inertia**: The Young's Modulus of the material and the moment of inertia are constant along the length of the beam.

6. **Neutral Line** : Neutral Line: The neutral line refers to the material layer within the cross-section of a beam that experiences zero longitudinal strain during bending. In symmetrically loaded and homogeneous beams, this line coincides with the centroidal axis. It remains unstressed and unstretched, separating the compressed and tensioned regions of the beam under bending deformation.

Based on these assumptions, the governing differential equation for the transverse vibration of a homogeneous beam with constant section is:

$$EI\frac{d^4w(x,t)}{dx^4} + \rho A\frac{\partial^2 w(x,t)}{\partial t^2} = 0 \tag{2.1}$$

where:

- $w(x,t)$ is the transverse displacement as a function of position x and time t,
- E is the Young's modulus,
- I is the second moment of area of the beam's cross-section,
- ρ is the density of the material,

- A is the cross-sectional area.

This equation governs the dynamic response of the beam, with its behavior being intrinsically linked to its geometry, material properties, and—critically—its boundary conditions. The analysis is carried out in two sequential phases. First, the associated eigenvalue problem is solved to determine the system's natural frequencies. Second, the corresponding spatial mode shapes are derived, providing insight into the deformation patterns associated with each resonant frequency.

2.3.1.1 Natural frequencies of a beam

To determine the natural frequencies and normal modes for the beam , we employ separation of variable , thus we let the general solution:

$$w(x,t) = \phi(x)T(t) \tag{2.2}$$

Substituting this into the governing equation (2.1) gives:

$$\frac{a^2}{\phi(x)}\frac{d^4\phi(x)}{dx^4} = \frac{1}{T(t)}\frac{d^2T(t)}{dt^2}, \quad a^2 = -\frac{EI}{\rho A} \tag{2.3}$$

Since the left-hand side depends only on the space variable x and the right-hand side depends only on the time variable t, both must equal a constant, say λ:

$$\frac{a^2}{\phi(x)}\frac{d^4\phi(x)}{dx^4} = \lambda, \quad \frac{1}{T(t)}\frac{d^2T(t)}{dt^2} = \lambda \tag{2.4}$$

Thus , for T we have :

$$T(t) = A\cos(\omega t) + B\sin(\omega t) \tag{2.5}$$

where $\omega^2 = \lambda$ is the natural angular frequency.

The general solution to the beam vibration equation can be represented in various forms. For homogeneous beams with constant cross-sectional properties, the spatial component of the displacement field, denoted by $\phi(x)$, is most conveniently expressed as:

$$\phi(x) = C_1\sin(\beta x) + C_2\cos(\beta x) + C_3\sinh(\beta x) + C_4\cosh(\beta x) \tag{2.6}$$

where $\beta^4 = \omega^2/a^2$.

While the general form of the solution does not inherently satisfy boundary conditions, our pillar is modeled as a clamped-free (cantilever) beam. To determine the natural frequencies and corresponding mode shapes, these specific

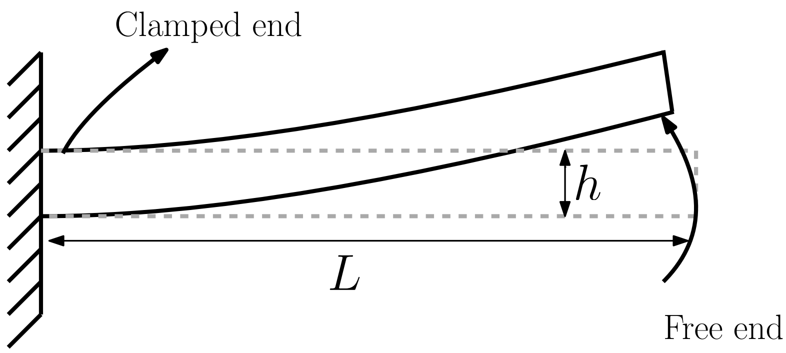

Figure 2.2: Representation of a cantilevered beam.

boundary conditions are explicitly applied to the general solution. This process yields a discrete set of admissible solutions—each associated with a particular resonance frequency—that satisfy both the governing differential equation and the physical constraints at the beam's boundaries.

The corresponding boundary conditions as represented in 2.2 are expressed as follows:

Clamped end (x=0):	**Free end (x=L):**
$\phi(0) = 0,$	$EI\dfrac{d^2\phi}{dx^2}(L) = 0,$
$\dfrac{d\phi}{dx}(0) = 0$	$EI\dfrac{d^3\phi}{dx^3}(L) = 0$

Using the solution from (2.6), we get the following equation:

$$\cos(\beta l)\cosh(\beta l) = -1 \tag{2.7}$$

where β denotes the eigenvalue. The roots for this equation are :

$$\beta_1 l = 1.87510, \quad \beta_2 l = 4.69409, \quad \beta_3 l = 7.85473, \quad \text{for } i > 3 \quad \beta_i = (2i-1)\frac{\pi}{2} \tag{2.8}$$

where n is the vibration mode order.

Once determined, these solutions establish a direct relationship between the resonance frequencies and the geometric and material properties of the beam, typically expressed through the characteristic equation:

$$f_n = \frac{(\beta_n l)^2}{2\pi}\sqrt{\frac{EI}{\rho A l^4}} \tag{2.9}$$

Taking into account the geometry of our active zone and pillars, that is rectangular cuboid, we write :

$$\begin{aligned} A &= bh \\ I &= \frac{1}{12}bh^3 \end{aligned} \tag{2.10}$$

by replacing (2.10) in (2.9), we have:

$$f_n = \frac{(\beta_n l)^2}{2\pi} h \sqrt{\frac{E}{12\rho}} \tag{2.11}$$

Equation (2.3.1.1) establishes a relationship between the beam's geometric parameters (length and height) and β_n, which is inherently linked to the order of the vibration mode. Based on this equation, preliminary calculations can be performed to guide the design of the pillars, ensuring that their dimensions align with the desired vibration mode and frequency.

2.3.2 Thin plate vibration theory

Thin Plate Theory models the vibration behavior of slender, flat structures by applying the Kirchhoff–Love kinematic assumptions. This framework is particularly valid when the plate thickness hh is much smaller than its in-plane dimensions, i.e., $h <<$ plate length and width as represented in Figure 2.3. It simplifies the governing equations based on the following core idealizations:

- **Geometric Simplification:** Transverse shear deformations are neglected, reducing the three-dimensional elasticity problem to a two-dimensional one. This is justified when the plate is sufficiently thin.
- **Linearized Dynamics:** Small-amplitude vibrations allow the use of linear strain–displacement relationships, thereby enabling the application of modal superposition principles.
- **Material Continuity:** While the theory is general enough to incorporate heterogeneous or anisotropic materials (such as laminated composites), we restrict the analysis to homogeneous and isotropic materials, characterized by constant Young's modulus E, Poisson's ratio μ, and mass density ρ, for analytical clarity and tractability.

To extract the vibration modes, a separable displacement field of the form

$$w(x, y, t) = F(x, y).T(t) \tag{2.12}$$

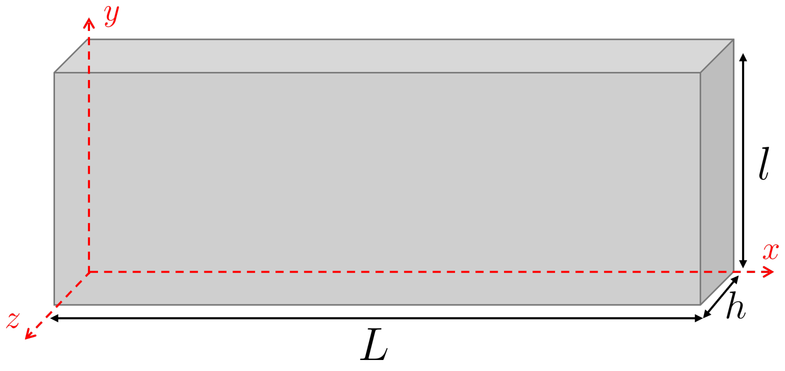

Figure 2.3: Schematic of a rectangular plate showing in-plane dimensions L, l and thickness h.

is assumed. The spatial component $F(x, y)$ captures the mode shape, while $T(t)$ describes the temporal dynamics. Although this ansatz imposes restrictions, it remains valid under separable boundary conditions. In our case, the active zone geometry—with clamped interfaces and free lateral edges—satisfies these conditions, justifying the use of this modal decomposition.

The transverse bending vibration of the plate is governed by the Kirchhoff-Love equation, expressed in terms of the out-of-plane displacement $w(x, y, t)$:

$$\rho h \frac{\partial^2 w}{\partial t^2} + D\nabla^4 w - \sigma(x, y, t) = 0 \tag{2.13}$$

where:

$$\nabla^4 \equiv \frac{\partial^4}{\partial x^4} + 2\frac{\partial^4}{\partial x^2 \partial y^2} + \frac{\partial^4}{\partial y^4} \quad \text{(biharmonic operator)},$$

$$D = \frac{Eh^3}{12(1-\nu^2)} \quad \text{(flexural rigidity)},$$

$$\sigma(x, y, t) : \text{external in-plane stresses}\ .$$

The pursuit of spatially confined vibration modes leads us to consider$(0, N)$ modal configurations, where the mode shape exhibits no nodal lines along the yy-direction while maintaining N nodal lines along x. This particular choice offers dual advantages: the x-wise uniformity ensures consistent vibration amplitude across the contact surface, while the xx-direction wavelength $\lambda_x \approx \frac{L_x}{N}$ can be tuned to match the fingertip's characteristic dimensions (typically 10-20 mm) through appropriate selection of N.

To engineer such modes, we construct an ansatz derived from the general solution for rectangular plates with separable boundary conditions. The spatial component of the $(0, N)$ mode takes the form [77]:

$$w(x, y, t) = X(x)\, Y(y)\, T(t) \tag{2.14}$$

To enforce nodal lines at the boundary between active and passive zones, the ansatz function is constructed by incorporating the first-mode solution of a simply supported beam: :

$$Y(y) = \sin\left(\frac{\pi}{l} y\right) \tag{2.15}$$

where l is the plate width in the x–direction. The sine function is chosen to satisfy the boundary conditions in x, such as those corresponding to simply supported edges:

$$Y(0) = 0 \qquad Y(l) = 0 \tag{2.16}$$

Thus the spatial component become :

$$w(x, y, t) = X(x)\, T(t)\, \sin\left(\frac{\pi}{l} y\right), \tag{2.17}$$

Substituting the assumed form (2.17) into Eq. (2.13) and separating variables, we obtain an ordinary differential equation (ODE) for the x–dependent function:

$$\frac{\partial^4 X(x)}{\partial x^4} - 2\left(\frac{\pi}{l}\right)^2 \frac{\partial^2 X(x)}{\partial x^2} + \left[\left(\frac{\pi}{l}\right)^4 - \frac{\lambda}{D}\right] X(x) = 0, \tag{2.18}$$

where λ is a constant.

While the yy-dependent component of the ansatz (2.15) ensures that the displacement is zero on the line separating the passive and active area of the display, the xx-directional behavior must accommodate free-edge boundary conditions to match the plate's physical constraints. For this, we adopt the modal solution of a free-free Euler-Bernoulli beam, which inherently satisfies:

$$\text{Free-edge BCs:} \quad \left.\frac{d^2 X}{dx^2}\right|_{x=0,L} = \left.\frac{d^3 X}{dx^3}\right|_{x=0,L} = 0. \tag{2.19}$$

given by:

$$X(x) = A\Big[\cosh(kx) - \cos(kx)\Big] + B\Big[\sinh(kx) - \sin(kx)\Big] \tag{2.20}$$

where k is the wavenumber along y. Enforcing the free-edge conditions yields the characteristic equation:

$$\cosh(kL)\cos(kL) = 1. \tag{2.21}$$

This equation governs the permissible wave-numbers k for the system's resonant modes. Its solutions are well-documented for free-free beams, providing explicit kL values for mode-shape determination.

Substituting the spatial solution (2.20) into the plate equation (2.18) yields the eigenvalue relation:

$$\lambda = D\left[\left(\frac{\pi}{l}\right)^4 + 2\left(\frac{\pi}{l}\right)^2 k^2 + k^4\right]. \tag{2.22}$$

where λ couples the spatial and temporal dynamics. The time-dependent component $T(t)$ then obeys:

$$\frac{\partial^2 T(t)}{\partial t^2} + \frac{\lambda}{\rho h} T(t) = 0, \tag{2.23}$$

which describes a simple harmonic oscillator with angular frequency

$$\omega = \sqrt{\frac{\lambda}{\rho h}}. \tag{2.24}$$

Substituting Eq. (2.22) into Eq. (2.24), we obtain the resonance frequency expression:

$$f = \frac{1}{2\pi}\sqrt{\frac{D}{\rho h}\left[\left(\frac{\pi}{l}\right)^4 + 2\left(\frac{\pi}{l}\right)^2 k^2 + k^4\right]}. \tag{2.25}$$

This expression directly links the geometric parameters (length l, thickness h) and material properties (E, ρ) to the wavenumber k, which is determined by the mode order N through the boundary conditions.

Once the theoretical foundations underlying the analytical design have been established, we proceed to the detailed design of both the active zone and the resonant pillars.

2.3.3 Design

The relationship between resonance frequency and the target vibration mode order is influenced by multiple interdependent parameters. To reduce complexity, we impose the following fixed constraints:

- **Shared material properties:** Both the active zone and the pillars are designed using the same Young's modulus (E) and the mass density (ρ).
- **Common geometric constraint:** A constant plate thickness of $h = 2, \mathrm{mm}$ is assumed across all components.

the Remaining parameters are optimized independently for each design case.

Active zone design : For the active zone, the objective is to generate a vibration mode with a half-wavelength below 20 mm, while maintaining a sufficient length (115.5 mm) to accommodate natural finger exploration during user interaction. With the material properties and plate thickness fixed at $h = 2\,\mathrm{mm}$, the width is set to $l = 20\,\mathrm{mm}$ to match the dimensions of the available piezoelectric ceramics—allowing for one ceramic per antinode.

To obtain the target spatial resolution, we select a vibration mode with eight nodes along the length under free-free boundary conditions. This modal configuration results in a resonance frequency of $f_a = 32\,\mathrm{kHz}$, which aligns with our confinement and haptic feedback design objectives.

Pillar design : The pillar, featuring a square base, is dimensioned to ensure that its first bending mode under clamped-free boundary conditions resonates at the target frequency of the active zone, namely 32 kHz. Based on this resonance criterion and the fixed material and geometric parameters, the required pillar height is determined to be 7.1 mm.

The analytically derived dimensions are validated and refined via **finite element method (FEM) simulations**, ensuring accurate prediction of resonance frequencies and mode shapes. This step accounts for manufacturing tolerances and secondary effects neglected in the semi-analytical model.

2.4 Finite element simulation

The finite element analysis serves two critical roles: (1) refining the resonance frequency predicted by the simplified analytical model, and (2) validating vibration confinement. While the semi-analytical approach provides initial dimensioning with an expected $\pm 5\%$ frequency error, the FEM simulation—free from Kirchhoff-Love plate assumptions—delivers precise modal analysis.

We first compute the active zone's resonance using a 3D FEM model that accounts for shear deformation and edge effects. This corrected frequency then guides pillar tuning through a second FEM study, ensuring perfect matching between the pillar's first clamped-free bending mode and the operational frequency.

All simulations were carried out using SALOME-MECA/CODE-ASTER, assuming linear elastic, homogeneous, and isotropic material behavior. The structure was modeled in pure aluminum, with material properties given in Table 2.1. This two-stage verification, combining numerical analysis and experimental prototyping, ensures a consistent link between the design phase and the final prototype.

Table 2.1: Mechanical properties of Aluminum

Aluminum Properties	
Young's Modulus E	70 GPa
Density ρ	2.7 kg L^{-1}
possion ration	0.34

2.4.1 Analytical design validation

We start by designing and simulating both the active zone and the pillars.

Active zone simulation: Our preliminary design, developed to meet the required specifications, defines the active zone as a plate with dimensions 115.5 mm × 20 mm × 2 mm.A modal Finite Element Method (FEM) analysis was carried out to identify the vibration modes of the structure. The model was constructed using a tetrahedral mesh and applied boundary conditions corresponding to clamped edges along the yy-direction and free edges along the xx-direction. This configuration replicates the physical constraints of the prototype and enables accurate characterization of its modal behavior. The simulation revealed multiple vibration modes, one of which occurs at 38 kHz. The corresponding mode shape, illustrated in Figure 2.4a, exhibits eight nodes with a half-wavelength of approximately 13 mm, aligning with the design objectives.

However, a 6 kHz discrepancy was observed between the FEM results and the analytical calculations. This difference can be attributed to the assumed mode shape along the x-axis, which deviates from a purely sinusoidal function, as shown in Figure 2.4c. Nevertheless, the displacement along the y-axis confirms that the vibration mode adheres to the free-free boundary conditions, validating the overall design approach (Figure 2.4b).

A 6 kHz frequency offset (20%) occurs due to mismatched x-axis boundary conditions (analytical: simply-supported; FEM: near clamped). However, the y-axis response maintains free-free characteristics as modeled (Figure 2.4b), and x-direction mode shapes show qualitative agreement (Figure 2.4c). While this confirms that the approach captures key physics, exact frequency prediction requires boundary condition alignment. However, real-world performance stems from energy transfer between plate and pillar modes, not idealized edge conditions. Thus, refining the ansatz is unnecessary since, in practice collective resonators behavior (pillars) outweighs individual boundary effects.

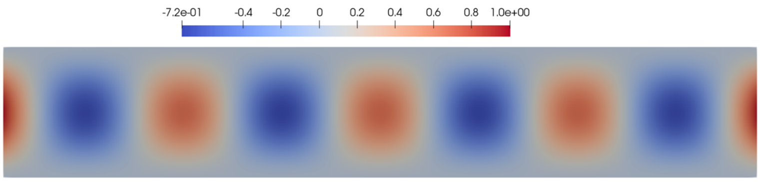

(a) desired Mode shape

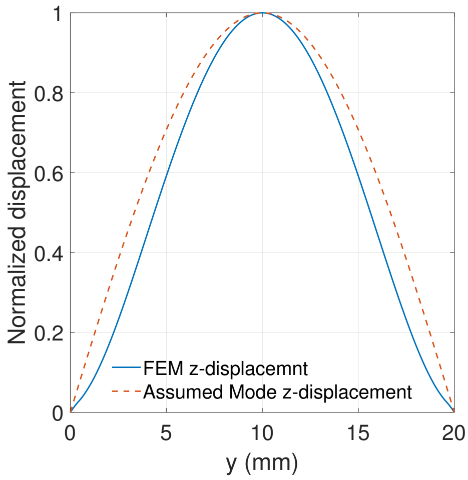

(b) Displacement in the y-direction

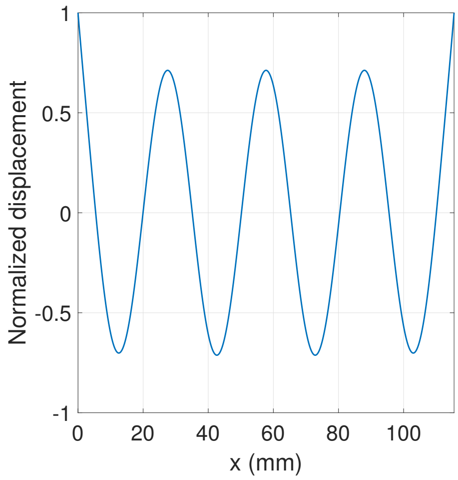

(c) Displacement in the x-direction

Figure 2.4: FEM simulation of the active zone at 38 kHz

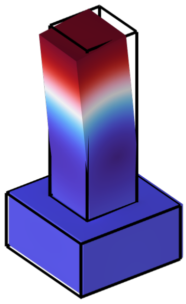

Figure 2.5: First bending mode of the pillar at 38 kHz. Displacement is scaled up for visualization.

the pillar zone simulation: On the other hand, regarding the pillar design, the primary objective is to ensure that its first vibration mode coincides with the frequency of the selected mode of the active zone. Under these constraints, we must update our analytical design to match the 38 kHz. The new analytical design process led to a pillar with dimensions 2 mm $\times$ 2 mm $\times$ 6.5 mm.

Subsequent finite element method (FEM) simulations were conducted. The results showed that the first bending mode of the pillar occurred at 35 kHz. Fine tuning the design to match the desired resonance frequency lead to a pillar of 2 mm $\times$ 2 mm $\times$ 6.3 mm.

Figure 2.5 illustrates the mode shape of this first vibration mode. For clarity, the pillar is shown with its base, though the simulation itself was performed on the pillar alone, applying a clamped boundary condition at its bottom face to represent its attachment to the plate.

Since both components of the final prototype have been independently simulated and validated, the next step involves performing finite element method (FEM) simulations on the complete assembly. These simulations aim to evaluate the global behavior of the final prototype, specifically analyzing the effects of different periodicity conditions and pillar arrangements on the vibration confinement performance.

2.4.2 Prototype Simulations

The final FEM simulation evaluates pillar spacing (4–12 mm, spanning $\lambda/4$ to λ relative to the 13 mm antinode spacing in y) and row count (1–3 rows) to achieve vibration confinement. While classical metamaterial designs rely on Floquet-Bloch theory—which assumes infinite periodicity—our finite plate necessitates an empirical approach as an analytic approach lead to untractable mathematical modeling.

In this simulation, pillar rows are positioned on each side of a plate at a distance of 20 mm, corresponding to the width of the active zone. The plate itself has the same length as the active zone, 115.5 mm. Additionally, the boundary conditions of the large plate are set to be free along all its edges, ensuring an accurate representation of its vibrational behavior.

In this simulation, pillar rows are positioned symmetrically on each side of the plate at a distance of 20 mm, which corresponds to the width of the active zone. The plate itself has the same length as the active zone, 115.5 mm. Furthermore, the boundary conditions of the larger plate are set to be free along all its edges to ensure an accurate representation of its vibrational behavior.

Initially, simulations were performed with a single row of pillars placed on each side of the active zone. The plate was dimensioned just sufficiently to accommodate this configuration, serving as a preliminary test of vibration confinement. In a second phase, the plate size was progressively increased to evaluate the confinement performance in a more realistic application context—specifically, the ability to restrict vibrations within a localized region of a larger surface. This approach enables a systematic assessment of the designed structure's effectiveness in limiting vibrational propagation beyond the targeted confinement area.

2.4.2.1 Simulation with one row

Considering a single row of pillars, modal analysis using finite element method (FEM) simulations was conducted to assess the influence of periodicity on vibration confinement. The periodicity parameter, p, was systematically varied from 4 mm to 12 mm to thoroughly examine its impact on the propagation and attenuation of vibrational modes.

The modal analysis confirmed the existence of the desired vibration mode across multiple periodicity scenarios, where we can clearly notice the desired vibration mode being confined . However, this mode appeared consistently at a lower frequency than initially expected, with the deviation varying according to periodicity. The reasons behind this discrepancy will be further investigated in a subsequent section.

Figure 2.6 illustrates the desired vibration mode for a periodicity of 4 mm. It clearly shows the mode being effectively confined between the pillar rows. However this vibration mode was found at 32 kHz. At the resonance frequency, pillar displacement is primarily observed along the x and y directions. This observation supports our hypothesis regarding mode coupling between the active zone and the pillars, highlighting the effectiveness of the designed structure in achieving vibration confinement.

For next simulation test, we opted of a periodicity of 4 mm. Since our

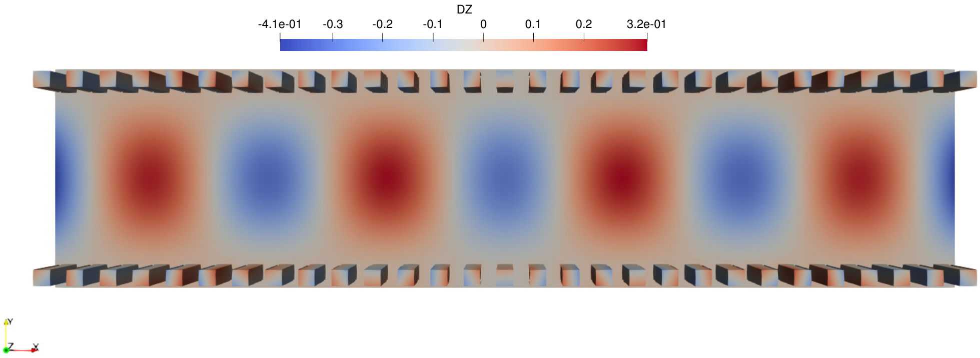

(a) displacement in z direction

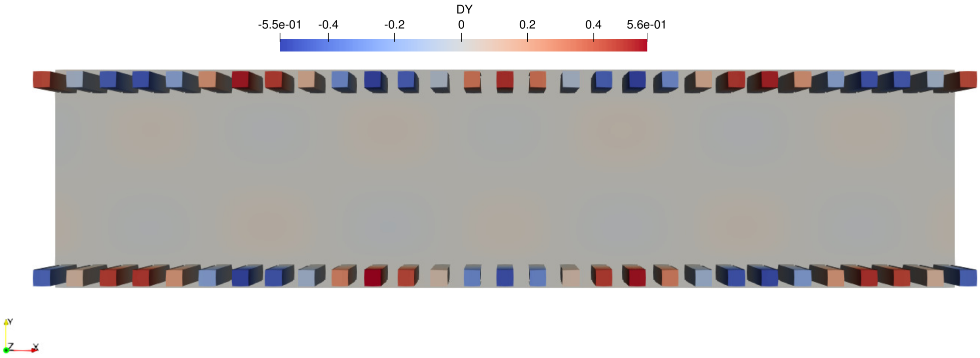

(b) displacement in x direction

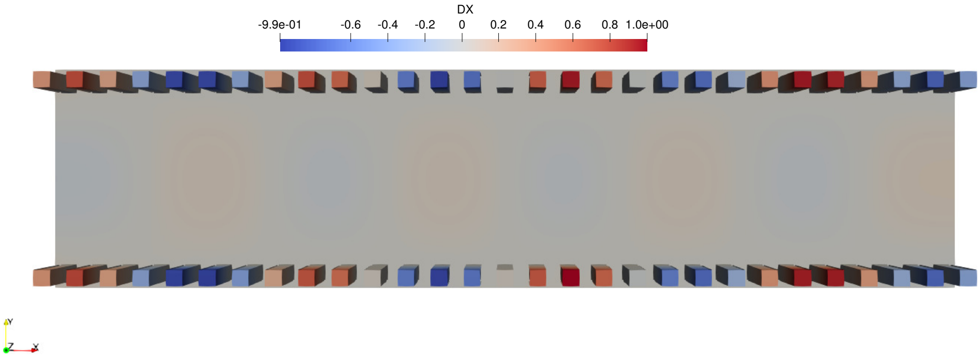

(c) displacement in y direction

Figure 2.6: FEM simulation result with periodicity of 4 mm

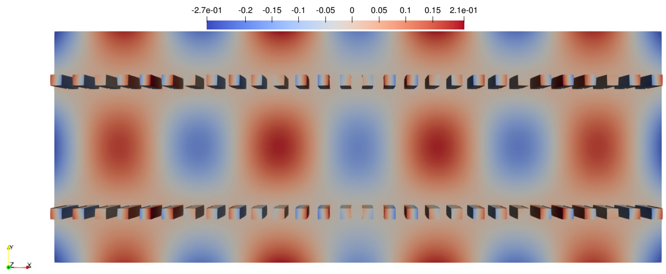

Figure 2.7: One row large surface

primary objective is to confine vibrations within a larger plate structure, the plate size was increased by adding additional surface area on each side of the active zone, specifically by a width of 8 mm on each side. Subsequent FEM simulations revealed that a single row of pillars was insufficient to effectively confine the targeted vibration mode. As illustrated in Figure 2.7, the mode shape clearly shows vibrations propagating beyond the intended confinement region, indicating the inadequacy of a single row of pillars in providing effective vibration isolation. These results highlight the potential necessity of incorporating multiple rows of pillars to achieve better confinement of vibrations, particularly when dealing with larger passive areas.

.

2.4.3 simulation with multiple rows

To systematically assess the limits of vibration confinement, the plate's lateral dimensions were incrementally extended beyond the active zone—from an additional 5 mm (Figure 2.8) up to 25 mm (Figure 2.9). For the 5 mm extension, the existing two pillar rows (one per side) effectively confined vibrations within the designated region. However, at 25 mm, confinement deteriorated significantly, with the vibrational energy leaking beyond the pillar boundaries.

To validate the hypothesis that increasing the number of pillar rows enhances confinement, a third row was added on each side, and the 25 mm configuration was re-simulated (Figure 2.10).

The updated results demonstrated restored confinement, with vibrations tightly localized within the pillar-defined zone. These findings confirm that as the passive zone dimensions scale up, a proportional increase in pillar rows is required to preserve vibration isolation and energy trapping performance.

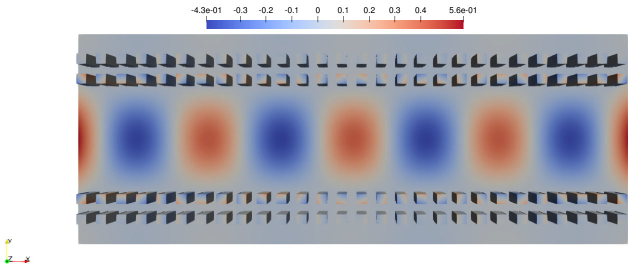

Figure 2.8: Two rows small passive surface

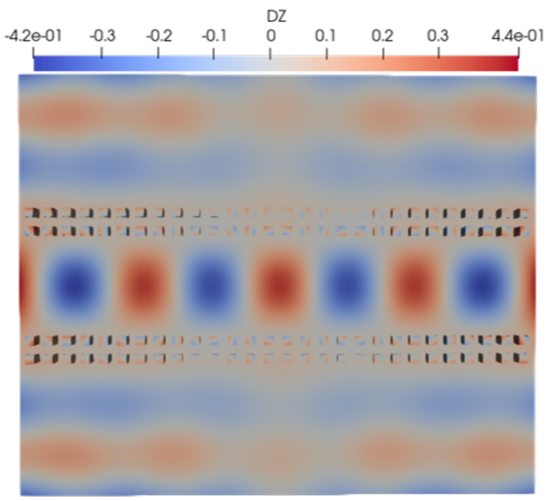

Figure 2.9: two rows large passive surface

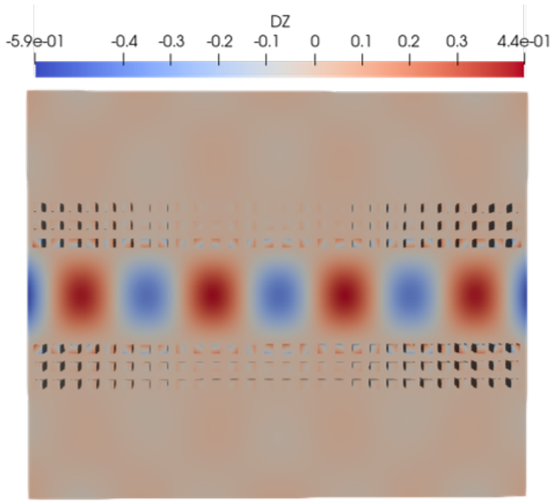

Figure 2.10: Three rows large passive surface

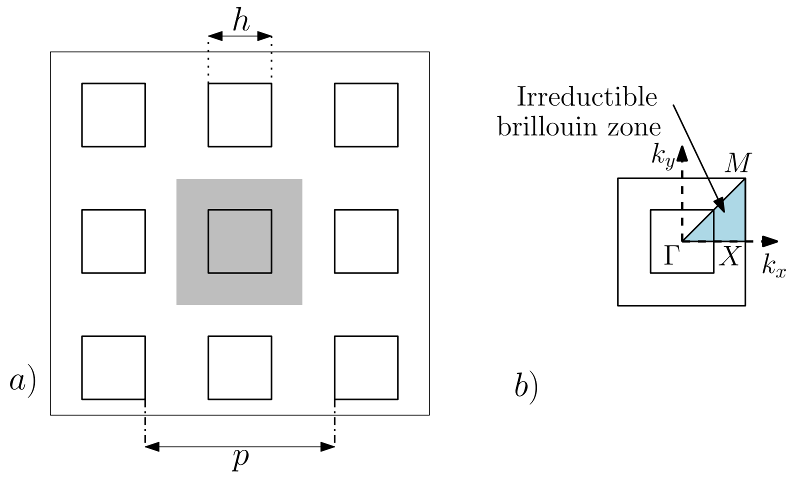

Figure 2.11: The periodic structure. a) 3 × 3 example. b) Brillouin zone

2.5 Investigation of the periodicity effect

The periodicity of pillars critically influences both resonance frequency and wave propagation characteristics. To quantify this relationship, we analyze the dispersion diagram—a fundamental tool in periodic media (e.g., metamaterials)—which plots frequency versus wavenumber. Derived from Bloch-Floquet theory, these diagrams reveal forbidden frequency bands (bandgaps) where vibrations cannot propagate, enabling predictive design of confinement efficacy for arbitrary pillar arrangements.

2.5.1 Evaluating the dispersion diagram

To compute the dispersion diagram, we examine the behavior of a single unit cell of the pillar structure, corresponding to the gray zone depicted in Figure 2.11.a also called *Brillouin zone*. The unit cell is modeled under the assumption of perfect periodicity with a periodicity length p, and an infinite repetition of this pattern is considered. This periodic analysis allows us to identify the relationship between frequency and wave vector, thereby revealing the band structure of the system.

The system behavior , assuming the material is linear elastic and homogeneous with isotropic properties, is governed by the the local dynamic equilibrium [78]:

$$\rho \frac{\partial^2 w}{\partial t^2} = \nabla \cdot \left[C \left(\nabla w + (\nabla w)^{\mathrm{T}} \right) \right], \tag{2.26}$$

where ρ is the mass density, w is the displacement field, and C is the stiffness tensor describing the material's elastic properties.

The frequency response of periodic systems can be efficiently analyzed by studying a single unit cell with Bloch-periodic boundary conditions, which enforce phase continuity across adjacent cells for a given wave vector k. Crucially, symmetry allows restricting the analysis to the irreducible Brillouin zone (IBZ) (Figure 2.11) – a minimal subset of the full Brillouin zone that captures all unique dispersion behavior.

For rectangular lattices, the IBZ is defined by high-symmetry points:

- Γ : Zone center ($k_x = k_y = 0$)
- X : Edge midpoint along kx ($k_y = 0$)
- M : Corner ($k_x = k_y = \pi/p$)

The standard $\Gamma \to X \to M \to \Gamma$ path (Fig. 1.9b) maps the complete dispersion diagram, revealing bandgaps – frequency ranges where wave propagation is prohibited due to destructive interference in the periodic lattice.

The Floquet-Bloch's theorem states that the displacement field w is of the wave equation is governed by the following equation [78] :

$$w(\vec{r} + \vec{a}_i) = w(\vec{r})\, e^{j\vec{k}\cdot\vec{a}_i}, \tag{2.27}$$

where:

- $\vec{r}$ is the position vector within the unit cell.
- $\vec{a}_i$ are the lattice vectors defining the periodicity in the x and y directions.
- $\vec{k} = (k_x, k_y, 0)$ is the Bloch-Floquet wave-vector in reciprocal space.
- j is the imaginary unit ($j = \sqrt{-1}$).

The dispersion diagram is obtained by solving the eigenvalue problem associated with the unit cell, while sweeping the wave vector along the boundary of the irreducible Brillouin zone (IBZ), specifically following the path ΓX, XM, and MΓ. This approach allows the characterization of wave propagation within the periodic structure and the identification of frequency band gaps.

Given the geometric and material complexity of the unit cell, an analytical solution to the eigenvalue problem is generally intractable. Therefore, numerical methods, specifically finite element simulations, are employed to accurately compute the dispersion relations. These simulations provide the eigenfrequencies for each wave vector along the IBZ path, forming the dispersion diagram of the periodic structure.

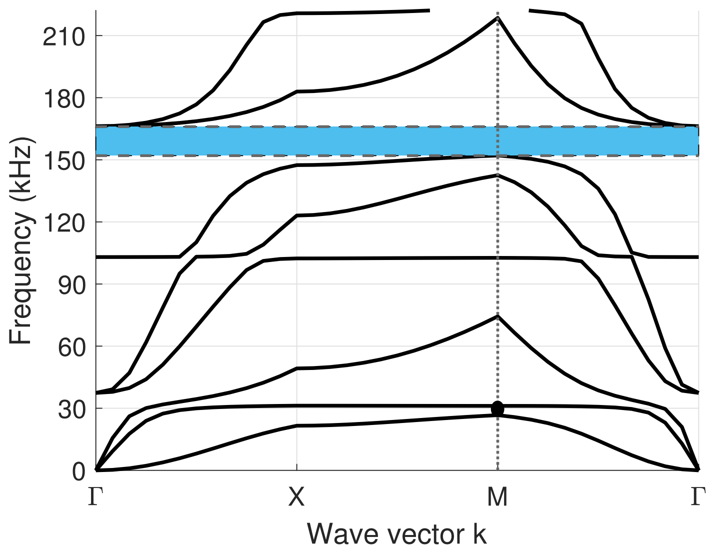

Figure 2.12: Dispersion diagram of the periodic cell. The blue area represents the band gap.

The dispersion diagram of the periodic unit cell is presented in Figure 2.12. It displays several branches, each corresponding to a distinct vibrational mode. Notably, the diagram reveals the presence of a frequency range where no branch appears—highlighted in blue—extending across the entire Brillouin zone. This range is referred to as a *complete band gap*, meaning that any incident wave, regardless of its propagation direction, will be reflected or refracted within this frequency band. In the current case, the complete band gap lies between 152 kHz and 166 kHz.

In this diagram, the resonance frequencies associated with the natural vibration modes (standing wave) of the unit cell can be identified at specific points in the Brillouin zone. These typically occur when the wave vector reaches the high-symmetry point M. For instance, due to geometric symmetry, the first two bending modes are marked in the diagram by black dots. These bending modes correspond to a resonance frequency of 32 kHz.

Based on the dispersion diagram, we observe that the first vibration mode of the unit cell aligns closely with the frequency of the desired vibration mode. This observation can be explained by the principle of mode conversion, which underlies our prototype's design. Specifically, the transverse vibration mode of the active zone couples effectively with the bending vibration mode of the pillars at their interface. Consequently, energy from the active zone vibration mode is efficiently transferred into the pillar vibration mode, resulting in ef-

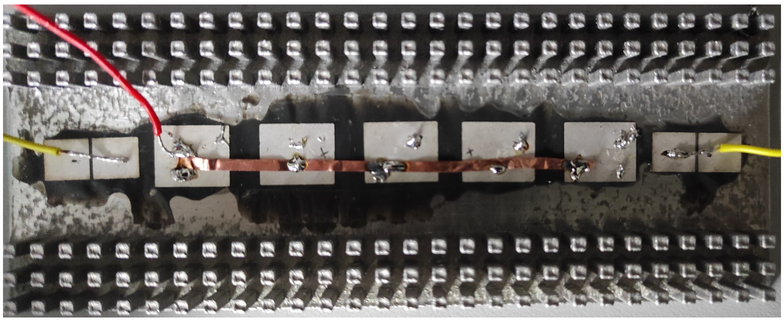

Figure 2.13: the plate simulation with mode confinement. The black squares indicate the locations of the actuators, while the red squares mark the positions of the sensors.

fective confinement of vibrations within the designated region

Our dispersion analysis reveals a paradigm shift from conventional phononic crystals-based prototypes. Phononic crystals rely primarily on frequency band gaps, within which elastic wave propagation is completely prohibited. Consequently, any incident wave at a frequency within this band gap is either reflected or significantly attenuated, resulting in vibration isolation and the potential for localized energy confinement. In such structures, the wavelength associated with the confined vibrations directly depends on the periodicity of the crystal lattice.

In contrast, our prototype leverages mode conversion, actively transferring energy from the transverse vibration mode of the active zone into the pillar bending modes. This mechanism does not solely rely on the existence of a frequency band gap but rather utilizes the resonance matching between the pillar and the active zone to achieve effective confinement.

2.6 Experimental validation

Based on the outcomes of multiple FEM studies, an experimental prototype was developed. It comprises three rows of pillars with a periodicity of 4 mm, without any additional passive surface. Prior to fabrication via 3D printing (Figure 2.13), a dedicated FEM model was constructed using the manufacturer's material data for *Al-Alloy AlSi7Mg0,6*. Piezoelectric actuators with dimensions $12\,\text{mm} \times 3\,\text{mm} \times 0.3\,\text{mm}$ were incorporated into the model and positioned at the antinodes of the targeted vibration mode. The corresponding simulation results are presented in Figure 2.14.

To validate vibration confinement, the surface velocity field of the prototype will be measured using a Laser Doppler Vibrometer (LDV). Since confinement can only be assessed at resonance, the actuation frequency must match that

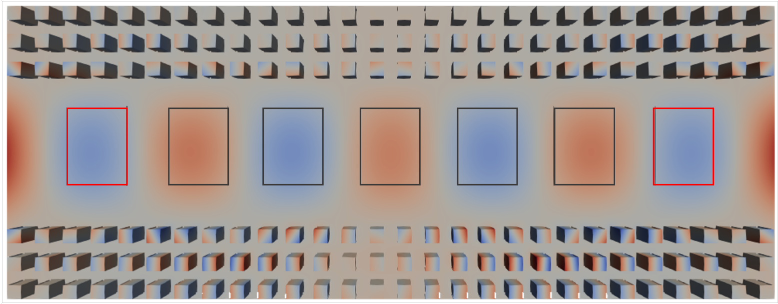

Figure 2.14: Experimental Prototype with piezoelectric ceramics.

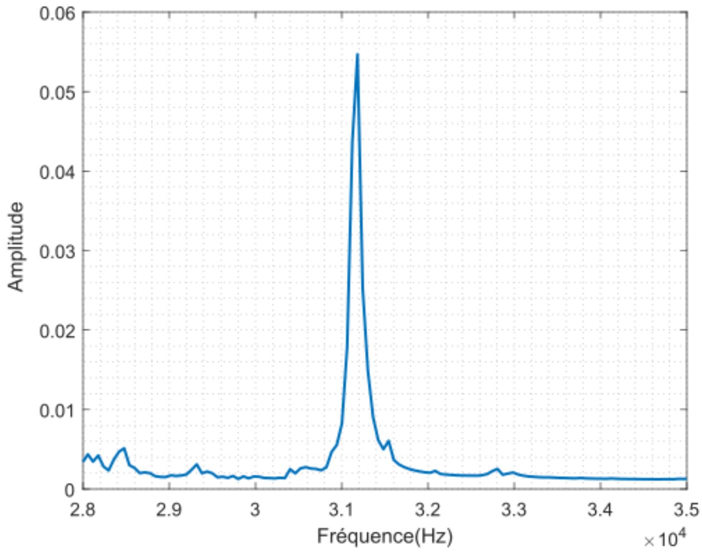

Figure 2.15: Frequency response of the prototype

of the selected vibration mode. To identify this frequency, a sweep was performed using a sinusoidal signal modulated linearly from 28 kHz to 35 kHz. The excitation was applied using a dynamic signal analyzer (SR785, Stanford Research). Figure 2.15 shows the response of a piezoelectric sensor during this test.

The spectrum displays a peak around 31 kHz, confirming the presence of a mode at this frequency. LDV measurements at this frequency confirm that the desired vibration mode is effectively confined, as evidenced by the measured normal velocity field shown in Fig. 2.16.

Since the vibration mode is now effectively confined, the next step involves implementing a closed-loop control system to actively increase its responsiveness, thus expanding the generated stimulus's bandwidth. By broadening the

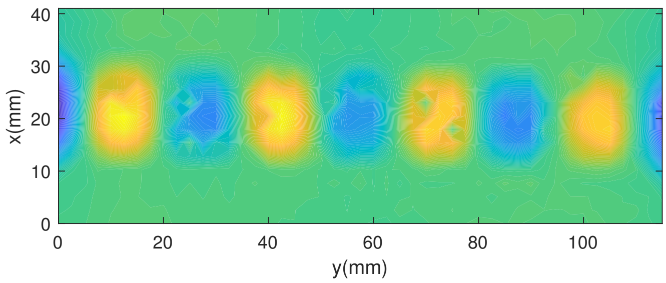

Figure 2.16: Mapping of the confined vibration mode

bandwidth, we enhance the system's ability to generate vibration patterns containing richer frequency content. This improvement allows the creation of more versatile and realistic tactile sensations, which are essential for advanced haptic applications.

Besides our objective to broaden the spectrum of achievable vibration patterns, we also aim to actively control the confined vibration mode. This will enable us to assess whether the adjacent placement of resonating pillars has any significant impact on the effectiveness and precision of vibration mode control. Such analysis is critical to ensure the robustness of the control strategy when pillars are placed closely together within the structure.

2.7 Modeling and control of vibration modes

2.7.1 Dynamic model of a vibration mode

Application of a voltage v across a piezoelectric transducer induces internal stresses via the inverse piezoelectric effect. These stresses lead to mechanical deformations of the material, resulting in the generation of an elastic wave that propagates through the structure.

By applying modal decomposition, the dynamic of a single vibrating mode can be described by a spring-mass-damper model [79]. this behavior can be represented by the following ordinary differential equation :

$$\ddot{w}_n + 2\xi_n\omega_n\dot{w}_n + \omega_n^2 w = g_n v \tag{2.28}$$

where w, ξ, ω_n, g, and v represent, respectively, the modal displacement measured by the sensor, the modal damping factor, the resonance frequency of the mode, the piezoelectric conversion gain, and the supply voltage.

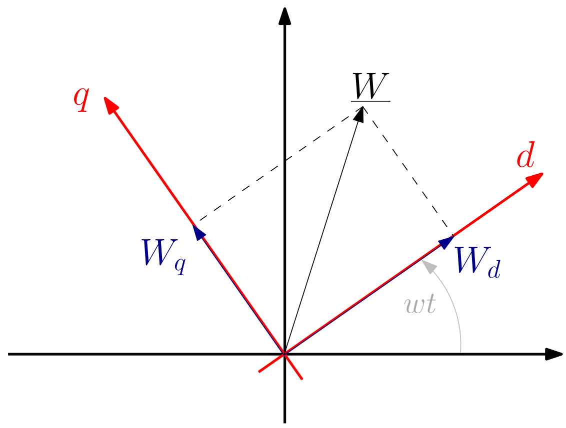

Figure 2.17: Phasor representation of the vibration amplitude W in the rotating reference frame at time t, illustrating its magnitude and phase.)

We rewrite this equation as follows introducing different parameters (from now on, we omit the n index unless needed to avoid ambiguity) :

$$M\ddot{w} + D\dot{w} + Kw = Nv \tag{2.29}$$

with the displacement, M the modal mass, K the modal stiffness, D the modal damping and N the converting factor.

This model describes the instantaneous evolution of the vibration. However, since the actuator is driven by a sinusoidal excitation and the system is assumed to be linear, it is more relevant to characterize the vibration using its phasor representation. For this purpose, the model is reformulated in a rotating reference frame, equivalent to a modulation-demodulation approach.

2.7.1.1 rotating frame modeling

Assuming the vibration is harmonic in time, it can be expressed using a complex notation as:

$$w(t) = \Re\left\{\underline{W}e^{j\omega t}\right\} \tag{2.30}$$

where $\underline{W}$ is the complex amplitude, encoding both the magnitude and phase of the vibration relative to a reference to be defined later. ω is the angular frequency, and $\Re\{\cdot\}$ denotes the real part.

The voltage v can be represented similarly using complex notation. We define $\underline{V}$ as the complex amplitude of the voltage. Figure2.17 illustrates the position of the complex variable $\underline{W}$ at a given time t.

The vectors attached to the complex amplitudes rotate during operation. It is therefore simpler to project them onto a rotating reference frame to get a steady-state fixed vector. So we obtain:

$$\underline{w} = \left(W_\text{d} + jW_\text{q}\right) e^{j\omega t} \tag{2.31}$$
$$\underline{V} = \left(V_\text{d} + jV_\text{q}\right) e^{j\omega t} \tag{2.32}$$

we define a rotating reference frame (d, q), such as the d-axis is aligned with $e^{j\omega t}$. It is more convenient to analyze the dynamics of the vibrational velocity amplitude rather than the displacement amplitude, therefore we define the speed $u(t) = \dot{w}$ and its complex representation :

$$\underline{u} = \left(U_\text{d} + jU_\text{q}\right) e^{j\omega t} \tag{2.33}$$

Furthermore, given the device's normally high quality factor, various simplifying assumptions might be made :

- The frequency is slowly varying, so the derivatives of ω are negligible : $\frac{d\omega}{dt} \approx 0$.
- The dynamic of the vibration amplitude is slow compared with the derivative of the vibration: $\frac{\ddot{W}_d}{\omega^2} \ll W_d$.

By substituting equations (2.31), (2.32) and (2.33) into (2.29), and applying the assumptions, the system reduces to:

$$\left(M + \frac{K}{\omega^2}\right) \dot{U}_\text{d} + DU_\text{d} + \left(\frac{K}{\omega} - M\omega\right) U_\text{q} = NV_\text{d} \tag{2.34}$$

$$\left(M + \frac{K}{\omega^2}\right) \dot{U}_\text{q} + DU_\text{q} - \left(\frac{K}{\omega} - M\omega\right) U_\text{d} = NV_\text{q} \tag{2.35}$$

These equations describe the vibration dynamics in the rotating reference frame. The terms $\pm \left(\frac{K}{\omega} - M\omega\right) U_{d/q}$ represent gyroscopic coupling between the direct (d) and quadrature (q) components. These gyroscopic terms account for Coriolis-like effects arising from the frame rotation, which introduce coupling forces proportional to the angular velocity ω and the rate of change of the orthogonal component. This coupling plays a key role in the dynamics of the system, especially out of resonance.

Assuming a high quality factor for the piezoelectric transducer, the excitation frequencyω is close to the resonance frequency ω_0. We thus define a small detuning $\delta\omega$ such that the first order approximations : $M + K\omega^2 \approx 2M$ and $\frac{K}{\omega} - M\omega = 2M\delta\omega$. Equations (2.34) and (2.35) then become :

$$2M\dot{U}_\text{d} + DU_\text{d} - 2M\delta\omega U_\text{q} = NV_\text{d} \tag{2.36}$$

$$2M\dot{U}_{\mathrm{q}} + DU_{\mathrm{q}} + 2M\delta\omega U_{\mathrm{d}} = NV_{\mathrm{q}} \tag{2.37}$$

The resulting model in the rotating frame reveals that the voltage component along each axis directly controls the vibration velocity on that same axis. Additionally, it highlights a coupling between the two axes analogous to that observed in electrical machines. Furthermore, the vibration dynamics along the dd-axis are shown to be symmetric to those along the qq-axis.

2.7.2 Vibrations Control

Considering the terms $2M\delta\omega U_d$ and $-2M\delta\omega U_q$ as disturbances, they vanish at the resonance frequency ω_0. Otherwise, these disturbances must be compensated by the control system. Given the similar dynamics along both axes, we focus on the control design for a single axis. Applying the Laplace transform, equation (2.36) becomes:

$$\frac{U_{\mathrm{d}}}{V_{\mathrm{d}}} = F(s) = \frac{G}{\tau s + 1} \tag{2.38}$$

With $G = \frac{N}{D}$ and $\tau = 2\frac{M}{D}$.

Controller design Taking into account the first order system in Eq.(2.38), we chose a PI controller, such as :

$$C(s) = K_{\mathrm{p}} + \frac{K_{\mathrm{i}}}{s} \tag{2.39}$$

The control scheme is presented in 2.18. We chose the controller parameters in order to compensate the pole that (2.38) presented , and to ensure a desired closed loop time response defined as $t_{\mathrm{d}} = 3\tau_{\mathrm{d}}$; we have then :

$$K_{\mathrm{i}} = \frac{1}{\tau_{\mathrm{d}} \times G} \qquad K_{\mathrm{p}} = \tau_{\mathrm{d}} \times K_{\mathrm{i}} \tag{2.40}$$

In order to use the controller defined, the identification of the parameters is presented.

2.7.2.1 Modal parameters identification

In order to identify the system τ and G, we consider the steady state. In this condition, the derivatives of U_{d} and U_{q} are null. Assuming that $V_{\mathrm{d}} = V$ and $V_{\mathrm{q}} = 0$ and using equations (2.36) and (2.37), it can be shown that [80]:

$$U_{\mathrm{q}} + \left(U_{\mathrm{d}} - \frac{NV}{2D}\right)^2 = \left(\frac{NV}{2D}\right)^2 \tag{2.41}$$

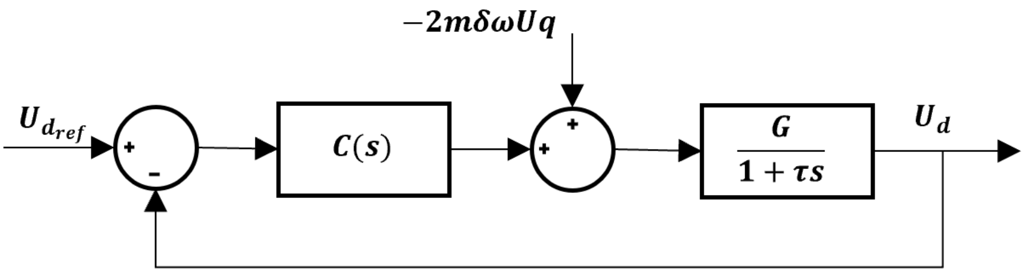

Figure 2.18: Close loop of the vibrations component on the d-axis

Hence, when sweeping the frequency upward through the expected resonance, the vector UU describes a circle centered at $\left(\frac{NV}{2D}, 0\right)$ with radius proportional to $\frac{NV}{2D}$

The value of V is known, however this method don't allow for the separate identification of the values of N or D. however since our purpose is to identify the dynamic parameters τ and G. for that there is relationship between the circle parameters and these dynamic parameters.

For the identification one parameters is used and that's the radius $R = \frac{NV}{2D}$. we can establish based on the circle diameter and the gain are related as such ;

$$\frac{2R}{V} = \frac{N}{D} = G \tag{2.42}$$

Moreover we can establish that the bandwidth of the system ω_{BP} is related to the radius as follows :

$$\omega_{BP} = 2R \tag{2.43}$$

From this we can deduce the time constant τ :

$$\tau = \frac{2M}{D} = \frac{2}{\omega_{BP}} = \frac{1}{R} \tag{2.44}$$

2.8 Electronics Hardware

The control of the haptic device is achieved thanks to an *Stm32f446* Digital Signal Processor (DSP).It is used to synthesize and measure ultrasonic sinusoidal signals via its analog-to-digital converter (ADC) inputs and generates an output voltage through its digital-to-analog converter (DAC). The generated voltage is then amplified by a linear amplifier (NF Corporation HSA4052). The control implemented in this device is similar to the one described in [81]

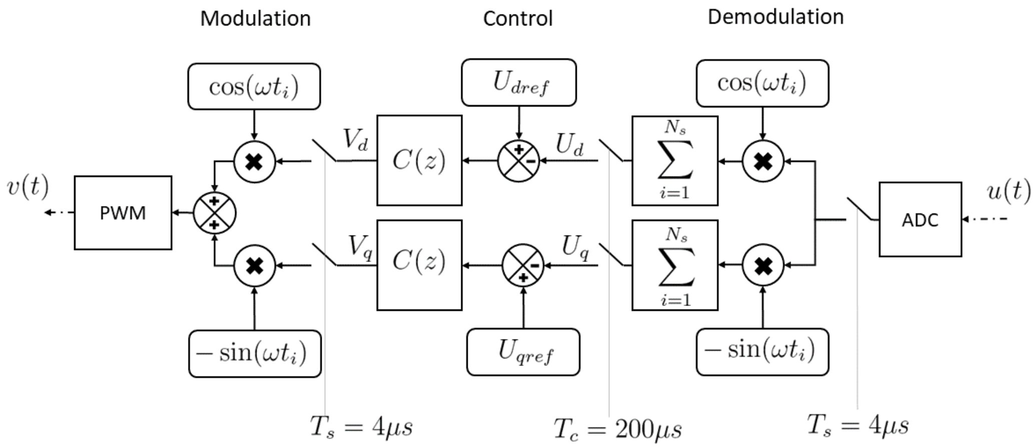

Figure 2.19: Closed loop control scheme in rotating frame

which involves two asynchronous process. A fast process, Direct Digital Synthesis (DDS), at a frequency of 250 kHz ($T_s = 4\,\mu m$), generates the voltage reference that is then amplified to supply the actuators. the voltage is generated considering only the real part of the voltage described in (2.32):

$$v(t_k) = V_d \cos(\omega t_k) - V_q \sin(\omega t_k) \tag{2.45}$$

where $t_k = kT_s$ and k is the sample number.
The DSP also calculates the d-q component of the vibrations as follows :

$$U_d = \frac{1}{N_s} \sum_{i=0}^{N_s-1} w(t_i) \cos(\omega t_i) \tag{2.46}$$

$$U_q = \frac{1}{N_s} \sum_{i=0}^{N_s-1} w(t_i) \sin(\omega t_i) \tag{2.47}$$

.

where N_s is the number of samples per period of oscillation.

The slower process, operating at 5 kHz, generates the voltage reference for the amplifier. The closed-loop control scheme coordinating both processes is shown in Figure 2.19.

2.8.1 Experimental validation

Experimental validation of the control is conducted in two stages: first, mode identification to confirm the targeted vibration mode, followed by the implementation and testing of the closed-loop control.

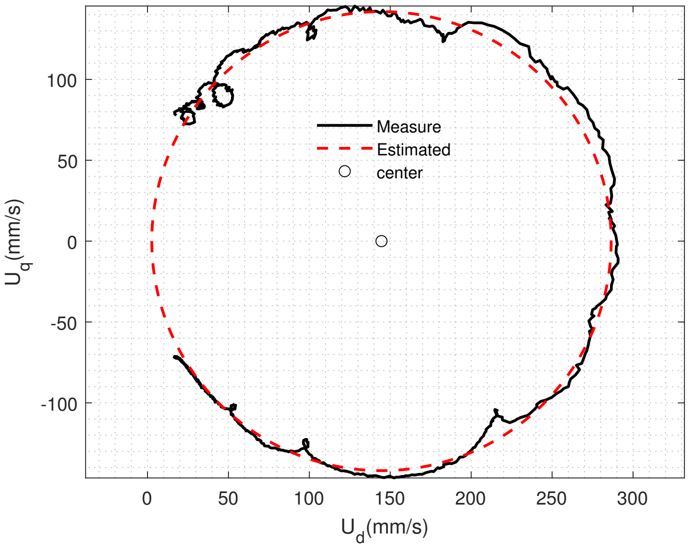

Figure 2.20: Frequency sweep result. In red: experimental measurement; in blue: identified model.

2.8.2 Modal Parameter Identification

To accurately identify the dynamic parameters related to velocity, a frequency sweep was performed to characterize the frequency response of the confined vibration mode. Analysis of the response indicates that the adjacent resonating pillars exert minimal influence on the mode's dynamic behavior, suggesting that their presence does not significantly alter the inherent vibration characteristics.

Using equation (2.41), the dynamic parameters were then identified. The estimated parameters are given in table **??**.

Figure 2.20 compares the measured frequency response with the model prediction based on these parameters, showing good agreement. However, the experimental curve exhibits fluctuations in gain and phase, likely due to dimensional variations among the pillars stemming from manufacturing tolerances.

With the mode parameters identified, the control design and its experimental validation can proceed.

2.8.3 Control Validation

Based on the parameters, the controller was synthesized. PI (Proportional-Integral) regulator was chosen to achieve a response time at 95% of 2 ms ,

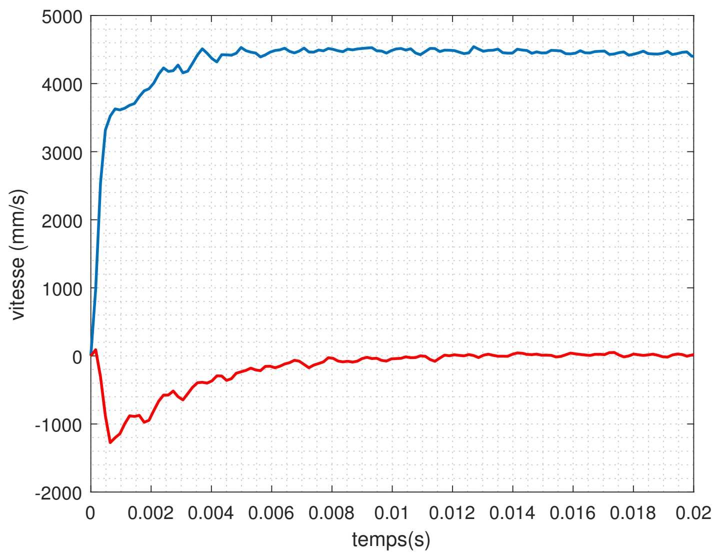

Figure 2.21: System step response. In blue: U_d; in red: U_q.

which is fast enough to ensure high fidelity for textures that can be generated by the prototype.

Figure 2.21 shows the step response for a non-zero direct reference and a zero quadrature reference ($U_\mathrm{d} = 4500$, $U_\mathrm{q} = 0$). The velocities follow their references without overshoot or steady-state error. Based on this , we can validate that despite the dispersion in the pillar dimensions, the PI controller can effectively control the mode vibration with the prescribed dynamic.

2.9 Conclusion

In this chapter, a systematic methodology for designing passively confined vibrations was presented. This method leverages the principle of mode conversion between a primary vibrating surface (plate) and periodically arranged resonating pillars attached to it. Under specific conditions, flexural vibrations occurring on the surface are effectively attenuated by coupling with the bending modes of the pillars, thereby imposing nodes on the plate and limiting vibration propagation. Specifically, the resonance frequency of the desired vibration mode must closely match the first bending resonance frequency of the pillars to ensure efficient energy transfer and confinement.

After successfully demonstrating vibration confinement, a closed-loop control strategy was implemented to evaluate the influence of the resonating pillars on the dynamic control of the vibration mode. The results of this controlled experiment indicated that the presence of the pillars had negligible impact on the effectiveness of vibration control, confirming the robustness and compatibility of the passive confinement strategy with active vibration control methods.

3 Design of actively confined vibrations

3.1 introduction

In this chapter, we explore the concept of active vibration confinement, where a control system is employed to dynamically manage vibrations within specified regions.

Unlike traditional methods that rely on geometric design, active techniques leverage sensors and actuators to monitor and modify the vibration response in real-time. Specifically, piezoelectric actuators and sensors are strategically placed on the vibrating surface to apply targeted forces that counteract or shape the vibrations. The force references required for this process are determined by a control law. In this chapter, we present two complementary strategies for achieving active vibration confinement. The first approach draws inspiration from the passive confinement mechanism described in Section2.2, in which resonant elastic pillars were used to locally attenuate vibration. Here, these pillars are functionally replicated using piezoelectric actuators, enabling dynamic and tunable control over the confinement zone. In the second approach, we expand on the actuator/sensor paradigm by exploiting a distributed network of collocated piezoelectric elements. This configuration enables the real-time shaping of vibrational energy along a beam, allowing not only confinement but also the synthesis of custom vibration patterns. Together, these methods provide a framework for spatially controlling vibrations in flexible structures through active means.

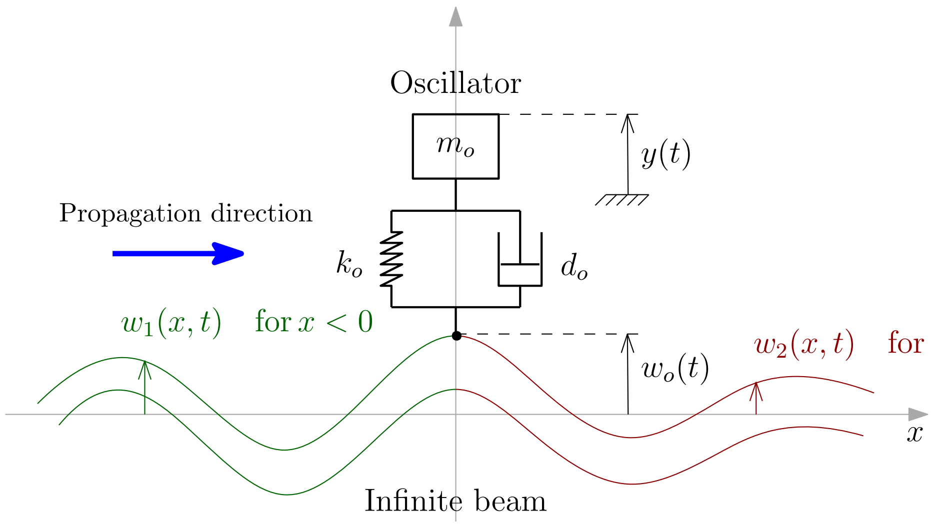

Figure 3.1: Schematic of the traveling-wave confinement problem in an infinite beam using an oscillator.

3.2 Active pillars

3.2.1 General principle

In the passive vibration confinement strategy, the pillars are designed as resonant beams, with their lengths specifically tailored such that their first bending mode resonates at the desired frequency of the confined vibration mode. In this chapter, we synthesize this resonant behavior actively by replacing the passive pillars with actuators. At each actuator location—corresponding to a former pillar position—we measure the local vibration velocity u. Based on this measurement, we compute the force f that the actuator must generate in order to emulate the dynamic response of a resonant pillar at the target frequency. The key advantage of this approach is its adaptability: the active pillar can replicate the desired resonant behavior across a wide range of frequencies and positions. This is achieved by dynamically modifying the relation between the actuator's applied force and the measured velocity. Consequently, the active confinement system offers greater flexibility and can accommodate varying excitation conditions without requiring physical redesign or re-tuning of the structure.

3.2.2 Developing Pillar-Inspired Control Laws for Wave Confinement

To highlight the control strategy, we rely on a simplified model of the interaction between a pillar and the structure as depicted in figure 3.1. We consider an infinite beam in which a flexural progressive wave propagates from $x \to -\infty$ to $x \to +\infty$. At $x = 0$, a harmonic oscillator is fixed and moves vertically under the wave's effect. However, rotation imposed by a perfect fixed support is neglected. Indeed, given the pillars' small size, rotational inertia effects are second-order. Due to the discontinuity introduced by the oscillator, the displacement field is decomposed: for $x < 0$ the wave $w_1(x,t)$ consists of the superposition of the incident and reflected waves, for $x \geq 0$ the wave $w_2(x,t)$ results from the remaining transmitted energy. For the calculation, the incident wave is the input and is arbitrarily set to W_p.

We first determine the force exerted by the beam on the oscillator. The displacement of the mass measured in the earth-fixed reference frame is:

$$\underline{y}(t) = \underline{Y}\,\mathrm{e}^{i\omega t}\ . \tag{3.1}$$

Continuity of the displacement field at $x = 0$ imposes:

$$\underline{w_1}(0,t) = \underline{w_2}(0,t) = \underline{w_o}(t). \tag{3.2}$$

The oscillator's equilibrium is given by:

$$m_o\underline{\ddot{y}} + d_o\left(\underline{\dot{y}} - \underline{\dot{w}_o}\right) + k_o\left(\underline{y} - \underline{w_o}\right) = 0 \tag{3.3}$$

where m_o, d_o, k_o are respectively the mass, damping, and stiffness of the oscillator, and where $\underline{w_o}(t) = \underline{w_2}(0,t)$ is set.

The force applied by the beam on the oscillator is given by:

$$\underline{F}_{p\to o} = -(i\omega d_o + k_o)\left(\underline{y} - \underline{w_o}\right)\quad , \tag{3.4}$$

and since from Eq. (3.3), we have:

$$\underline{y} - \underline{w_o} = \frac{m_o\omega^2\underline{w_o}}{k_o - m_o\omega^2 + d_o\omega}\quad , \tag{3.5}$$

we finally establish:

$$\underline{F}_{p\to o}(\omega) = -(i\omega d_o + k_o)\left(\frac{m_o\omega^2}{k_o - m_o\omega^2 + d_o\omega}\right)\underline{w_o}\,. \tag{3.6}$$

Since we wish to restore the oscillator's resonant behavior through control, we consider $\underline{F}_{p\leftarrow o}(\omega_o) = -\underline{F}_{p\rightarrow o}(\omega_o)$, with $\omega_o = \sqrt{\frac{k_o}{m_o}}$ the oscillator's resonance frequency. After substitution into (3.5) and simplifications:

$$\underline{F}_{p\leftarrow o}(\omega_o) = \left(1 - i\frac{1}{2\xi_o}\right) m_o\omega_o^2\underline{w}_o(t)\,, \tag{3.7}$$

and assuming a weakly damped oscillator ($\xi_o \ll 1$), it becomes:

$$\underline{F}_{p\leftarrow o}(\omega_o) \approx -i\frac{1}{2\xi_o} m_o\omega_o^2\underline{w}_o(t)\,. \tag{3.8}$$

This can be rewritten in terms of velocity (denoted $\underline{u}_o = i\omega_o\underline{w}_o(t)$ for consistency with previous sections):

$$\underline{F}_{p\leftarrow o}(\omega_o) \approx -\frac{1}{2\xi_o} m_o\omega_o\underline{u}_o(t)\,. \tag{3.9}$$

Thus, the oscillator at resonance generates a force proportional to velocity and in phase opposition.

Second, we seek a condition for perfect confinement, which in the model corresponds to canceling displacement in the beam's right part, at least sufficiently far from $x = 0$. We solve by superposition. The general equation, considering a point force at $x = 0$, is:

$$\rho\mathcal{A}\frac{d^2w(x,t)}{dt^2} + E\mathcal{I}\frac{\partial^4 w(x,t)}{\partial x^4} = F(t)\delta(x) \tag{3.10}$$

with $\mathcal{A}$ the beam's cross-sectional area and $\mathcal{I}$ its second moment of area on one hand, and E, ρ the material's stiffness and density on the other.

First, the progressive wave for rightward propagation (from negative to positive x) is given by:

$$\underline{w}_p(x,t) = \underline{W}_p\,\mathrm{e}^{i\beta x - i\omega t} \tag{3.11}$$

where β is the wavenumber and ω the angular frequency, satisfying the dispersion relation $\beta^4 = \frac{\rho\mathcal{A}}{E\mathcal{I}}\omega^2$. It should be noted that this wave corresponds to the solution with no force applied so it is implicit that the inertia effect due to the oscillator's mass m_o is neglected. This induces that the frequency of the propagating wave are less or equal to the oscillator resonant frequency.

For the forced solution, the general solution is:

$$\underline{w}(x,t) = \left(C_1\,\mathrm{e}^{i\beta x} + C_2\,\mathrm{e}^{-i\beta x} + C_3\,\mathrm{e}^{\beta x} + C_4\,\mathrm{e}^{\beta x}\right)\mathrm{e}^{i\omega t} \tag{3.12}$$

but different solutions must be sought per domain as indicated earlier.

The problem simplifies by considering that for $x < 0$ only an incident wave (heading toward $x = 0$) matters, and the evanescent wave must vanish as $x \to -\infty$. Moreover, the problem is symmetric, so the solution must be too. Thus, we seek the displacement field due to forcing by $\underline{F}\,\mathrm{e}^{-i\omega t}$ in the form:

$$\underline{w}_f(x,t) = \begin{cases} \underline{w}_{2_f}(x,t) = A\,\mathrm{e}^{i\beta x} + B\,\mathrm{e}^{-\beta x} & \text{for } x \geq 0 \\ \underline{w}_{1_f}(x,t) = C\,\mathrm{e}^{-i\beta x} + D\,\mathrm{e}^{\beta x} & \text{for } x < 0 \end{cases}. \tag{3.13}$$

The displacement field continuity conditions are:

$$\begin{aligned} \underline{w}_{2_f}(0,t) &= \underline{w}_{1_f}(x,t) \\ \left.\frac{\partial \underline{w}_{2_f}(x,t)}{\partial x}\right|_{x=0} &= \left.\frac{\partial \underline{w}_{1_f}(x,t)}{\partial x}\right|_{x=0}, \end{aligned} \tag{3.14}$$

and for equilibrium we require:

$$\begin{aligned} E\mathcal{I}\left.\frac{\partial^2 \underline{w}_{2_f}(x,t)}{\partial x^2}\right|_{x=0} &= E\mathcal{I}\left.\frac{\partial^2 \underline{w}_{1_f}(x,t)}{\partial x^2}\right|_{x=0} \\ E\mathcal{I}\left.\frac{\partial \underline{w}_{2_f}(x,t)}{\partial x}\right|_{x=0} &= \underline{F}(t)\left.\frac{\partial \underline{w}_{1_f}(x,t)}{\partial x}\right|_{x=0}. \end{aligned} \tag{3.15}$$

with $F(t)$ a force applied to the beam at $x = 0$ After solving, the constants are determined:

$$A = C = i\frac{\underline{F}}{4\beta^3 E\mathcal{I}} \quad \text{and} \quad B = D = -\frac{\underline{F}}{4\beta^3 E\mathcal{I}} \tag{3.16}$$

hence:

$$\underline{w}_f(x,t) = \begin{cases} \underline{w}_{2_f}(x,t) = \dfrac{\underline{F}}{4\beta^3 E\mathcal{I}}\left(i\,\mathrm{e}^{i\beta x} - \mathrm{e}^{-\beta x}\right)\mathrm{e}^{-i\omega t} & \text{for } x \geq 0 \\ \underline{w}_{1_f}(x,t) = \dfrac{\underline{F}}{4\beta^3 E\mathcal{I}}\left(i\,\mathrm{e}^{-i\beta x} - \mathrm{e}^{\beta x}\right)\mathrm{e}^{-i\omega t} & \text{for } x \geq 0 \end{cases} \tag{3.17}$$

Finally, the solution with a progressive wave injected from the left is given by $w(x,t) = w_p(x,t) + w_f(x,t)$, hence it writes:

$$\underline{w}(x,t) = \begin{cases} \underline{w}_1(x,t) = \left[\left(\underline{W}_p + i\dfrac{\underline{F}}{4\beta^3 E\mathcal{I}}\right)\mathrm{e}^{i\beta x} - \dfrac{\underline{F}}{4\beta^3 E\mathcal{I}}\,\mathrm{e}^{-\beta x}\right]\mathrm{e}^{-i\omega t} \\ \underline{w}_2(x,t) = \left(\underline{W}_p\,\mathrm{e}^{-i\beta x} + i\dfrac{\underline{F}}{4\beta^3 E\mathcal{I}}i\,\mathrm{e}^{-i\beta x} - \dfrac{\underline{F}}{4\beta^3 E\mathcal{I}}\,\mathrm{e}^{\beta x}\right)\mathrm{e}^{-i\omega t} \end{cases} \tag{3.18}$$

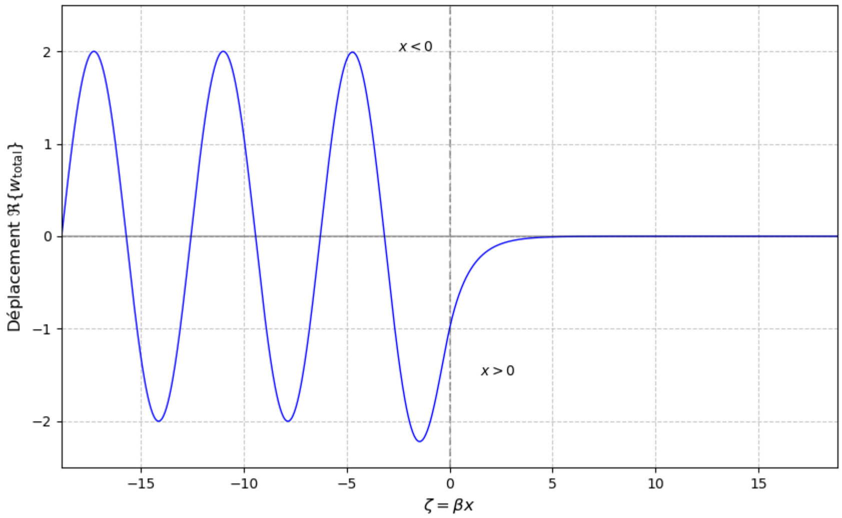

Figure 3.2: Confinement example using Eq. (3.20)'s optimal force for $\underline{W}_p = 1$: the wave is stationary and attenuates on the right. The evanescent wave's presence is clear for $x > 0$

To determine the force value for optimal confinement, we impose zero far-field displacement for $x > 0$:

$$\underline{w}_2(x,t) = 0 \quad \text{for } \beta x \gg 1 \Rightarrow F = -i4E\mathcal{I}\beta^3\underline{W}_p \,. \tag{3.19}$$

This imposes the left far field:

$$\underline{w}_1(x,t) = i2\underline{W}_p \sin(\beta x)\, \mathrm{e}^{-i\omega t} \,, \tag{3.20}$$

which is a standing wave. Thus, there exists a force for which the reflected wave (imposed by the force) exactly compensates the incident wave. However, applying the force necessarily generates displacement beyond $x = 0$ as illustrated in Figure 3.2.

It now remains to equate the arbitrary harmonic force used to establish the forced solution with the force applied by the oscillator to the beam, assuming that the frequency of the incident wave coincides exactly with the resonance frequency of the oscillator. Observing that the amplitude imposed on the oscillator at $x = 0$ is $\underline{w}_o = -\underline{W}_p$, and exploiting relation (3.9), we derive the approximate condition:

$$\frac{m_o\omega_o^2}{2\xi} = 4E\mathcal{I}\beta^3 \Rightarrow \xi = \frac{1}{2}\left(\frac{m_o}{\rho\mathcal{A}}\right)^{\frac{3}{4}}\left(\frac{k_o}{E\mathcal{I}}\right)^{\frac{1}{4}} \,, \tag{3.21}$$

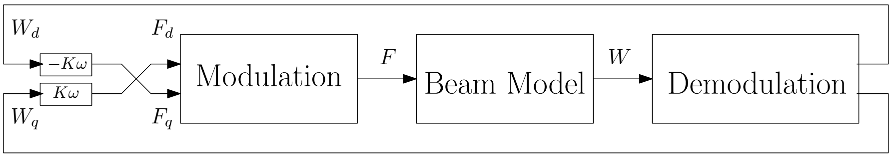

Figure 3.3: Vibration confinement scheme based on the electrical analogy: the block "beam model" simulate the dynamic of a pillar which is implemented in the rotating frame.

where we used the dispersion relation for resonance $\omega_o = \sqrt{\frac{k_o}{m_o}} = \sqrt{\frac{E\mathcal{I}}{\rho\mathcal{A}}}\beta^2$. This demonstrates the difficulty of achieving optimal confinement with a single force, as tuning the structure's resonances requires an additional dissipation condition, while damping is fixed by material choice for pillars.

The theoretical analysis reveals that a control law emulating pillar dynamics requires a precise gain (ξ) for optimal confinement (Eq. 3.21). This stringent condition – dependent on fixed material properties and inertial parameters – poses implementation challenges. Notably, this could explain why numerical simulations demonstrated that multiple pillar rows are necessary: distributed force application provides robustness against sensitivity to the critical ξ value. Motivated by Eq. 3.8, we therefore implement a simplified control law:

$$\underline{F} = K\underline{u}_o \tag{3.22}$$

This approach maintains some physical relevance while being practical.

Reformulated in a rotating reference frame for implementation simplicity, the control law becomes:

$$\begin{aligned} F_d &= KU_\mathrm{d} \\ F_q &= KU_\mathrm{q} \end{aligned} \tag{3.23}$$

with U_d and U_q denoting in-phase and quadrature modal velocity components.

This structure theoretically enables frequency-independent confinement,provided that the control gain is sufficiently high to effectively attenuate the vibration response. We verify this principle through simulations quantifying performance limits and stability robustness.

3.2.3 Simulation of the control law

To evaluate the effectiveness of the proposed active confinement strategy, we consider a free-free beam modeled via Euler-Bernoulli theory. The dynamic response is simulated using a *time-domain* Green's function formulation for harmonic excitation [82], which analytically determines displacement fields induced by concentrated forces at discrete positions. This framework, integrated with our control strategy, enables analysis of controlled dynamics when excitation and confinement points are spatially separated. The simulation is done for free-free boundary conditions, and the locations of the force are chosen relatively close to antinodes of the vibration at 3 kHz. This ensures that the force can act on the vibration for two scenarios detailed later.

It is important to emphasize that this simulation represents an illustrative case study rather than a comprehensive parametric investigation. The primary objective is to demonstrate the feasibility of the approach and highlight its key characteristics, not to exhaustively explore all possible configurations or operational conditions.

We adapt the control law (3.23) to express force-displacement relationships. Under the harmonic oscillator approximation (valid under modal projection), the control forces in the demodulated frame are:

$$\begin{aligned} F_d &= -\omega_1 K W_{\mathrm{q}} = K' W_{\mathrm{q}} \\ F_q &= \omega_1 K W_{\mathrm{d}} = K' W_{\mathrm{d}} \end{aligned} \tag{3.24}$$

Vibration excitation is applied at the beam's centerline, while confinement forces act symmetrically about this point (Figure 3.4). To illustrate the confinement behavior, simulations were conducted for two specific scenarios: first, with 3 kHz excitation and two different control gain values (K), demonstrating the influence of gain magnitude on performance; second, with 5 kHz excitation to examine frequency-dependent effects. In both cases, the excitation amplitude remained fixed at 1 N to ensure consistent comparisons.

These limited scenarios serve to validate basic operational principles and reveal potential implementation challenges. The study does not explore critical parameters like control point spacing or location optimization, and conclusions should be interpreted as indicative rather than comprehensive.

First, we present results for an excitation at 3 kHz, where the system response is analyzed under two distinct control gain values K', allowing us to assess the influence of the gain magnitude on confinement performance. Subsequently, the simulation is repeated for an excitation at 5 kHz, providing insight into the behavior of the system at a higher frequency and enabling comparison across different conditions.

In all simulation scenarios, the excitation force applied to induce vibrations is set to a constant amplitude of 1 N. This ensures consistency across different test cases and allows for a fair comparison of the resulting vibration confinement performance.

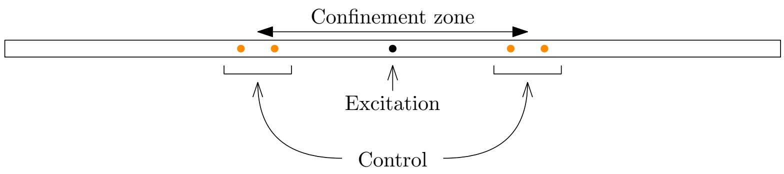

Figure 3.4: Schematic of the simulated beam : the excitation is applied at the center of the beam (black dot), and forces are applied at the orange dot to confine the vibration in the region they delimit.

Simulation results

An initial evaluation of the vibration confinement strategy was conducted at 3 kHz. In this configuration, excitation forces were applied uniformly in the same direction across the designated control (confinement) points, as illustrated in Figure 3.5a. The corresponding results, presented in Figure 3.5b, indicate a successful attenuation of the vibration amplitude beyond the control points—by approximately a factor of three. Furthermore, it is observed that nodal lines precisely emerge at the locations where control forces were applied. This confirms that the strategy effectively imposes spatial constraints on the vibration field.

In subsequent simulations, control forces were configured as opposing force couples at adjacent confinement points to generate pure bending moments. This arrangement realistically models piezoelectric transducer behavior, where antiparallel surface forces create counteracting moments at patch boundaries (Fig. 3.6a). By inducing controlled curvature reversals, this moment-dominated approach more effectively impedes vibrational wave propagation through localized impedance mismatches.

The simulation results, presented in Figure 3.6b, demonstrate a notable improvement in confinement performance when using opposing-direction control forces. Within the target tactile interaction zone, active confinement boosted vibration amplitude from 2 μm (uncontrolled) to 6 μm (controlled)—a threefold increase demonstrating successful energy focusing. This amplification is further evidenced by a sixfold amplitude ratio across the confinement boundary, confirming effective suppression of peripheral energy leakage. The combined effect could enhance haptic signals through energy concentration where users interact, while simultaneously improving system efficiency by minimizing dissipation across non-functional surfaces.

During our tests, various gain values were evaluated to determine the conditions necessary for achieving effective vibration confinement. It was observed that a high gain- on the order of 1×10^8 - was required to produce the desired confinement behavior. The results obtained using this gain are

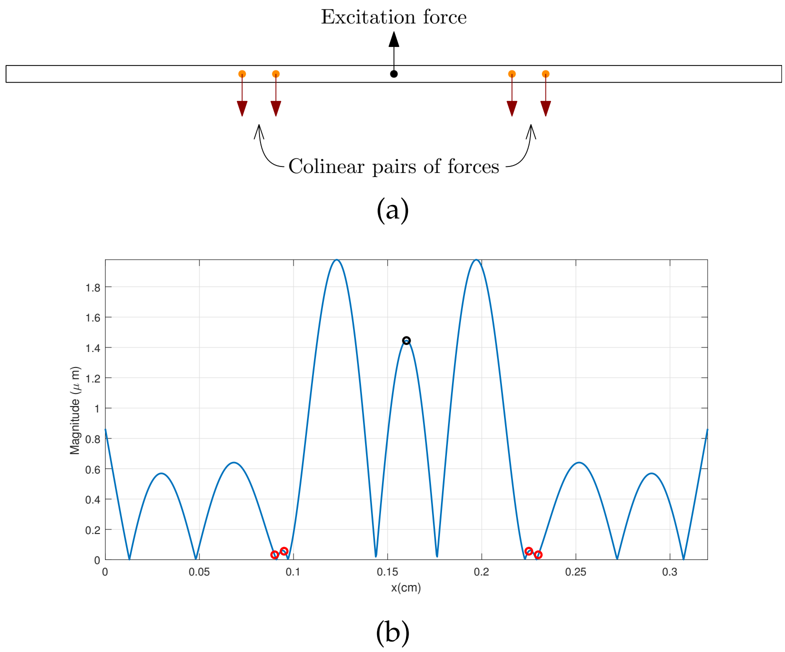

Figure 3.5: Control strategy mimicking the effect of pillars rows: a) Forces distribution used to approximate the effect of pillars; b) Modulus of the vibration velocity at 3 kHz with opposite control forces

shown in Figure 3.7a, where the vibration amplitude is effectively suppressed outside the targeted region.

Conversely, when the gain was reduced to 1×10^7, the confinement performance degraded significantly. As illustrated in Figure 3.7b, vibrations were no longer effectively confined, indicating that the gain magnitude directly influences the control system's ability to attenuate vibration propagation. These observations emphasize the high dependence of vibration confinement effectiveness on the gain value. An additional test conducted at a higher frequency using the same gain value (1×10^8) further reveals that the effectiveness of the confinement strategy also depends on the excitation frequency. This is expected because the actuator locations non longer respect the requirement to apply forces around antinodes. As shown in Figure 3.8, the confinement fails at this frequency, indicating that a the high gain need to be adapted to the wavelength, hence the frequency. in order to guarantee effective confinement across all frequencies.

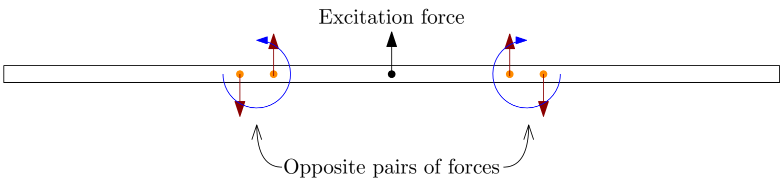

(a)

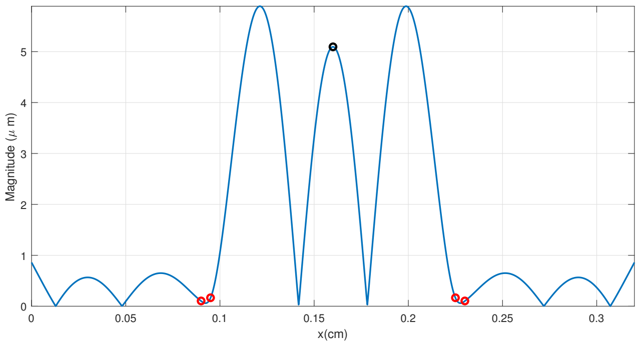

(b)

Figure 3.6: Control strategy mimicking the effect of ceramic patches: a) Forces distribution used to approximate the effect of piezoelectric patches which act as localized moments; b) Modulus of the vibration velocity at 3 kHz with opposite control forces

3.2.4 Challenges to implement this method

During the simulation results multiple challenges have been spotted that restrict the practical application and implementation of this method such as :

- **High gain requirement:** The method demonstrates a strong reliance on high gain values—on the order of 10^8—to achieve effective vibration confinement. While the simulations only display the steady-state response, the transient dynamics where displacements can reach micrometer scales, potentially generating forces exceeding 100 N. Such large gains are highly susceptible to external disturbances and sensor noise, posing significant challenges for practical implementation.
- **Sensitivity to gain variation:** The confinement effectiveness is highly sensitive to the selected gain value. Even minor deviations from the optimal gain lead to a substantial degradation in performance, limiting the robustness of the approach.
- **Frequency dependence:** The method exhibits a marked dependence on the excitation frequency. This implies that the gain must be adapted to the

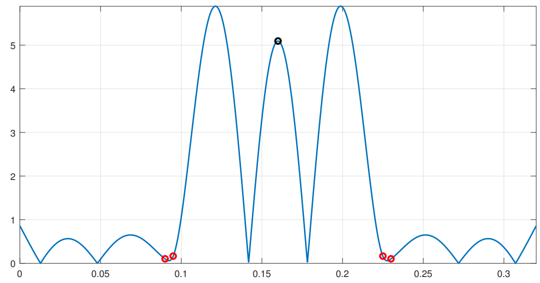

(a) Confinement for a feedback gain $K' = 1 \times 10^8$

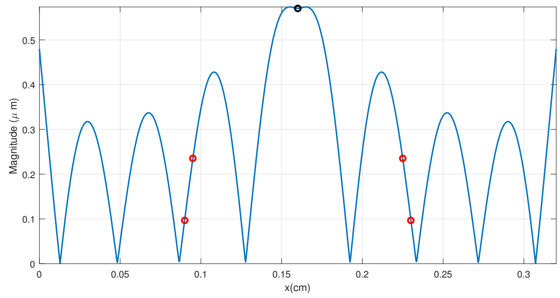

(b) Confinement for a feedback gain $K' = 1 \times 10^7$

Figure 3.7: Comparison of confinement control for different feedback gains at 3 kHz

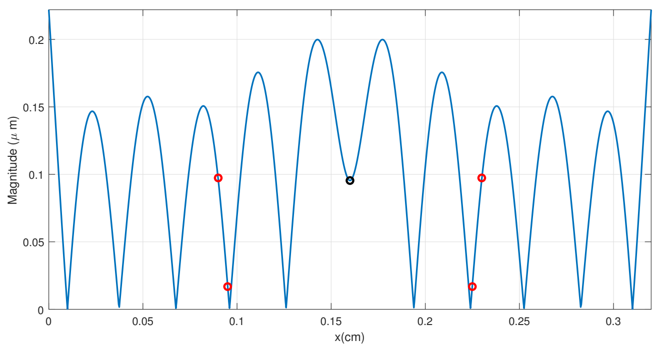

Figure 3.8: Simulation results at 5 kHz

operational frequency range. In practice, this could require even higher gains for certain frequencies, further compounding the implementation challenges mentioned above.

These constraints significantly limit the robustness and scalability of the control strategy, particularly in noisy environments –which is characteristic of our application due to the low vibration amplitudes– or when dealing with broadband or time-varying excitations. In light of these limitations, we decide to explore an alternative control approach capable of delivering reliable and adaptive vibration confinement under realistic operational conditions.

3.3 Confinement by sensor/actuator framework

The initial control strategy exhibited limitations in achieving robust vibration confinement. Converting the proportional control to a proportional-integral (PI) architecture within the rotating reference frame –mathematically equivalent to a proportional-resonant (PR) controller [83]– provides theoretically infinite gain at the modulation frequency. However, this introduces critical stability challenges in non-collocated configurations. The inherent $-\pi/2$ phase lag characteristic of integral controllers combines with structural phase responses near other modes, degrading phase margin. Furthermore, high-frequency feedthrough effects, where unattenuated dynamics bypass the controller's bandwidth [79], create additional destabilizing pathways. Under high-gain conditions, the aggregate phase shift approaches $-\pi$ at critical frequencies, creating instabilities through unintended positive feedback loops. This dual challenge of phase degradation and high-frequency feedthrough presents fundamental implementation barriers for non-collocated confinement systems.

Given these limitations, it is necessary to propose a robust method for active vibration confinement. This method leverages a distributed network between a number of actuators n_a and a number sensors n_c, while explicitly accounting for the dynamic coupling interactions among them. By doing so, it enables real-time control over vibration propagation and facilitates the spatial localization of vibrational energy particularly around the sensors.

Beyond simple confinement, this architecture offers the potential to dynamically generate a variety of spatial vibration patterns without requiring modifications to the control framework. Such adaptability is essential for applications like surface haptics, where the ability to reconfigure feedback profiles on demand enhances both functionality and user experience.

To streamline the development and analysis process, we constrain the propagation of vibrations to a single spatial dimension by modeling the structure as a beam. Piezoelectric ceramics are employed as the actuation and sensing elements, arranged in a collocated configuration where each sensor shares the same physical location as an actuator $n_c = n_a = N$. This setup is particularly advantageous, as it supports accurate measurement and control of local vibration fields, thereby enhancing the precision of the confinement mechanism. This is also motivated by Preumont's fundamental observation that non-collocated configurations inherently exhibit non-minimum phase behavior due to right half-plane zeros [79]. Such zeros migrate into the operational bandwidth precisely when spatial separation exists between actuation and sensing points. By implementing colocated control in our system, we deliberately avoid these complications—ensuring minimum-phase characteristics within our target bandwidth and preserving adequate phase margins for stable operation. The newly proposed control architecture is grounded in the modal superposition principle, which serves as the theoretical foundation for analyzing and controlling the system's dynamic response. Before detailing the control scheme, we begin with a brief introduction to modal superposition. This approach assumes that the response of a linear elastic system can be expressed as a weighted sum of its natural vibration modes. By projecting the system dynamics onto its modal basis, the complex coupled spatial-temporal behavior is transformed into a set of decoupled ordinary differential equations, each representing an independent mode. This simplification facilitate the analysis and design of our control law.

3.3.1 Modal Superposition

In linear elastodynamics, the free vibration problem—governed solely by initial displacement and velocity fields without external loading—admits infinitely many solutions. Each solution corresponds to an eigenpair consisting of a natural frequency ω_m and an associated *mode shape* $\phi_m(\boldsymbol{x})$, where $\boldsymbol{x}$ denotes the spatial coordinate vector and $m \in \mathbb{N}$. These eigenpairs satisfy the homogeneous boundary-value problem, with mode shapes defined up to an arbitrary scaling constant.

Mathematically, these mode shapes form a complete orthogonal basis for the solution space satisfying the kinematic constraints [84]. Consequently, the dynamic response to arbitrary mechanical loading can be expressed through modal superposition:

$$\boldsymbol{w}(\boldsymbol{x}, t) = \sum_{m=1}^{\infty} w_m(t)\phi_m(\boldsymbol{x}), \tag{3.25}$$

where $w_m(t)$ are the time-dependent generalized coordinates representing modal participation factors.

Physically, this decomposition separates the spatial distribution of vibration energy (ϕ_m) from its temporal evolution (w_m), reducing complex distributed systems to assemblies of single-degree-of-freedom oscillators [77]. This framework provides the theoretical foundation for our subsequent analysis of vibration confinement in beam structures. It should be noted, that for a given admissible displacement field, one can calculate the coordinates $\boldsymbol{w}_m(t)$ from the inner product:

$$w_m(t) = \iiint_\Omega \phi_m(t)^T \boldsymbol{w}(\boldsymbol{x}, t) d\Omega, \tag{3.26}$$

where Ω is the domain occupied by the structure. The normalization is arbitrary, and a common choice is to normalize to have unitary modal masses. The mass-normalized modes $\hat{\phi}_j(\boldsymbol{x})$ verify:

$$\iiint_\Omega \rho(\boldsymbol{x}) \hat{\phi}_j(\boldsymbol{x})^T \hat{\phi}_j(\boldsymbol{x}) d\Omega = 1$$

where ρ is the density. Using the projection of the wave propagation equation on the mass-normalized mode shapes reveals that each modal amplitude $\boldsymbol{w}_m(t)$ satisfies the following ordinary differential equation for :

$$\ddot{w}_m(t) + 2\xi_m \omega_m \dot{w}_m(t) + \omega_m^2 w_m(t) = f_m(t)\,. \tag{3.27}$$

This projection eliminates spatial dependencies, yielding independent oscillator equations. Here, ξ_m is the modal damping ratio, ω_m is the natural frequency, and $f_m(t)$ is the modal force.

Note: This normalization is chosen for the purpose of the example. In practice, different normalizations, such as a unitary maximum amplitude, are used and for each mode a modal mass M_j, a modal damping D_j and a modal stiffness K_j appear in the right hand side of the dynamic equation (3.27). □

For this simplified case study, we consider a beam (uni-dimensional domain $\Omega \to [0, L]$) with N actuators at positions x_k. The forces are supposed to be ideally concentrated at the actuator locations and normal to the beam. We can express the relevant component as the distribution of forces normal to the beam:

$$F(x, t) = \sum_{j=1}^{N} F_j(t) \delta(x - x_j) \tag{3.28}$$

where δ is the Dirac distribution. The modal force applied to the mode m is given by the projection on $\hat{\phi}_m$:

$$f_m(t) = \iiint_\Omega \sum_{k=1}^{N} F_j(t) \delta(x - x_j) \hat{\phi}_m(x) d\Omega\,, \tag{3.29}$$

which leads to:

$$f_m(t) = \sum_{j=1}^{N} \hat{\phi}_m(x_j) F_j(t)\,. \tag{3.30}$$

This formulation demonstrates that force coupling to mode m is governed by the mode shape amplitude at actuator locations. Crucially, this spatial dependence means modes with nodal lines at actuator positions ($\hat{\phi}_m(x_j) = 0$) cannot be excited, while higher-order modes experience progressively weaker excitation. With finite actuators, the system exhibits inherent spectral selectivity—only modes with significant $\hat{\phi}_m(x_k)$ magnitude at these specific locations can be effectively controlled. This spatial filtering represents a fundamental constraint in discrete-actuator vibration confinement systems.

For each actuator, the force is generated using the piezoelectric effect, and is therefore proportional to the voltage across the patches which we assumed to be independent, thus:

$$F_j(t) = K_f V_j(t) \tag{3.31}$$

where K_f is a coefficient depending on the piezoelectric material and the geometry of the patches (supposed to be the same for all actuators here).
Applying the Laplace transform to (3.27) while incorporating (3.30) yields the modal participation of the mode m:

$$W_m(s) = \sum_{j=1}^{N} \hat{\phi}_m(x_j) \frac{K_f V_j(s)}{s^2 + 2\xi_m \omega_m s + \omega_m^2}. \tag{3.32}$$

with $W_m(s) = \mathcal{L}[w_m(t)]$ the Laplace transform of $w_m(t)$

Note: This concentrated force model represents a simplified case study for fundamental validation. Practical implementations would account for distributed actuator effects and spatial filtering.

Due to reversibility of the piezoelectric patches and the colocalisation, the displacement measured by the sensor at position x_k ($k \in \{1, \ldots, N\}$) and due to the mode m is expressed as:

$$\underline{W}_{km}(s) = K_f \hat{\phi}_m(x_k) W_m(s) = K_f^2 \hat{\phi}_m(x_k) \sum_{j=1}^{N} \hat{\phi}_m(x_j) \frac{K_f V_j(s)}{s^2 + 2\xi_m \omega_m s + \omega_m^2}\,. \tag{3.33}$$

Despite the notation, $\underline{W}_{km}(s)$ is a voltage, and should be understood as the contribution of the mode m too the measured voltage on sensor k. This reconstruction exhibits some limitations: modes with nodes at x_k ($\phi_k(x_l) = 0$)

remain undetectable, and higher-order modes become progressively unresolvable. Actually, since sensors are colocated with actuators in our configuration, this spatial filtering creates identical constraints for both sensing and actuation—modes unobservable are simultaneously uncontrollable. This limitation defines the fundamental modal subspace accessible to colocated confinement strategies.

Finally, the voltage on sensor k results from the contribution of all excited modes, which we can write using the decomposition property as:

$$\underline{W}_k(s) = \sum_{m=1}^{\infty} \underline{W}_{km}(s) = \sum_{m=1}^{\infty} K_f^2 \hat{\phi}_m(x_k) \sum_{j=1}^{N} \hat{\phi}_m(x_j) \frac{K_f V_j(s)}{s^2 + 2\xi_m \omega_m s + \omega_m^2}\,. \tag{3.34}$$

Now, since the infinite sum is guaranted to converge as a consequence of the decomposition theorem, the expression can be rearranged:

$$\underline{W}_k(s) = \sum_{j=1}^{N} \left[K_f^2 \sum_{m=1}^{\infty} \frac{\hat{\phi}_m(x_k)\hat{\phi}_m(x_j)}{s^2 + 2\xi_m \omega_m s + \omega_m^2} \right] V_j\,. \tag{3.35}$$

3.3.2 Control strategy

The previous theoretical developments are expressed as the scalar product of a row vector, whose components correspond to the transmittance between sensor k and the voltage $V_i(s)$ applied to actuator i:

$$\underline{\boldsymbol{W}}_k(s) = \boldsymbol{T}(s)_j \boldsymbol{V}(s)$$

where the relevant expressions can be directly identified from Eq. (3.35). Concatenating the $\underline{\boldsymbol{W}}_k(s)$ into a column vector, the set of measurements caused by the voltages applied $\boldsymbol{V}(s)$ are in matrix form:

$$\underline{\boldsymbol{W}}(s) = \boldsymbol{T}(s)\boldsymbol{V}(s) \tag{3.36}$$

The objective of the control is to impose a velocity field concentrated in a specific region of the beam, thereby reproducing a confinement effect similar to the passive solution using pillars. This requires individualized actuator control based on the complete set of measurements from the sensing ceramics. It is therefore necessary to determine the relationship between the measured signals and the voltages in order to design the feedback loops. Since the application involves a single-frequency vibration (denoted Ω), Eq. (3.36) can be exploited for this purpose. At a given frequency, the components of matrix $\boldsymbol{T}$

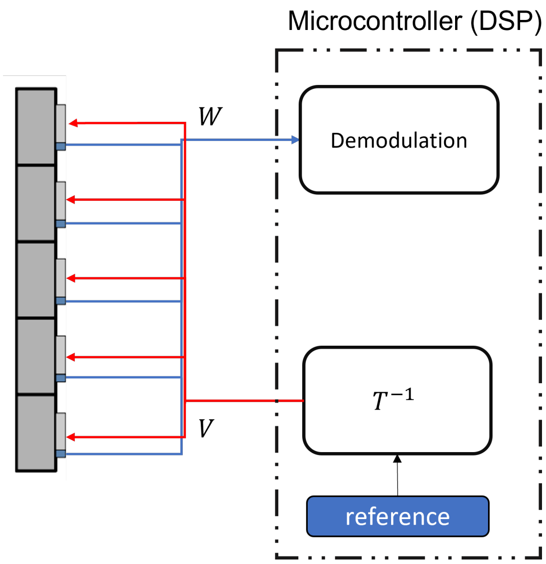

Figure 3.9: Control strategy

are constant complex numbers. The actuator voltages $V_i$can thus be obtained by inverting Eq. (3.36):

$$\boldsymbol{V}(\Omega) = \boldsymbol{T}(\Omega)^{-1}\underline{\boldsymbol{W}}(\Omega) \tag{3.37}$$

This implies that the matrix $\mathbf{T}(\Omega)$ must be invertible. A first condition can therefore be established regarding the frequency Ω. Indeed, it is known that when lightly damped structures are excited at a resonance frequency, the vibration is dominated by the corresponding mode (for example $\hat{\phi}_m$). Thus, in this case we have:

$$\underline{W}_k(s) \approx K_f^2 \hat{\phi}_m(x_k) \sum_{j=1}^{N} \frac{\hat{\phi}_m(x_i)}{\omega_m^2 - \Omega^2 + 2i\xi_m\omega_m\Omega} V_j \quad \text{pour}\, \Omega \approx \omega_m$$

This shows that the rows of the matrix $\mathbf{T}$ differ only by a multiplicative factor, meaning that it is not invertible. Physically, this implies that the energy is mainly injected into the dominant mode, making it impossible to sense and actuate the other modes. It is therefore necessary to operate at a frequency that does not excite a mode resonance.

However, even if this condition is met, poor conditioning may still occur if the transmittance coefficients are too similar.

3.3.3 Simulation-based validation of the method

A simulation was conducted on a beam of length 100 mm, with six actuators evenly distributed along its length. Each actuator was paired with a co-located sensor positioned at the same location, enabling simultaneous actuation and measurement at discrete points along the beam (cf. Figure 3.9). Moreover the beam was in clamped-clamped boundary conditions. The beam configuration resulted in the modal response presented in Figure 3.10.

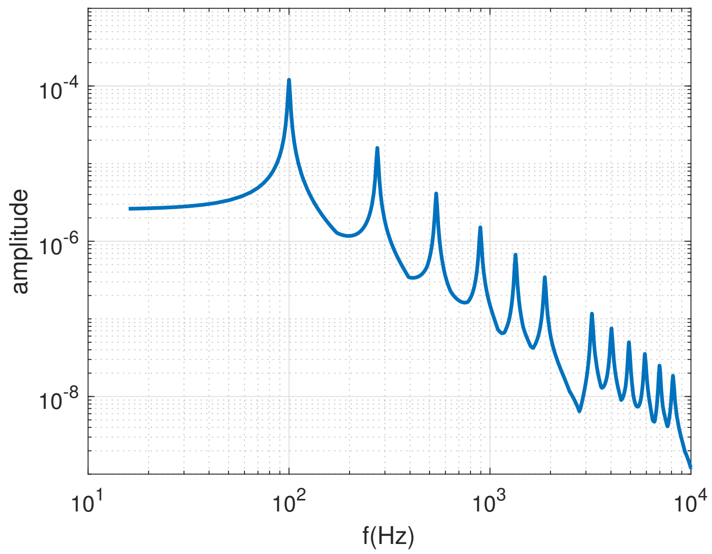

Figure 3.10: Modal response of the simulated beam

The proposed methodology was implemented on the simulated beam model to evaluate its effectiveness. Specifically, the ability to limit vibration propagation around each actuator was tested to assess the performance of the spatial confinement strategy. By applying the computed driving voltages, the resulting vibration fields were analyzed to verify whether confinement was achieved in the vicinity of each actuator, thus demonstrating the method's capability to locally control vibrational energy.

Three vibration confinement tests were conducted to validate the proposed control strategy. In the first test, the goal was to confine vibrations to the left side of the beam, as shown in Figure 3.11. The second test targeted the central region (Figure 3.13), and the third aimed to localize vibrations on the right side (Figure 3.12).

The simulation results validate the proposed control architecture for achieving vibration confinement in regions surrounding the actuator/sensor positions. Notably, the actuators located at the boundaries of the selected confinement zone apply higher forces compared to those within the confined region. This behavior highlights the role of peripheral actuators in counteracting vibrational energy leakage and maintaining spatial confinement. Since the simu-

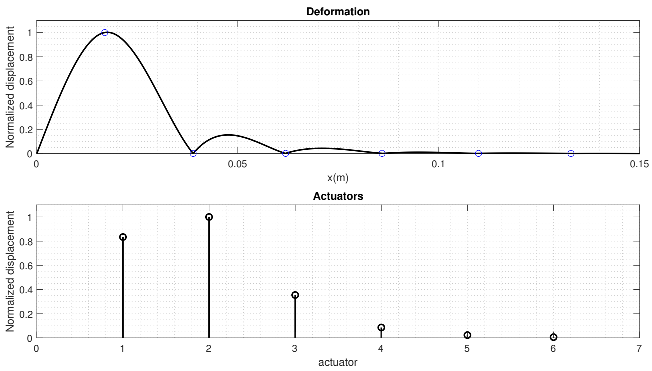

Figure 3.11: Result of simulation of the vibration confinement on the left

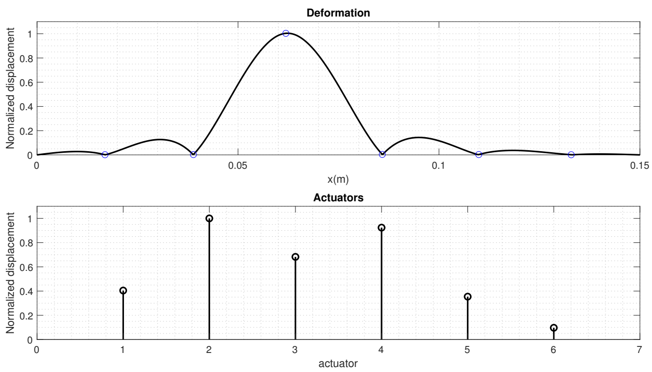

Figure 3.12: Result of simulation of the vibration confinement in the middle

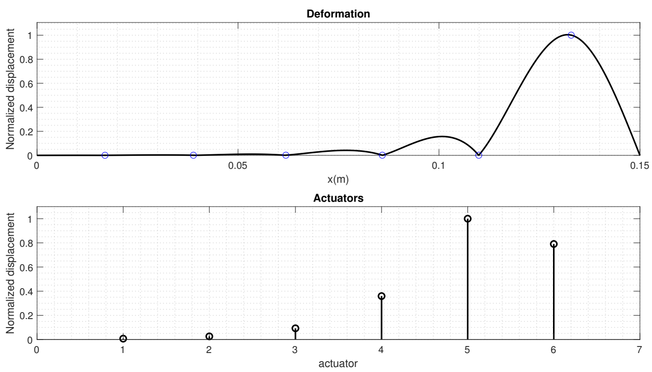

Figure 3.13: Result of simulation of the vibration confinement on the right

lations validate the effectiveness of the proposed control architecture, we proceeded with the development of an experimental prototype to further assess and validate the control strategy under real-world conditions.

3.4 Experimental validation of the sensors-actuators framework

Building on simulation validation, an experimental prototype was realized to evaluate three critical aspects under physical constraints: real-world confinement efficacy and practical implementation barriers.

3.4.1 Experimental Setup

Mechanical Setup

The experimental setup consists of a uniform steel beam with dimensions 150 mm×20 mm×1 mm, subjected to fixed-fixed boundary conditions. The choice of clamped-clamped boundary conditions was made primarily to achieve larger vibration amplitudes and, importantly, to ensure consistency in boundary conditions throughout all experimental tests. In contrast, maintaining consistent boundary conditions is typically challenging with free-free configurations. On the surface of one side of the beam, 6 piezoelectric ceramics actuators, each with dimensions of 12 mm×12 mm×0.3 mm were glued in a manner that ensured they were equidistantly spaced along the length of the beam. To act as sensors, 12 piezoelectric ceramics, each with dimensions of 12 mm×3 mm×0.3 mm, were placed as pairs on either side of the actuators, as depicted in Fig.3.14. The precise placement of these ceramics is critical for the uniform distribution of the induced strain when the actuators are subjected to electrical stimuli.

Electrical Hardware

A custom power electronics system drives the piezoelectric actuators. The system employs analog-to-digital converters (ADCs) to measure sinusoidal signals and pulse-width modulation (PWM) outputs to generate excitation signals. Control implementation is handled by an STM32F446 digital signal processor (DSP).

Since this strategy assumes constant-frequency excitation, we apply the control in the rotating frame as proposed in Chapter 2. The control involves two asynchronous process. A fast process, Direct Digital Synthesis (DDS), at a frequency of 40 kHz (T_s= 25 µm), generates the voltage reference that is then applied to supply the actuators using PWM. The voltage is generated consid-

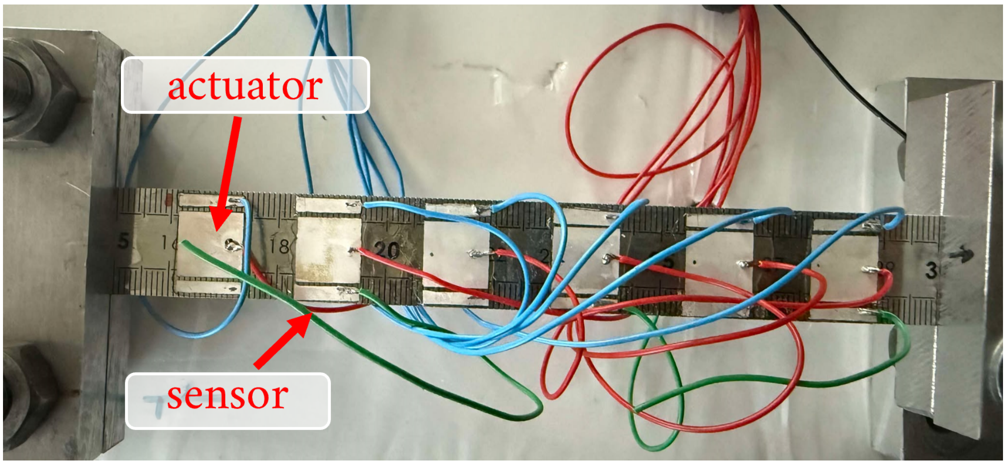

Figure 3.14: Picture of the prototype showing the placement of actuators and sensors

ering only the real part of the voltage described in:

$$v(t_k) = V_d \cos(\omega t_k) - V_q \sin(\omega t_k) \tag{3.38}$$

where $t_k = kT_s$ and k is the sample number.
The DSP also calculates the d-q component of the vibrations as follows :

$$W_d = \frac{1}{N_s} \sum_{i=0}^{N_s-1} w(t_i) \cos(\omega t_i) \tag{3.39}$$

$$W_q = \frac{1}{N_s} \sum_{i=0}^{N_s-1} w(t_i) \sin(\omega t_i) \tag{3.40}$$

.

where N_s is the number of samples per period of oscillation. In contrast to the fixed-frequency implementation in the preceding chapter, the slower control process now operates synchronously with the application excitation frequency. This modification aligns process dynamics directly with the target operational vibration range of 100 Hz to 4000 Hz, optimizing computational resource allocation for low-frequency haptic feedback applications.

In addition to the DSP, the control board integrates a dedicated driving circuit. This circuit comprises six identical MOSFET-based half-bridges, each serving as a DC-AC converter for the independent actuation of the six piezoelectric transducers. As illustrated in Figure 3.15, each half-bridge consists of two MOSFET switches and a corresponding gate driver.

The power stage is designed with consideration for the capacitive behavior of the piezoelectric elements, generating a sinusoidal voltage centered around

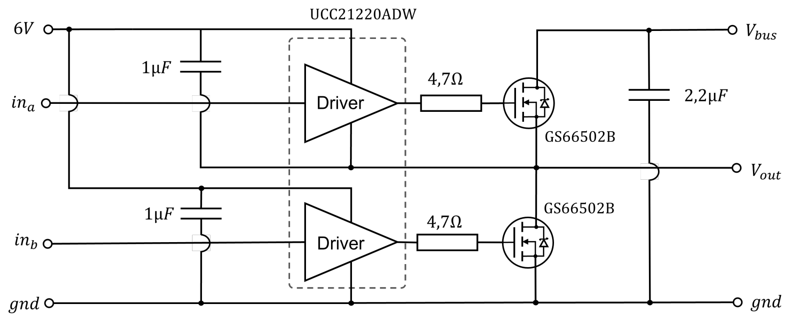

Figure 3.15: Half bridge structure

a DC offset of $V_{\text{bus}}/2$. The actuation signal is produced via pulse-width modulation (PWM), with the PWM signals synthesized by the DSP. This architecture allows for operation over a wide frequency range, supporting flexible and efficient control of the piezoelectric actuators.

A second order low-pass filter is added at the output of the inverter. The components of the low pass filter L_f, R_f were chosen, considering the piezoelectric actuators blocked capacitance C_p. The resulting low pass filter transfer function can be expressed as :

$$F(s) = \frac{1}{L_f(C_p)s^2 + Rf(C_p)s + 1} \tag{3.41}$$

The cutoff angular frequency of the filter, given by $\omega_f = \frac{1}{2\pi\sqrt{L_p C_p}}$, is selected to be higher than the operating frequency and lower than the PWM frequency. The complete schematics of the electronic architecture is presented in 3.16.

3.4.2 Characterization of the setup

Before validating the vibration confinement strategy, it is essential to first characterize the frequency response of the beam. This step is crucial for identifying suitable actuation frequencies at which the control law can be effectively applied. As previously established, active vibration confinement cannot be implemented at the natural frequencies of the beam's vibration modes, due to the dominance of a single mode that impedes spatial selectivity. Instead, the control must be applied at intermediate frequencies between modal resonances, where the system response is distributed among multiple modes, enabling effective confinement.

The experimental frequency response of the setup (Figure 3.17) was obtained by performing a sine sweep excitation spanning 100 Hz to 4500 Hz on

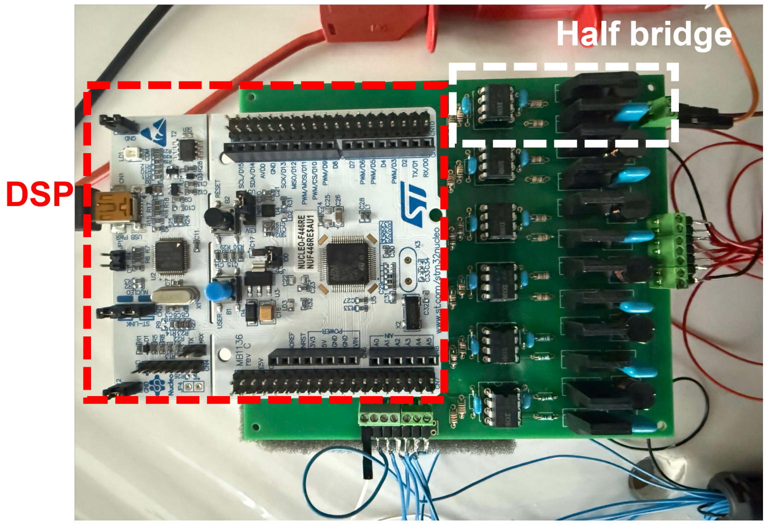

(a) The experimental electronic setup

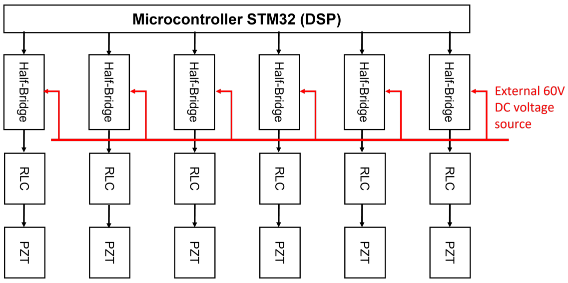

(b) Electronic schematics

Figure 3.16: The electronic setup

one of the actuators while recording the responses from all sensors. The resulting frequency response reveals the presence of several distinct vibration modes, as expected, but also it is observed that the low frequencies are attenuated. A comparison of the ADC input capacitance with the blocked capacitance of the piezoelectric ceramics revealed an impedance mismatch, causing derivative behavior that corrupted low-frequency measurements. As a result, the operating frequency was limited to 2 kHz–2.5 kHz.

Before presenting the experimental results, we begin by outlining two major limitations of the proposed control architecture that were identified during preliminary testing. Furthermore, we propose a methodology for evaluating these limitations where possible. This analysis is essential for identifying potential areas of improvement and guiding future developments.

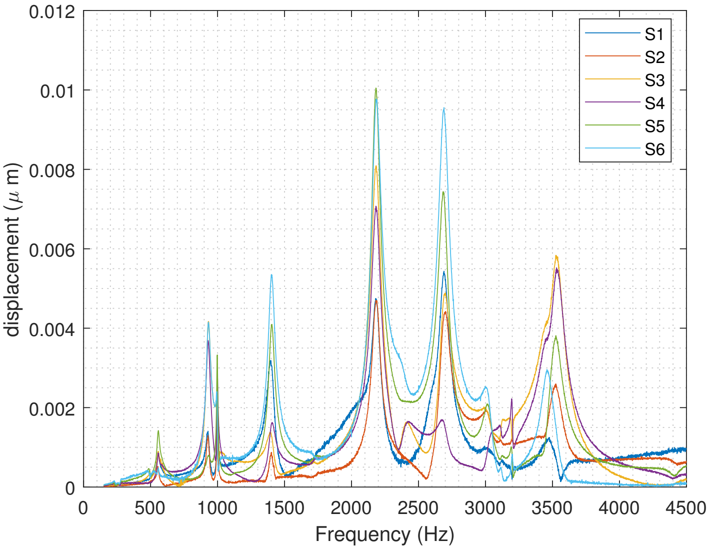

Figure 3.17: Frequency response of the experimental setup

3.4.3 Limitation of the experimental setup

Preliminary tests and experimental observations revealed two major limitations in the implementation of our control architecture:

- Low signal-to-noise ratio due to weak vibration amplitudes.
- Degeneracy of the transmitance matrix $\boldsymbol{T}$ at specific excitation frequencies.

High signal to noise ratio

The small amplitude of vibrations leads to low sensor signal levels, particularly evident in the frequency response for excitation frequencies below 2 kHz. Under these conditions, the signal-to-noise ratio becomes critically low, making the measurements highly vulnerable to noise interference. Furthermore, the weak signal amplitudes exacerbate susceptibility to crosstalk phenomena between adjacent piezoelectric sensors. As a result, the electrical signals measured by the sensors may not accurately represent the actual mechanical vibrations. This undermines the reliability of the sensing process and, consequently, the effectiveness of the feedback-based control strategy.

Control Authority Degeneracy in the Transmittance Matrix

The Equation (3.36) at a given can be developed as follows

$$\begin{bmatrix} \underline{W}_1 \\ \underline{W}_2 \\ \vdots \\ \underline{W}_N \end{bmatrix} = \begin{bmatrix} T_{11} & T_{12} & \dots & T_{1N} \\ T_{21} & T_{22} & \dots & T_{2N} \\ \vdots & \vdots & \ddots & \vdots \\ T_{N1} & T_{N1} & \dots & T_{NN} \end{bmatrix} \begin{bmatrix} V_1 \\ V_2 \\ \vdots \\ V_N \end{bmatrix} \tag{3.42}$$

The fundamental objective remains independent vibration amplitude control at each location through coordinated actuation. Physically, a line of the matrix $\boldsymbol{T}$ encodes how the vibrations generated by the set of actuators is converted to a measurement. When the measurements become similar, e.g at the vicinity of a resonance, $\boldsymbol{T}$ conditionning decreases, indicating a degeneracy of the matrix. This mathematical condition reveals physical limitations in achieving localized vibration control, as degenerate actuator pairs cannot be driven to produce distinct amplitude distributions at their respective sensor positions.
Therefore, it is necessary to evaluate the condition of the matrix at a given frequency.

Orthogonality Matrix The coupling matrix $\boldsymbol{T}$ is first normalized as follows:

$$\boldsymbol{T}_{\text{norm}} = \frac{\boldsymbol{T}\boldsymbol{T}^H}{\|\boldsymbol{T}\|_2} \tag{3.43}$$

where $\boldsymbol{T}^H$ is the hermitian transpose of $\boldsymbol{T}$.

This normalized matrix is expressed row-wise as:

$$\boldsymbol{T}_{\text{norm}} = \begin{bmatrix} \boldsymbol{T}_1 \\ \vdots \\ \boldsymbol{T}_N \end{bmatrix} \tag{3.44}$$

Each row $\boldsymbol{T}_j$ represents the normalized interaction vector for sensor j. The orthogonality matrix $\boldsymbol{ORT}$ is then constructed by computing the dot product between every pair of rows (including self-products):

$$\mathbf{ORT} = \begin{bmatrix} O_{11} & \cdots & O_{1N} \\ \vdots & \ddots & \vdots \\ O_{N1} & \cdots & O_{NN} \end{bmatrix} \tag{3.45}$$

Each entry O_{ij} ranges between 0 and 1. A value of $O_{ij} \approx 1$ indicates strong similarity or coupling between sensors i and j, while $O_{ij} \approx 0$ implies near orthogonality, i.e., negligible coupling.

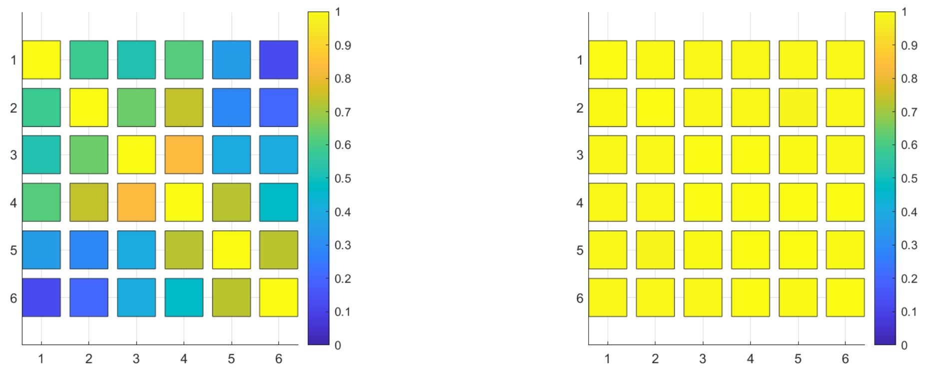

(a) Orthogonality matrix at 2.4 kHz

(b) Orthogonality matrix at 2.2 kHz

Figure 3.18: Orthogonality matrices

Figure 3.18a illustrates the orthogonality matrix at 2.4 kHz, which is nearly diagonal, confirming weak coupling among sensors. Conversely, Figure 3.18b reveals a dense matrix structure at 2.2 kHz, indicative of strong coupling, as expected near a modal resonance.

Interpretation Through Examples To further interpret the orthogonality matrix, we analyze two representative cases:

- The first case corresponds to matrix $\mathbf{T}$ identified at 2.4 kHz, associated with an experimental condition validated later in this chapter.
- The second case is derived from $\mathbf{T}$ identified at 2.2 kHz, which aligns with a resonance frequency—where decoupling via matrix inversion is known to fail.

Coupling Evaluation Criterion

To quantify the global degree of sensor coupling, we define a scalar criterion η as follows:

$$\eta = \frac{\|\mathbf{ERR}\|_2}{N-1}, \quad \text{where} \quad \mathbf{ERR} = 1 - \mathbf{ORT} \tag{3.46}$$

Here, **ERR** represents the deviation from perfect orthogonality. A value of η close to 1 indicates minimal coupling, whereas $\eta \approx 0$ reflects strong coupling among sensors.

Applying this metric to the two previously described cases yields:

$$\eta_{2400} = 0.46 \qquad \eta_{2200} = 0.0092$$

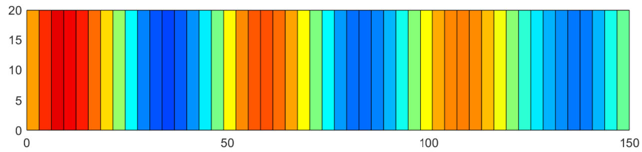

Figure 3.19: Vibration mode at 2.2 kHz used to calibrate the sensors

These values confirm the low degeneracy of the transmission matrix at certain frequencies. 2.4 kHz and the severe coupling at 2.2 kHz, validating the limitations of matrix inversion in the presence of modal resonance.

All experimental vibration results were measured using a laser Doppler vibrometer (LDV), with data acquired along the centerline of the beam. A spatial resolution of 3 mm was used, providing 50 measurement points along the total beam length of 150 mm.

3.4.4 Sensors Calibration

Before applying our control architecture to achieve vibration confinement, it is necessary to first calibrate the sensors, as they only provide measurements in the form of voltages generated by the piezoelectric elements during vibration. To perform this calibration, we excite the structure to generate a standing wave, corresponding to one of its natural vibration modes. A standing wave was used to avoid phase change as in a travelling wave. However, due to the effects of the measurement chain—including potential delays introduced by the electronics—the measured phase may be altered. Additionally, calibration is needed to establish the relationship between the measured voltage and the actual vibration amplitude at each sensor location.

Figure 3.19 illustrates the vibration measured by LDV laser of the vibration mode used for this calibration. This mode, which occurs just below our operational frequency, exhibits six anti nodes—matching the number of sensors in our setup. The objective is to calibrate the sensor voltages against the vibration amplitude at the center of each sensor. It is evident from the figure that the sensor locations are positioned very close to the center of each anti node, providing a suitable condition for accurate calibration. Multiple vibration amplitudes where used in order to calibrate measurement and ensure linearity.

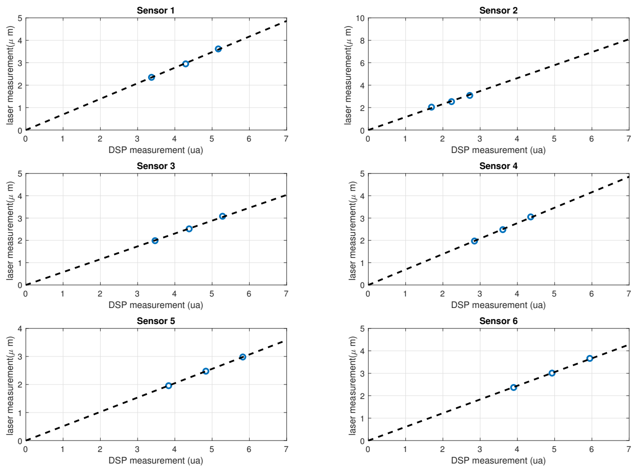

Figure 3.20: Comparison of Vibration Amplitude Measurements: DSP and Laser

Figure 3.20 demonstrates that the amplitude of the measured vibration is linearly correlated with the voltage values acquired by the DSP via its ADC. This linear relationship validates the proportionality assumption between sensor voltage and vibration amplitude. In Figure 3.21, the demodulated measurements done by the DSP $\underline{W}_d$ and $\underline{W}_q$ (red), and the demodulated displacement obtained using the laser vibrometer (blue) are depicted. A consistent phase shift is observed in the measurements, likely introduced by the signal conditioning chain. Both the phase shift and the gain ratio are accounted for during the sensor calibration process, ensuring that the measured signals accurately reflect the mechanical behavior of the system.

3.5 Vibration propagation without the control architecture

Before applying the control architecture, the natural propagation of vibrations when exciting a single actuator is assessed. This step ensures that, in the absence of control, vibrational energy is not inherently confined and spreads across the structure as expected. Figure 3.22 illustrates the vibration response of the beam when only the actuator located on the left side is excited. As shown, the vibration propagates throughout the entire surface of the beam, confirming that no natural confinement occurs and establishing a baseline for evaluating the effectiveness of the proposed control strategy.

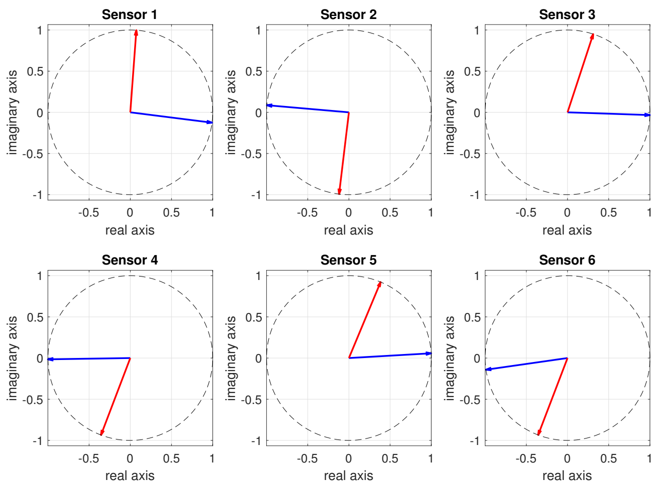

Figure 3.21: Phase shift between vibration measurement of the DSP and measurement by laser

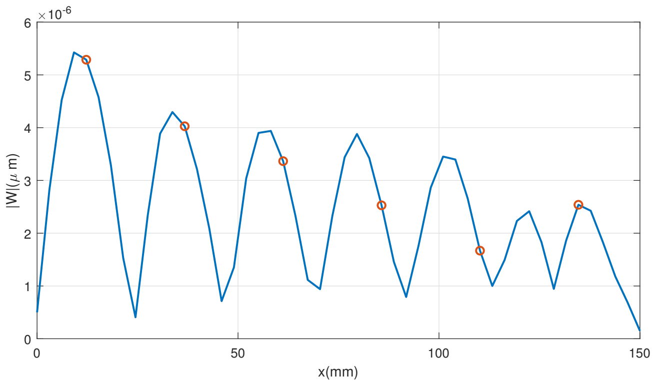

Figure 3.22: Vibration propagation without control: solid blue line — laser measurement;red circles — sensor positions.

3.6 Vibration confinement results

To validate our control architecture ability to confine vibration around an actuator/sensor, we aimed to recreate the same deformation as the one we tried in simulation part. The vibration confinement was tested in 3 cases of vibration confinement one at the left 3.23 , middle 3.24 and right 3.25 of the the beam.

Figures 3.23b, 3.24b, and 3.25b show that, under the proposed control strategy, the displacements measured by the sensors closely follow their respective reference signals. Quantitative measurements along the beam further confirm successful vibration confinement: in all test cases, amplitudes within the target zone exceed those in peripheral regions by a factor of 3–4. These results demonstrate both spatial energy focusing—beneficial for enhancing haptic perception—and suppression of parasitic vibrations, which are key requirements for scalable, large-area interfaces.

In particular, for the case where confinement is targeted at the center of the beam, the results demonstrate the most effective confinement: the vibration amplitude at the desired sensor region is nearly four times greater than the maximum amplitude observed at any other location on the structure. Moreover, when vibration confinement is applied at the edges of the beam, the results show a gradual attenuation of the vibration amplitude outside the targeted region. Although the confinement is slightly less pronounced than in the central case, the vibrations remain effectively concentrated within the intended area.

Moreover, in contrast to the simulation results, the experimental observations reveal that the voltages (and thus the forces) applied by the actuators located within the intended confinement region are greater than those applied by the other actuators. However, it is still evident that the actuators positioned closer to the confinement boundaries contribute more significantly than those farther away. This highlights the critical role of boundary actuators in reinforcing confinement by counteracting vibrational leakage beyond the targeted zone.

Since we have validated that the proposed control scheme successfully enables vibration confinement, we now extend its application to the generation of different vibration patterns on the structure. The flexibility of the control architecture allows for the precise shaping of vibrational energy, enabling the synthesis of diverse spatial distributions tailored to the needs of specific applications. In this experimental study, we focus on the generation of traveling waves—a class of dynamic patterns characterized by spatial and temporal phase shifts. Traveling waves are particularly valuable in applications ranging from haptics and tactile displays to ultrasonic manipulation and structural health monitoring, where directional control over vibration propagation can

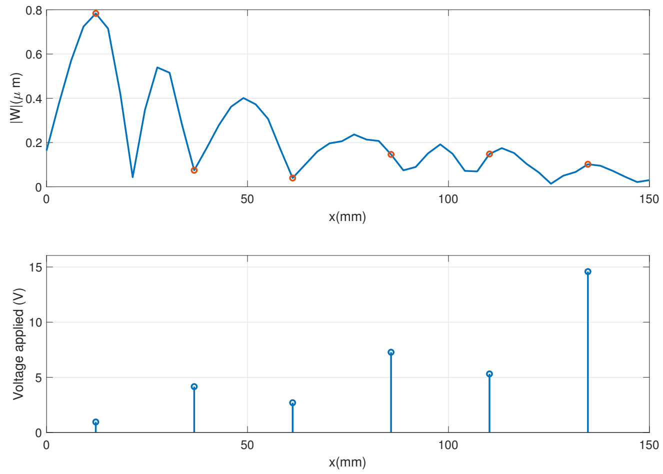

(a) Vibration propagation without control: solid blue line — laser measurement;red circles — sensor positions..

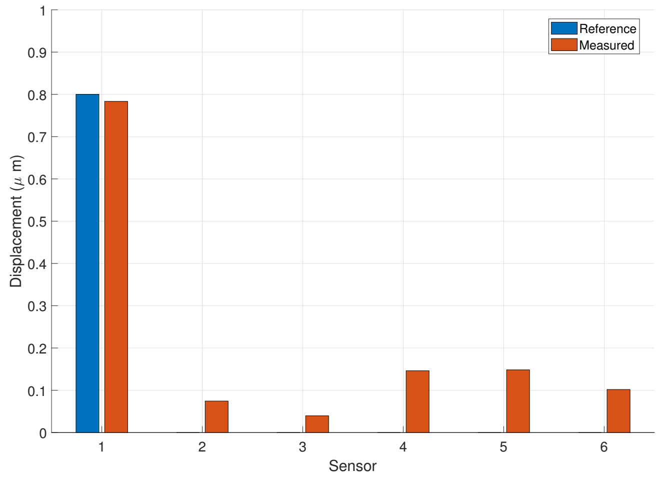

(b) Comparison of measured vibrations vs the reference

Figure 3.23: Vibration confinement test on the left side of the beam

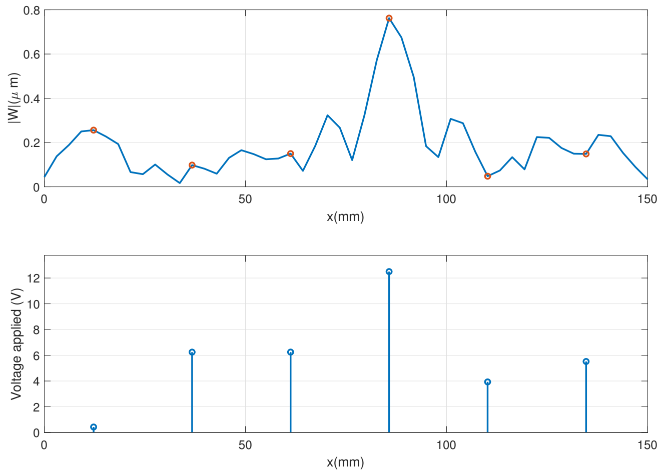

(a) Vibration propagation without control: solid blue line — laser measurement;red circles — sensor positions.

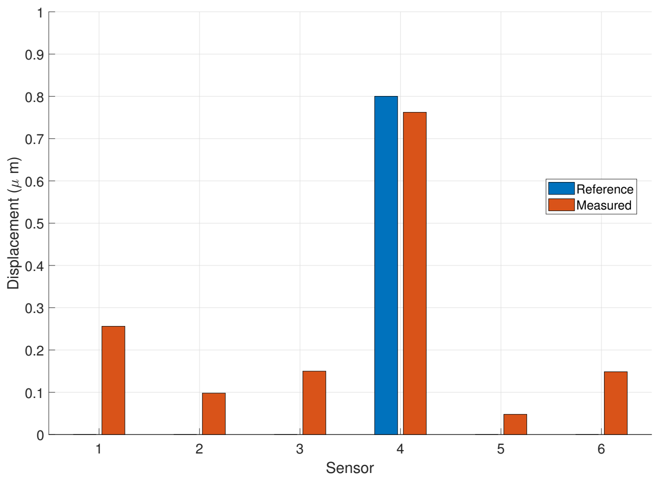

(b) Comparison of measured vibrations vs the reference

Figure 3.24: Vibration confinement test in the middle of the beam

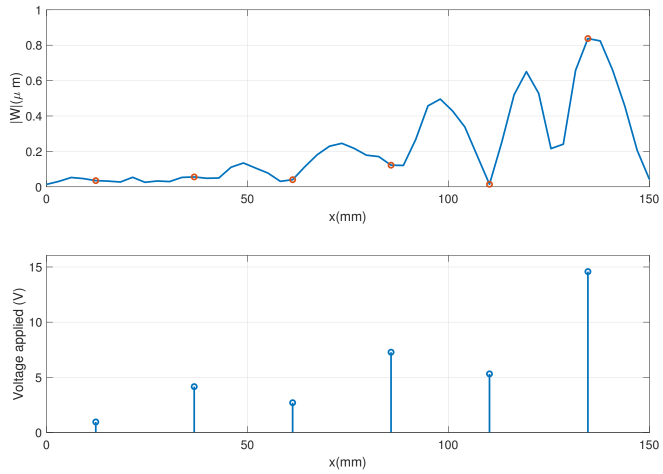

(a) Vibration propagation without control: solid blue line — laser measurement;red circles — sensor positions.

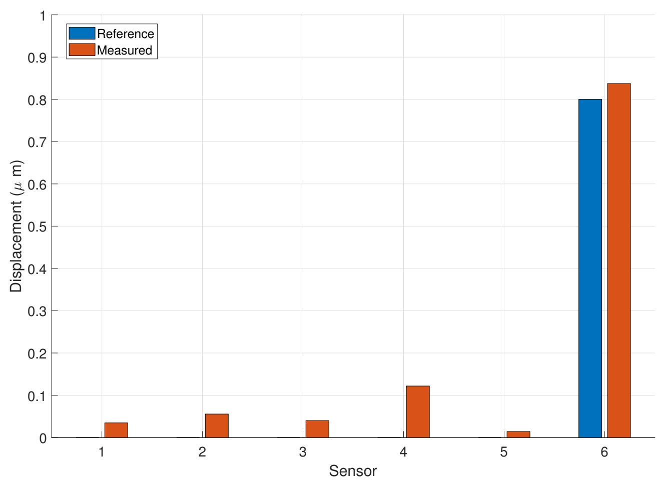

(b) Comparison of measured vibrations vs the reference

Figure 3.25: Vibration confinement test on the right side of the beam

facilitate user interaction, object transport, or localized excitation.

3.7 Generating traveling wave

Generating traveling waves is important in several fields beyond haptics. Unlike standing waves, which confine vibrational energy to fixed positions, traveling waves facilitate the transport of energy and momentum across a structure. This dynamic behavior is essential for enabling functions such as peristaltic pumping, where a sequence of propagating waves drives fluid flow in soft or flexible channels [85, 86]. Similarly, in granular and powder transport systems, traveling waves can be used to mobilize and control particulate materials without direct mechanical contact [87, 88]. In the field of haptics, traveling waves are particularly advantageous for generating shear forces that produce directional tactile cues on the skin [53, 54], offering a more immersive and controllable user experience. Thus, the ability to synthesize traveling waves expands the range of functional applications for vibration control and manipulation across both industrial and interactive domains.

Reference signals for traveling wave generation In a traveling wave, the displacement is a function of time and position, with:

$$w(x,t) = Asin\left(\omega t - 2\pi \frac{x}{\lambda}\right) \tag{3.47}$$

where λ is the wavelength. In a perfectly homogeneous medium, there is a relationship between λ and ω given by$\lambda = \frac{2\pi c}{\omega}$, where c is the sound speed in the medium. As a result, the displacement of the sensors located on the beam should undergo a displacement as follows:

$$W(j) = Asin(\omega t - 2\pi \frac{x_s(j)}{\lambda}) \quad j \in \{1 \ldots 6\} \tag{3.48}$$

where the location of the j_{th} is denoted $x_s(j)$. Consequently, the six displacements have the same amplitude but have a phase shift corresponding to its position.

Traveling wave ratio To evaluate the efficiency of the method, we calculate the *Traveling Wave Ratio* (TWR). It is defined as the complement of the Standing Wave Ratio (SWR), which quantifies the severity of standing wave patterns.

The Standing Wave Ratio is defined as:

$$\mathrm{SWR} = \frac{A_{\mathrm{max}} - A_{\mathrm{min}}}{A_{\mathrm{max}} + A_{\mathrm{min}}} \tag{3.49}$$

where A_{max} is the maximum amplitude across the beam, and A_{min} is the minimum amplitude.

This ratio can be interpreted as follows:

- SWR = 0: Pure traveling wave (no reflection)
- SWR = 1: Pure standing wave (total reflection)
- $0 < \text{SWR} < 1$: Mixed wave, with partial reflections forming standing wave patterns

Accordingly, the Traveling Wave Ratio is defined as:

$$\text{TWR} = 1 - \text{SWR} \tag{3.50}$$

Its interpretation is the complement of SWR:

- TWR = 0: Pure standing wave
- TWR = 1: Pure traveling wave
- $0 < \text{TWR} < 1$: Partial traveling wave, with some standing wave components

Experimental Results of Traveling Waves In order to generate various traveling wave patterns, we applied Equation (3.49), systematically varying the parameter k in the range from 10.5 to 13.9. This allowed us to investigate the effect of wavelength tuning on the resulting vibration profiles and to identify the values of k that produce the most efficient traveling wave behavior.

For each value of k, the Traveling Wave Ratio (TWR) was computed, as illustrated in Figure 3.26. The results indicate that the optimal performance was achieved for $\lambda = 6.6$ cm, where the TWR reached a value of 0.58. This means that in this configuration, approximately 60% of the total vibrational energy corresponds to a traveling wave component, highlighting a significant improvement in directional wave generation through proper wavelength tuning.

To visually evaluate the traveling wave behavior, Figures 3.27, 3.28, and 3.29 illustrate the vibration profiles corresponding to $\lambda = 5.9$, 6.6,7.4 cm, respectively. Each figure presents the displacement measured by the laser vibrometer, enabling direct observation of the resulting waveforms for different spatial phase configurations.

From these figures, it is evident that the case corresponding to $\lambda = 6.6$ exhibits the most prominent traveling wave behavior. In this scenario, the

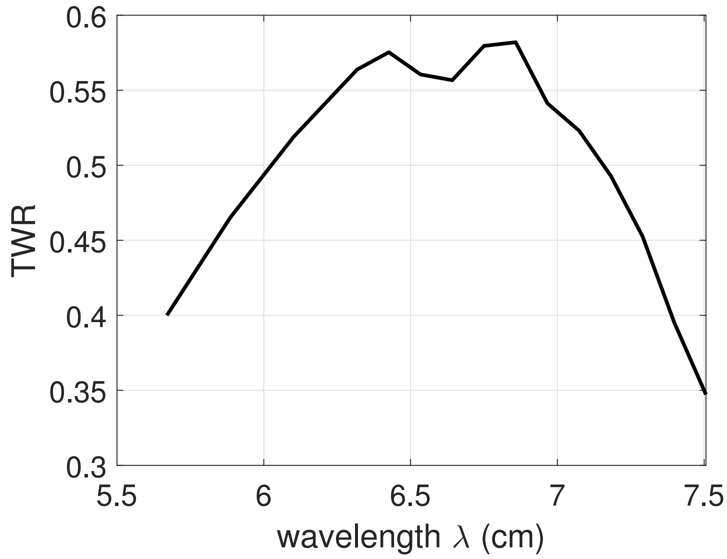

Figure 3.26: Travelling Wave ration in function of travelling wave wavelength k

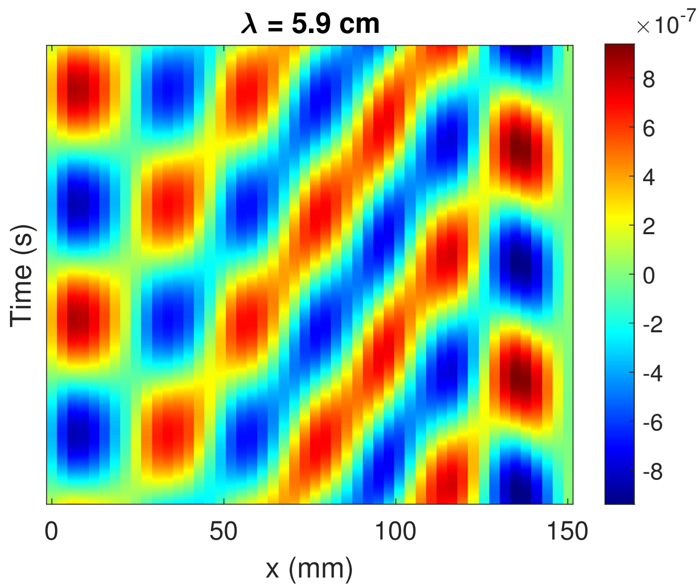

Figure 3.27: Traveling wave behavior at $\lambda = 5.9$

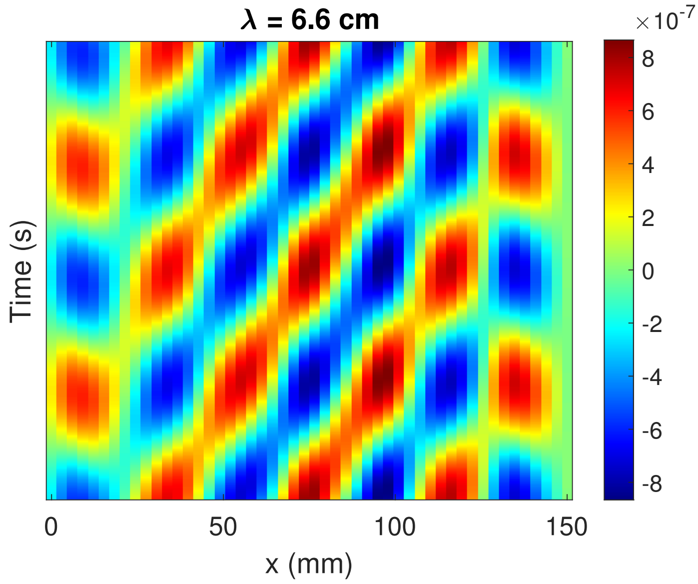

Figure 3.28: Traveling wave behavior at $\lambda = 6.6$

vibration pattern shows clearly defined and smoothly propagating diagonal anti-nodes over time—an indication of effective wave propagation. This contrasts with the other cases ($\lambda = 5.9$ and$\lambda = 7.4$), where the waveforms appear more stationary or distorted, suggesting a mixture of standing and traveling wave components. The visual coherence at $\lambda = 6.6$ supports the previously reported TWR maximum, highlighting this configuration as the most effective for generating a traveling wave.

Furthermore, even in the best-performing case ($\lambda = 7.4$), the figures reveal opportunities for improvement, as the resulting traveling wave is not perfectly formed. This suggests that the TWR could be increased further—potentially approaching unity—with enhancements to the experimental setup. One avenue for improvement lies in the use of smaller actuators and sensors, which could provide better spatial resolution and coupling, thus enabling finer control over the wave shape. Additionally, improving the calibration process is crucial; for instance, the current measurement resolution of 3 mm corresponds to a phase shift of approximately 20 to 30 degrees, which may introduce significant errors in the resulting waveform. Enhancing both hardware precision and calibration accuracy may therefore yield higher-fidelity traveling waves.

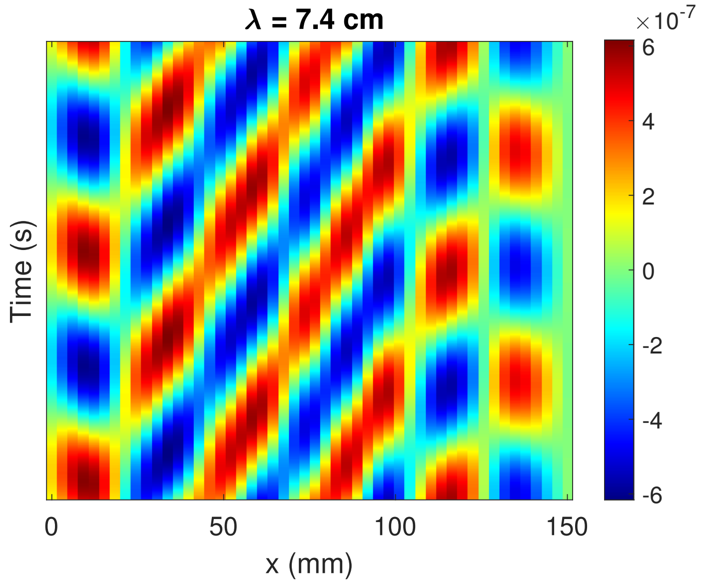

Figure 3.29: Traveling wave behavior at$\lambda = 7.4$

3.8 conclusion

In this chapter, we introduced and analyzed two control strategies aimed at achieving spatial confinement of vibrational energy in flexible structures. The first approach is rooted in an analogy with electrical resonant filters and demonstrated the ability to suppress vibrational propagation at specific frequencies using high-gain feedback control. However, simulations revealed critical limitations, notably the dependency on extremely high gain values and the resulting challenges with robustness, sensitivity to frequency variations, and practical implementation constraints.

To address these issues, a second, more comprehensive control architecture was developed based on modal superposition theory. This method models the structure as a superposition of its natural vibration modes, enabling the formulation of a spatial decoupling strategy through the inversion of an actuator–sensor interaction matrix. By targeting off-resonance frequencies and applying individualized control loops to each sensor/actuator pair, this architecture allows for the real-time confinement and dynamic shaping of vibration fields.

The theoretical formulation was validated via both analytical simulations and experimental implementation. Numerical results demonstrated successful confinement of vibrational energy around target regions, with higher actuation observed at the boundaries of the confinement zones to prevent energy leakage. Experimental validation confirmed these findings, though performance was impacted by low signal-to-noise ratios and degeneracy of the transmission matrix at certain frequencies. These effects were characterized using an orthogonality matrix and quantified by a scalar coupling metric, guiding the selection of operational frequencies.

Additionally, the flexibility of the proposed control architecture was leveraged to generate traveling waves—an important capability for applications in haptics and particle transport. By tuning the spatial phase reference to match the natural wavelength of the structure, a traveling wave ratio (TWR) of up to 0.58 was achieved, indicating substantial success in generating directional wave propagation.

Overall, this chapter establishes a robust foundation for active vibration confinement and spatial vibration pattern synthesis. While challenges remain — particularly in improving hardware resolution and noise robustness—the proposed control strategy demonstrates strong potential for practical applications in precision vibration control and advanced haptic interfaces.

General Conclusion

This thesis aimed to advance the field of ultrasonic surface haptics (USF) by developing and validating methods for localizing and controlling ultrasonic vibrations on smart surfaces. The central objective was to enable localized tactile feedback without compromising scalability, energy efficiency, or signal clarity—challenges that currently limit the widespread integration of USF into consumer and industrial applications.

To achieve this, the work developed a vibration confinement strategy based on mechanical electrical analogy. Based on that, two complementary approaches to vibration confinement were explored: passive confinement using mechanical resonators and active confinement using sensor-actuator networks and control algorithms. These approaches were developed independently, validated through simulations, and implemented in experimental prototypes.

The first contribution of this thesis was the design and validation of a passive method for vibration confinement using resonant mechanical pillars integrated into the surface structure. By tuning the resonant frequency of the pillars to match a targeted vibration mode of the active zone, energy transfer between the plate and the pillars was optimized. This interaction attenuates wave propagation and confines vibration within a specific region.

Finite Element Method (FEM) simulations validated the influence of geometrical and material parameters, such as pillar height, periodicity, and placement. The study further investigated the minimum number of pillar rows required to effectively contain the vibration field. Experimental results confirmed the viability of this method and demonstrated clear mode confinement with little energy leakage beyond the resonator boundaries.

One key insight was that passive confinement via mode conversion offers a low-energy, robust solution for applications requiring consistent tactile effects. However, it remains frequency-specific and lacks flexibility for dynamic reconfiguration or broadband operation.

To overcome the limitations of the passive approach, the second major contribution of this work introduced an active vibration confinement strategy. Based on modal superposition and sensor-actuator feedback, this method allows the dynamic shaping of the vibration field using real-time control.

The control architecture was first developed and validated through simulation. The proposed control strategy allowed the generation of user-defined vibration patterns, such as localization around specific actuators or the formation of traveling waves.

A full experimental prototype was designed, including custom driving electronics and a DSP-based control system. The experimental setup demonstrated the ability to confine and manipulate vibrations in real time. Various configurations showed how actuation amplitude and phase could be tailored to match desired spatial profiles, including traveling waves with controlled wavelength.

Despite its promising results, the active method also exposed several practical limitations. Control performance was highly dependent on signal-to-noise ratio, vulnerable to sensor crosstalk, and sensitive to calibration accuracy. In addition, the approach exhibited marked sensitivity to actuator coupling and to the choice of operating frequency. Finally, the achieved vibration amplitudes remained too low for the intended haptic application.

Building upon the findings and insights developed throughout this thesis, several promising directions emerge for future research in the domain of vibration confinement for the generation of ultrasonic surface friction (USF). These research avenues offer opportunities to propose innovative strategies and make novel contributions to the field.

One particularly compelling direction involves the development of a hybrid confinement strategy that combines both passive and active methods. Such an approach would leverage the mechanical robustness and inherent stability of passive resonators while incorporating the flexibility and adaptability offered by active control. This synergy could lead to confinement systems that are both reconfigurable and resilient, capable of maintaining performance across varying environmental and operational conditions.

Another area worth exploring is the design of passive confinement structures with broadband characteristics—i.e., capable of attenuating vibration modes over a wide frequency range. Integrating such a system with an active control layer could result in a confinement architecture that preserves boundary conditions mechanically while dynamically adapting the excitation patterns. This combination could enable active confinement across a broad frequency band, a critical requirement for applications where the operating frequency may vary or where multiple haptic effects need to coexist.

Finally, whether through active, passive, or hybrid strategies, future research could also aim to generate and control multiple sets of vibration modes or traveling waves simultaneously. This would make it possible to create and modulate localized ultrasonic shear forces on extended surfaces, thus enhancing spatial resolution and tactile richness. Achieving this goal would mark a significant advancement in the design of scalable and programmable haptic interfaces for next-generation interactive technologies.,

Bibliography

[1] H. A. Malik, S. Rasool, A. Maqsood, and R. Riaz, "Effect of Haptic Feedback on Pilot/Operator Performance During Flight Simulation," *Applied Sciences*, vol. 10, p. 3877, Jan. 2020.

[2] R. K, D. H, and P. Ph, "Systematic Review of Virtual Haptics in Surgical Simulation: A Valid Educational Tool?," *Journal of surgical education*, vol. 77, no. 2, 2020 Mar-Apr.

[3] V. Tanwar, V. Anand, P. Aggarwal, M. Kumar, and G. R. Kumar, "Revolutionizing Military Training: A Comprehensive Review of Tactical and Technical Training through Augmented Reality, Virtual Reality, and Haptics," in *2024 IEEE 9th International Conference for Convergence in Technology (I2CT)*, pp. 1–5, Apr. 2024.

[4] I. El Rassi and J.-M. El Rassi, "A review of haptic feedback in teleoperated robotic surgery," *Journal of Medical Engineering & Technology*, vol. 44, pp. 247–254, July 2020.

[5] S. Azher, A. Mills, J. He, T. Hyjazie, J. Tokuno, A. Quaiattini, and J. M. Harley, "Findings Favor Haptics Feedback in Virtual Simulation Surgical Education: An Updated Systematic and Scoping Review," *Surgical Innovation*, vol. 31, pp. 331–341, June 2024.

[6] K. Ito, J. Hosoi, K. Takanohashi, Y. Ban, and S. Warisawa, "Clothes Vibration Device for Producing Tactile Stimuli to Evoke the Perception of Strong Wind," in *2024 IEEE International Symposium on Mixed and Augmented Reality (ISMAR)*, pp. 1266–1275, Oct. 2024.

[7] M. Carroll and C. Yildirim, "The Effect of Body-Based Haptic Feedback on Player Experience During VR Gaming," in *Virtual, Augmented and*

Mixed Reality (J. Y. C. Chen and G. Fragomeni, eds.), (Cham), pp. 163–171, Springer International Publishing, 2021.

[8] M. Fontana, S. Fabio, S. Marcheschi, and M. Bergamasco, "Haptic Hand Exoskeleton for Precision Grasp Simulation," *Journal of Mechanisms and Robotics*, vol. 5, Oct. 2013.

[9] J. Rae-Dupree, "Feel the Precision: Next-Gen Robotic Surgery With Haptic Feedback," *IEEE Pulse*, vol. 16, pp. 12–15, Jan. 2025.

[10] A. A. Alsamarei and Bahar Şener, "Remote social touch framework: A way to communicate physical interactions across long distances," *Journal on Multimodal User Interfaces*, vol. 17, pp. 79–104, June 2023.

[11] P. Wang, X. Bai, M. Billinghurst, S. Zhang, D. Han, M. Sun, Z. Wang, H. Lv, and S. Han, "Haptic Feedback Helps Me? A VR-SAR Remote Collaborative System with Tangible Interaction," *International Journal of Human–Computer Interaction*, vol. 36, pp. 1242–1257, Aug. 2020.

[12] T. L. Baldi, G. Paolocci, D. Barcelli, and D. Prattichizzo, "Wearable Haptics for Remote Social Walking," *IEEE Transactions on Haptics*, vol. 13, pp. 761–776, Oct. 2020.

[13] K. Klein, "Rethinking touch HMI controls for automotive displays and smart surfaces," *Information Display*, vol. 38, no. 1, pp. 24–29, 2022.

[14] Y. Gaffary and A. Lécuyer, "The Use of Haptic and Tactile Information in the Car to Improve Driving Safety: A Review of Current Technologies," *Frontiers in ICT*, vol. 5, Mar. 2018.

[15] D. Wang, Y. Guo, S. Liu, Y. Zhang, W. Xu, and J. Xiao, "Haptic display for virtual reality: Progress and challenges," *Virtual Reality & Intelligent Hardware*, vol. 1, pp. 136–162, Apr. 2019.

[16] C. Basdogan, F. Giraud, V. Levesque, and S. Choi, "A Review of Surface Haptics: Enabling Tactile Effects on Touch Surfaces," *IEEE Transactions on Haptics*, vol. 13, pp. 450–470, July 2020.

[17] S. Choi and K. J. Kuchenbecker, "Vibrotactile Display: Perception, Technology, and Applications," *Proceedings of the IEEE*, vol. 101, pp. 2093–2104, Sept. 2013.

[18] "Boréas Piezo Haptic Engine."

[19] D. Dalecki, S. Z. Child, C. H. Raeman, and E. L. Carstensen, "Tactile perception of ultrasound," *The Journal of the Acoustical Society of America*, vol. 97, pp. 3165–3170, May 1995.

[20] T. Iwamoto and H. Shinoda, "Two-dimensional Scanning Tactile Display using Ultrasound Radiation Pressure," in *2006 14th Symposium on Haptic Interfaces for Virtual Environment and Teleoperator Systems*, pp. 57–61, Mar. 2006.

[21] C. Q. Howard, C. H. Hansen, and A. C. Zander, "A Review of Current Ultrasound Exposure Limits,"

[22] J.-H. Woo and J.-G. Ih, "Vibration rendering on a thin plate with actuator array at the periphery," *Journal of Sound and Vibration*, vol. 349, pp. 150–162, Aug. 2015.

[23] "Ultrasonic force field provides tactile sensations in midair," Oct. 2013.

[24] C. Hudin, J. Lozada, and V. Hayward, "Localized Tactile Feedback on a Transparent Surface through Time-Reversal Wave Focusing," *IEEE Transactions on Haptics*, vol. 8, pp. 188–198, Apr. 2015.

[25] R. Raisamo, K. Salminen, J. Rantala, A. Farooq, and M. Ziat, "Interpersonal Haptic Communication: Review and Directions for the Future," *International Journal of Human-Computer Studies*, vol. 166, p. 102881, Oct. 2022.

[26] C. Hudin, *Focalisation par retournement temporel dans les plaques minces : Application à la stimulation tactile*. PhD thesis, Université Pierre et Marie Curie - Paris VI, Mar. 2014.

[27] E. Enferad, C. Giraud-Audine, F. Giraud, M. Amberg, and B. L. Semail, "Generating controlled localized stimulations on haptic displays by modal superimposition," *Journal of Sound and Vibration*, vol. 449, pp. 196–213, June 2019.

[28] A. Kaci, C. Giraud-Audine, F. Giraud, M. Amberg, and B. Lemaire-Semail, "Closed loop control of vibration field transient: Application to wave focusing," *Mechanical Systems and Signal Processing*, vol. 167, p. 108285, Mar. 2022.

[29] A. Kaci, *Méthodologie de Commande de Vibrations Multimodales Par Modulation-Démodulation Synchrone : Application Au Retour Tactile "Multi-Touch"*. These de doctorat, Université de Lille (2018-2021), Sept. 2020.

[30] G. Robles-De-La-Torre and V. Hayward, "Force can overcome object geometry in the perception of shape through active touch," *Nature*, vol. 412, pp. 445–448, July 2001.

[31] E. Mallinckrodt, A. L. Hughes, and W. Sleator, "Perception by the Skin of Electrically Induced Vibrations," *Science*, vol. 118, pp. 277–278, Sept. 1953.

[32] E. Vezzoli, *Tactile Feedback Devices : Friction Control and Texture Generation*. These de doctorat, Lille 1, Sept. 2016.

[33] R. M. Strong and D. E. Troxel, "An Electrotactile Display," *IEEE Transactions on Man-Machine Systems*, vol. 11, pp. 72–79, Mar. 1970.

[34] O. Bau, I. Poupyrev, A. Israr, and C. Harrison, "TeslaTouch: Electrovibration for touch surfaces," in *Proceedings of the 23nd Annual ACM Symposium on User Interface Software and Technology*, UIST '10, (New York, NY, USA), pp. 283–292, Association for Computing Machinery, Oct. 2010.

[35] "Tanvas - Surface haptic technology and products."

[36] S.-C. Kim, A. Israr, and I. Poupyrev, "Tactile rendering of 3D features on touch surfaces," in *Proceedings of the 26th Annual ACM Symposium on User Interface Software and Technology*, UIST '13, (New York, NY, USA), pp. 531–538, Association for Computing Machinery, Oct. 2013.

[37] S. Grimnes, "Electrovibration, cutaneous sensation of microampere current," *Acta Physiologica Scandinavica*, vol. 118, pp. 19–25, May 1983.

[38] T. Watanabe and S. Fukui, "A method for controlling tactile sensation of surface roughness using ultrasonic vibration," in *Proceedings of 1995 IEEE International Conference on Robotics and Automation*, vol. 1, pp. 1134–1139 vol.1, May 1995.

[39] M. Biet, *Conception et Contrôle d'actionneurs Électro-Actifs Dédiés à La Stimulation Tactile*. These de doctorat, Lille 1, Jan. 2007.

[40] "STIMTAC | Proceedings of the 24th annual ACM symposium adjunct on User interface software and technology."

[41] F. Giraud, M. Amberg, B. Lemaire-Semail, and G. casiez, "Design of a transparent tactile stimulator," in *2012 IEEE Haptics Symposium (HAPTICS)*, pp. 485–489, Mar. 2012.

[42] E. Vezzoli, T. Sednaoui, M. Amberg, F. Giraud, and B. Lemaire-Semail, "Texture Rendering Strategies with a High Fidelity - Capacitive Visual-Haptic Friction Control Device," in *Haptics: Perception, Devices, Control, and Applications*, pp. 251–260, Springer, Cham, 2016.

[43] A. Minikes and I. Bucher, "Comparing numerical and analytical solutions for squeeze-film levitation force," *Journal of Fluids and Structures*, vol. 22, pp. 713–719, July 2006.

[44] A. Minikes and I. Bucher, "Coupled dynamics of a squeeze-film levitated mass and a vibrating piezoelectric disc: Numerical analysis and experimental study," *Journal of Sound and Vibration*, vol. 263, pp. 241–268, May 2003.

[45] T. Sednaoui, E. Vezzoli, B. Dzidek, B. Lemaire-Semail, C. Chappaz, and M. Adams, "Experimental evaluation of friction reduction in ultrasonic devices," in *2015 IEEE World Haptics Conference (WHC)*, pp. 37–42, June 2015.

[46] N. Huloux, C. Bernard, and M. Wiertlewski, "Estimating Friction Modulation From the Ultrasonic Mechanical Impedance," *IEEE Transactions on Haptics*, vol. 14, pp. 409–420, Apr. 2021.

[47] M. Wiertlewski, R. Fenton Friesen, and J. E. Colgate, "Partial squeeze film levitation modulates fingertip friction," *Proceedings of the National Academy of Sciences*, vol. 113, pp. 9210–9215, Aug. 2016.

[48] D. A. Torres, B. Lemaire-Semail, C. Giraud-Audine, F. Giraud, and M. Amberg, "Design and control of an ultrasonic surface haptic device for longitudinal and transverse mode comparison," *Sensors and Actuators A: Physical*, vol. 331, p. 113019, Nov. 2021.

[49] A. Imaizumi, S. Okamoto, and Y. Yamada, "Friction Sensation Produced by Laterally Asymmetric Vibrotactile Stimulus," in *Haptics: Neuroscience, Devices, Modeling, and Applications*, pp. 11–18, Springer, Berlin, Heidelberg, 2014.

[50] E. C. Chubb, J. E. Colgate, and M. A. Peshkin, "ShiverPad: A device capable of controlling shear force on a bare finger," in *World Haptics 2009 - Third Joint EuroHaptics Conference and Symposium on Haptic Interfaces for Virtual Environment and Teleoperator Systems*, pp. 18–23, Mar. 2009.

[51] J. Mullenbach, M. Peshkin, and J. E. Colgate, "eShiver: Force feedback on fingertips through oscillatory motion of an electroadhesive surface," in *2016 IEEE Haptics Symposium (HAPTICS)*, pp. 271–276, Apr. 2016.

[52] H. Xu, M. A. Peshkin, and J. E. Colgate, "UltraShiver: Lateral Force Feedback on a Bare Fingertip via Ultrasonic Oscillation and Electroadhesion," *IEEE Transactions on Haptics*, vol. 12, pp. 497–507, Oct. 2019.

[53] S. Ghenna, E. Vezzoli, C. Giraud-Audine, F. Giraud, M. Amberg, and B. Lemaire-Semail, "Enhancing Variable Friction Tactile Display Using an Ultrasonic Travelling Wave," *IEEE Transactions on Haptics*, vol. 10, pp. 296–301, Apr. 2017.

[54] Z. Cai and M. Wiertlewski, "Ultraloop: Active Lateral Force Feedback Using Resonant Traveling Waves," *IEEE Transactions on Haptics*, vol. 16, pp. 652–657, Oct. 2023.

[55] Xiaowei Dai, J. E. Colgate, and M. A. Peshkin, "LateralPaD: A surface-haptic device that produces lateral forces on a bare finger," in *2012 IEEE Haptics Symposium (HAPTICS)*, (Vancouver, BC, Canada), pp. 7–14, IEEE, Mar. 2012.

[56] P. Garcia, F. Giraud, B. Lemaire-Semail, M. Rupin, and M. Amberg, "2MoTac: Simulation of Button Click by Superposition of Two Ultrasonic Plate Waves," in *Haptics: Science, Technology, Applications* (I. Nisky, J. Hartcher-O'Brien, M. Wiertlewski, and J. Smeets, eds.), vol. 12272, (Cham), pp. 343–352, Springer International Publishing, 2020.

[57] S. J. Breitschaft, S. Clarke, and C.-C. Carbon, "A Theoretical Framework of Haptic Processing in Automotive User Interfaces and Its Implications on Design and Engineering," *Frontiers in Psychology*, vol. 10, July 2019.

[58] A. B. Dhiab and C. Hudin, "Confinement of Vibrotactile Stimuli in Narrow Plates: Principle and Effect of Finger Loading," *IEEE Transactions on Haptics*, vol. 13, pp. 471–482, July 2020.

[59] A. Ben Dhiab, *Confinement of Vibrations for Localized Surface Haptics*. These de doctorat, Sorbonne université, Apr. 2022.

[60] A. Ben Dhiab and C. Hudin, "Confinement of Vibrotactile Stimuli in Periodically Supported Plates," in *Haptics: Science, Technology, Applications*, pp. 334–342, Springer, Cham, 2020.

[61] J. C. Maxwell, *The Scientific Papers of James Clerk Maxwell*. Cambridge University Press, 1 ed., Jan. 2011.

[62] D. T. Moore, "Gradient-index optics: A review," *Applied Optics*, vol. 19, pp. 1035–1038, Apr. 1980.

[63] W. E. Kock and F. K. Harvey, "Refracting Sound Waves," *The Journal of the Acoustical Society of America*, vol. 21, pp. 471–481, Sept. 1949.

[64] Y. Jin, R. Kumar, O. Poncelet, O. Mondain-Monval, and T. Brunet, "Flat acoustics with soft gradient-index metasurfaces," *Nature Communications*, vol. 10, p. 143, Jan. 2019.

[65] A. Pelat, F. Gautier, S. C. Conlon, and F. Semperlotti, "The acoustic black hole: A review of theory and applications," *Journal of Sound and Vibration*, vol. 476, p. 115316, June 2020.

[66] M. A. Butt, S. N. Khonina, and N. L. Kazanskiy, "Recent advances in photonic crystal optical devices: A review," *Optics & Laser Technology*, vol. 142, p. 107265, Oct. 2021.

[67] A. Khelif, A. Choujaa, S. Benchabane, B. Djafari-Rouhani, and V. Laude, "Guiding and bending of acoustic waves in highly confined phononic crystal waveguides," *Applied Physics Letters*, vol. 84, pp. 4400–4402, May 2004.

[68] T. Daunizeau, D. Gueorguiev, S. Haliyo, and V. Hayward, "Phononic Crystals Applied to Localised Surface Haptics," *IEEE Transactions on Haptics*, vol. 14, pp. 668–674, July 2021.

[69] C. Hudin and S. Panëels, "Localisation of Vibrotactile Stimuli with Spatio-Temporal Inverse Filtering," in *Haptics: Science, Technology, and Applications* (D. Prattichizzo, H. Shinoda, H. Z. Tan, E. Ruffaldi, and A. Frisoli, eds.), Lecture Notes in Computer Science, (Cham), pp. 338–350, Springer International Publishing, 2018.

[70] K. Dekemele, C. Giraud-Audine, and O. Thomas, "A piezoelectric nonlinear energy sink shunt for vibration damping," *Mechanical Systems and Signal Processing*, vol. 220, p. 111615, Nov. 2024.

[71] M. Alshaqaq, C. Sugino, and A. Erturk, "Programmable Rainbow Trapping and Band-Gap Enhancement via Spatial Group-Velocity Tailoring in Elastic Metamaterials," *Physical Review Applied*, vol. 17, p. L021003, Feb. 2022.

[72] Mason, WP, *Electromechanical Transducers and Wave Filters*. 1948.

[73] M. Rupin, *Cavité réverbérante et résonateurs sub-longueur d'onde : approches numériques et expérimentales*. PhD thesis, Université de Grenoble, Apr. 2014.

[74] F. Giraud, M. Amberg, B. Lemaire-Semail, and C. Giraud-Audine, "Using an ultrasonic transducer to produce tactile rendering on a touchscreen," in *2014 Joint IEEE International Symposium on the Applications of Ferroelectric, International Workshop on Acoustic Transduction Materials and Devices & Workshop on Piezoresponse Force Microscopy*, pp. 1–4, May 2014.

[75] S. Ghenna, *Approche Multimodale Pour La Conception d'interface à Retour Tactile à Plusieurs Doigts*. These de doctorat, Lille 1, Nov. 2016.

[76] S. Timoshenko, *History of Strength of Materials: With a Brief Account of the History of Theory of Elasticity and Theory of Structures*. Courier Corporation, Jan. 1983.

[77] M. Geradin and D. J. Rixen, *Mechanical Vibrations: Theory and Application to Structural Dynamics*. John Wiley & Sons, Feb. 2015.

[78] M. S. Kushwaha, P. Halevi, L. Dobrzynski, and B. Djafari-Rouhani, "Acoustic band structure of periodic elastic composites," *Physical Review Letters*, vol. 71, pp. 2022–2025, Sept. 1993.

[79] A. Preumont, *Vibration Control of Active Structures*, vol. 246 of *Solid Mechanics and Its Applications*. Cham: Springer International Publishing, 2018.

[80] F. Giraud and C. Giraud-Audine, *Piezoelectric Actuators: Vector Control Method: Basic, Modeling and Mechatronic Design of Ultrasonic Devices*. Kidlington, Oxford Cambridge, MA: Butterworth-Heinemann, Apr. 2019.

[81] S. Ghenna, F. Giraud, C. Giraud-Audine, and M. Amberg, "Vector Control of Piezoelectric Transducers and Ultrasonic Actuators," *IEEE Transactions on Industrial Electronics*, vol. 65, pp. 4880–4888, June 2018.

[82] M. Abu-Hilal, "Forced vibration of Euler–Bernoulli beams by means of dynamic Green functions," *Journal of Sound and Vibration*, vol. 267, pp. 191–207, Oct. 2003.

[83] R. Teodorescu, F. Blaabjerg, M. Liserre, and P. Loh, "Proportional-resonant controllers and filters for grid-connected voltage-source converters," *IEE Proceedings - Electric Power Applications*, vol. 153, pp. 750–762, Sept. 2006.

[84] L. Meirovitch, *Fundamentals of Vibrations*. Waveland Press, June 2010.

[85] F. Pigache, L. Coutant, J. M. Fontaine, and L. Pernod, "Peristaltic pumping by huge amplitude piezoelectric traveling wave actuator," in *2021 IEEE International Workshop of Electronics, Control, Measurement, Signals and Their Application to Mechatronics (ECMSM)*, pp. 1–6, June 2021.

[86] J. M. Floryan, S. Panday, and Kh. Md. Faisal, "On the peristaltic pumping," *Physics of Fluids*, vol. 33, p. 033609, Mar. 2021.

[87] I. Mahi, R. Messafeur, A. Belgacem, Y. Bellebna, H. Louati, and A. Tilmatine, "New separation method of metal/plastic micronized particles using travelling wave conveyors," *International Journal of Environmental Studies*, vol. 75, pp. 788–799, Sept. 2018.

[88] K. Masuda, D. Koyama, and M. Matsukawa, "Noncontact Transportation of Planar Object in an Ultrasound Waveguide," *IEEE Transactions on Ultrasonics, Ferroelectrics, and Frequency Control*, vol. 65, pp. 2160–2166, Nov. 2018.

Titre: Conception d'ondes mécaniques localisées contrôlées : application à l'haptique

Mots clés: Contrôle de vibration, Piézoélectricité, Haptique , Métamatériaux

Résumé: Menés dans le cadre du projet pluridisciplinaire HASAMé, ces travaux visent à dépasser les limites des technologies haptiques de surface actuelles, notamment en matière de mise à l'échelle, d'efficacité énergétique et de précision spatiale des effets tactiles. L'objectif central est de générer une friction ultrasonore localisée, permettant aux utilisateurs de percevoir des retours tactiles — textures, boutons ou indications directionnelles — directement sur des interfaces tactiles. Pour ce faire, des approches de confinement passif et actif sont étudiées. Le confinement passif exploite les propriétés géométriques et matérielles de structures périodiques — telles que des piliers mécaniques — afin de créer des zones vibratoires localisées par atténuation d'ondes et conversion de modes. Ces structures sont conçues et analysées au moyen de modélisations analytiques fondées sur les théories des poutres et des plaques, ainsi que par des simulations par éléments finis ; des prototypes expérimentaux valident leur efficacité. À l'inverse, le confinement actif est réalisé au moyen de réseaux d'actionneurs et de capteurs piézoélectriques intégrés à la surface. Des stratégies de contrôle sont développées par superposition modale et mises en œuvre dans un repère tournant, ce qui permet de façonner le champ vibratoire en temps réel. Cette approche autorise non seulement le confinement, mais aussi la génération d'ondes progressives, essentielles pour induire des forces de cisaillement directionnelles perçues par le bout du doigt de l'utilisateur. Une contribution majeure de cette thèse réside dans l'introduction d'un cadre de modélisation fondé sur l'analogie électrique, s'appuyant sur le circuit équivalent de Mason, qui modélise chaque section de la surface vibrante comme une cellule électrique à trois ports. Cette méthodologie constitue un outil souple pour l'analyse et la conception de systèmes haptiques complexes à contrôle distribué. Les résultats expérimentaux, obtenus avec des cartes électroniques conçues sur mesure et une vibrométrie laser, confirment les prédictions théoriques en montrant un confinement précis des vibrations et un contrôle efficace des réponses tactiles. Dans l'ensemble, ces travaux proposent un cadre complet — couvrant modélisation, contrôle, réalisation expérimentale et évaluation centrée sur l'utilisateur — pour le développement d'interfaces haptiques de nouvelle génération, ouvrant la voie à des surfaces intelligentes et réactives applicables aux commandes automobiles, aux dispositifs médicaux et à l'électronique grand public interactive.

Title: Design of controlled localized mechanical waves: application to haptics

Keywords: Vibration control, Piezoelectricity, Haptics, Metamaterials

Abstract: Conducted within the framework of the multidisciplinary HASAMé project, the work aims to overcome the limitations of current surface haptic technologies, particularly regarding scalability, energy efficiency, and the spatial precision of tactile effects. The central objective is to generate localized ultrasonic friction, allowing users to perceive tactile feedback such as textures, buttons, or directional cues directly on touch interfaces. To achieve this, both passive and active confinement approaches are investigated. Passive confinement leverages the geometric and material properties of periodic structures—such as mechanical pillars—to create localized vibrational zones through wave attenuation and mode conversion. These structures are designed and analyzed using analytical modeling based on beam and plate theories, as well as finite element simulations, with experimental prototypes validating their effectiveness. On the other hand, active confinement is realized through networks of piezoelectric actuators and sensors integrated into the surface. Control strategies are developed using modal superposition and implemented in a rotating reference frame, enabling real-time shaping of the vibration field. This approach allows not only confinement but also the generation of traveling waves, which are crucial for inducing directional shear forces perceived by the user's fingertip. A significant contribution of this thesis is the introduction of an electrical-analogy-based modeling framework using Mason's equivalent circuit, which treats each section of the vibrating surface as a three-port electrical cell. The methodology provides a flexible tool for analyzing and designing complex haptic systems with distributed control. Experimental results obtained with custom-designed electronic boards and laser vibrometry confirm the theoretical predictions, showing precise confinement of vibration and efficient control of tactile responses. Overall, this work provides a comprehensive framework—spanning modeling, control, experimental implementation, and human-centered evaluation—for the development of next-generation haptic interfaces. It opens the way for intelligent, responsive surfaces applicable to automotive controls, medical devices, and interactive consumer electronics.

Université de Lille
L2EP / IRCICA
50 Avenue Halley, 59650 Villeneuve-d'Ascq, France